Dark Matter and Neutrinos in the Foggy Universe

by

Chiamaka Okoli

A thesis
presented to the University of Waterloo
in fulfillment of the
thesis requirement for the degree of
Doctor of Philosophy
in
Physics

Waterloo, Ontario, Canada, 2018

Examining Committee Membership

The following served on the Examining Committee for this thesis. The decision of the Examining Committee is by majority vote.

External Examiner: Lawrence Widrow
Professor, Dept. of Physics, Engineering Physics and Astronomy,
Queen's University

Supervisor(s): Niayesh Afshordi
Associate Professor, Dept. of Physics and Astronomy,
University of Waterloo
James Taylor
Associate Professor, Dept. of Physics and Astronomy,
University of Waterloo

Internal Member: Kendrick Smith
Adjunct Professor, Dept. of Physics and Astronomy,
University of Waterloo

Internal-External Member: Francis Poulin
Professor, Dept. of Applied Mathematics,
University of Waterloo

Other Member(s): Avery Broderick
Associate Professor, Dept. of Physics and Astronomy,
University of Waterloo

Author's Declaration

This thesis consists of material all of which I co-authored: see Statement of Contributions included in the thesis. This is a true copy of the thesis, including any required final revisions, as accepted by my examiners

I understand that my thesis may be made electronically available to the public.

Statement of Contributions

This thesis is based on the following published articles – all of which I co-authored –

Chapter 2 is based on **Okoli C**. and Afshordi N., *Ellipsoidal Collapse, Concentration and the Smallest Dark Matter Haloes*, 2016, MNRAS, 456, 3068

Chapter 3 is based on **Okoli C.**, Taylor J. E., and Afshordi N., *Searching for Dark Matter Annihilation from Individual Haloes: Uncertainties, Scatter and Signal-to-Noise Ratios* , 2018, JCAP, 08 019

Chapter 4 is based on **Okoli C.**, Scrimgeour M., Afshordi N., and Hudson M., *Dynamical Friction in the Primordial Neutrino Sea*, 2017, MNRAS, 468, 2164

My individual contributions to the above-named articles as as follows:

1. The ideas in the first article are Dr Afshordi's. In addition to coding the physics calculations to produce the figures, I set up the outline and wrote the first draft of the article edited by Dr Afshordi.
2. The ideas are Dr Taylor's. I then wrote the codes and made all related plots in this thesis.
3. Regarding the last article, I picked up the project from where Dr Scrimgeour left off, wrote the codes that made most of the plots, with the exception of figure A.2(a) in the appendix. I filled in most of the texts in the draft following the outline originally planned by Dr Scrimgeour. Dr Afshordi and Dr Hudson edited the final version.

ABSTRACT

Dark matter is predicted to be the main contribution to the matter content in the universe, in addition to ordinary baryonic matter such as protons and neutrons. However, we are limited in our knowledge of the nature of this main content of matter and some of its characteristics, hence the term "the Foggy Universe". The majority of the work included in this thesis is related to dark matter. It includes an investigation of the characteristics of dark matter haloes – structures expected to hold the galaxies/clusters – and a proposal to effectively search for dark matter particles through dark matter annihilation products such as gamma rays. In the last part of the thesis, we include a novel large-scale effect of cosmological neutrinos on haloes in the universe that is dependent on the neutrino mass.

In more detail, this thesis is a collection of the contributions we made to cosmological research regarding the nature of dark matter. Motivated by the non-existence of halo concentrations for small mass haloes due to the poor mass resolution of N-body simulations, we propose and verify the agreement of an analytical mass-concentration model using the ellipsoidal collapse theory and assuming the conservation of total energy. Thereafter, and guided by the success of this prediction, we use this model to make analytical calculations that may be relevant for the indirect detection of dark matter particles using gamma-rays as by-products of dark matter annihilation. We consider noise estimates to include the expected gamma rays due to the formation of stars in the galaxies hosted by these haloes and the presence of the isotropic gamma-ray background to predict a signal-to-noise ratio as a function of halo mass in a bid to pinpoint the most interesting halo masses that should be good targets for this detection.

Given that neutrinos are the second most abundant particle in the universe after the photons, we finish off by quantifying the effect of dynamical friction from primordial neutrinos that may slow down haloes and presented how this effect may be extracted from galaxy surveys using different galaxy species in redshift space. Although independent of the number density of galaxies in the survey, the confidence level of this proposed detection is dependent on the survey properties – such as the number of galaxies, mean redshift of the survey – and the neutrino properties such as the mass and hierarchy of the species and could be greater than 3σ using an optimal survey.

ACKNOWLEDGEMENTS

As much as I would like to appreciate all the people who made this thesis possible as much as they deserve, I cannot obviously appreciate and mention everyone who contributed to my success, but will attempt to. How can one successfully finish a PhD program without a great advisor? I feel greatly blessed to have two of them, Niayesh Afshordi – Although I never expected it, you have played the role of a coach, colleague, counsellor, critic, friend, mentor, motivator, and strategic teacher at different phases of this journey while being a supervisor, Physics enthusiast, and Family man. I appreciate you for being you and will not have enough words to describe my appreciation, especially while I healed from the traumatic event of my life. I always and still marvel at how you easily combine all the responsibilities of being a supervisor of many students, finding errors in a plot with a single glance at the plot, sending emails at 4 am, interacting at all the talks you attend, interacting with visiting scientists, teaching courses, being genuinely interested in broad research areas of Physics and being a parent to your young sons. Wherever life leads me tomorrow, You have undoubtedly left a very positive indelible mark in my life. James Taylor – I feel lucky to have been under your tutelage as a student. I have undeniably learnt a lot from you, especially how to make better scientific presentations. I appreciate your co-supervision greatly particularly the detailed feedback/comment you provide on any of my drafts. Special appreciation to my excellent collaborators on the project regarding neutrinos, Derek Inman, Mike Hudson, Ue -Li Pen, Morag Scrimegeour; my dear office mates, with whom I shared most of my time at PI, Natacha Altamirano, Cohl Dron, Yasaman Yazdi; Other wonderful colleagues – many whom have graduated – at Niayesh's weekly group meeting, who have seen/commented on the different versions of most of the figures in this thesis including, but not limited to, Farbod Kamiab, Mansour Karami, Matthew Robins, Mehdi Saravani, Nosiphiwo Zwane and Daniel Carrasco Guariento, who appreciates my plots and says they are so beautiful and look like bananas, you'll never know how much that comment made me make many more plots to be shown at the group meetings; fellow grad students who have made my stay at UW worthwhile – Anael Berrouet, Saoussen Mbarek, and Stephen Turnbull. May I use this opportunity to appreciate Raphael Sorkin, who chairs the group meetings in Niayesh's absence and never lacks in genuine curiosity when I give the group talk on any of my projects, which are not his usual specialty. Raphael – your questions during the talks end up making my projects seem more important knowing that you were following thereby increasing my personal motivation to get the job done. Also, the conversations we have shared about other spheres of life have shaped me and made me more responsible for our world.

I appreciate the members of my committee for their helpful feedback during this journey, special thanks to Avery Broderick and Francis Poulin for invaluable feedback on my thesis.

My profound gratitude goes to my external examiner, Lawrence Widrow, for his insight in connecting the projects in this thesis together. I appreciate greatly.

Siblings are best friends for life and my life would not have been the same without them – Chizoba Ojiako in Airdrie, Alberta, with whom I relax over the weekend by talking away our life struggles and challenges in a foreign land, Obinna Nwosu, Chibuike Nwosu, Olisa Nwosu, Chidubem Udorji, and Ubasom Nwosu. Parents are a child's biggest influencer and I feel fortunate to have one of the best set – Mum– Your life taught me how to stay strong in the midst of life challenges, I know you are beaming with smiles from above, Rest on! Dad – you always say that anything worth doing is worth doing well; your belief in me inspires me a lot. I am so proud to call you dad. In a culture that raises the girl-child to be only an ideal wife, thank you mum and dad for raising my sisters and I as the individuals we are, irrespective of our gender.

Teachers make all professions possible. I have had so many great teachers in life, beginning with my late mum and other primary school teachers, my secondary school teachers especially Mr Olusegun Ajayi, Mr Peter Ogah, and Mr Sunday Ochula, and my undergraduate professors at the University of Nigeria, Nsukka including Prof Alexandra Animalu, Prof Augustine Chukwude, Prof A B C Ekwealor, Prof Daniel Obiora, Prof C M I Okoye, Prof A A Ubachukwu, Prof Johnson Urama; and great mentors at ICTP, Trieste, Italy – Dr Shehu Abdussalam, Prof Paolo Creminelli, Prof K S Narain, Prof Seifallah Randjbar-Daemi, and Prof Ravi Sheth. I appreciate my undergraduate Research mentor and coach respectively – Dr Bonaventure Okere and Dr Daniel Okoh. I began learning Python from the seminar organized by Dr Godfrey Akpojotor; I am very grateful. May I use this opportunity to appreciate the company of my first friends in Waterloo, after the PSI program, – Solomon Akaraka, Ikenna Ezike, Joachim Nsofini, Emmanuel Ogbe, Marvellous Onuma-Kalu, Kesha Senessie, Cedric Sinamuli, – with whom I have shared lots of joyful, happy and memorable times in a bid to ease off graduate-life stress and have a home away from home. I am thankful to my good distant friends who keep motivating me with their numerous questions regarding my research/school work – Ozioma Adimonye, Linda Aneke, Ogechukwu Alum, Ifeoma Kama, Khardiata Ndiaye, Nnedinma Nwosu, Uchenna Nwosu, and Chanda Prescod-Weinstein.

As some may know, I survived a ruptured brain aneurysm in my supposedly last term of studies – Winter 2018. My deep gratitude goes to the paramedics and police officers that arrived my home and the doctor-on-call at Grand River Hospital Kitchener that early morning – Dr Zaid Jaber. Afterwards, I was firmly supported by a great medical team and life-saving neurologists and neurosurgeons – Dr Brian Anthony van-Adel, Dr Naif Alharbi, Dr Mohammed Alwadai, Dr Vishnu Sunjay Sharma, and the entire excellent team at the Hamilton Health Sciences; my Rehabilitation therapists and nurses at Grand River Hospital

(Rehabilitation centre) Freeport, who made sure I had fun during my numerous therapy sessions and helped me restore my independence, especially Laura Milne – Laura, please tell Becky that I am now consciously left-handed thanks to your rigorous Occupational therapy – Kiarash Akhavan, Holly Arnold, Norine Lum; and Karen, Karly, Kristen, and Soha; who continued home therapy sessions with me when I returned home. Now that I have recovered to a large extent, I have to admit that the response of the paramedics make me feel like I chose the wrong career path for the good of mankind. However, I know it's okay because the world needs a little bit of everything and we all play our unique roles in it.

People come into our lives as either blessings or lessons. During my five years sojourn in Waterloo, I have had the privilege of meeting many blessings – lots of amazing friends turned family, who have kept me going in life, took care of my little boy during my health challenge and visited the hospitals with fruits, flowers, and cards. While some called and sent messages to check up on me, others kept me company during my long recovery including Funso Akinniyi and family, Chioma Anierobi, Emeka Asogwa, Philomena Atekha, Julie and Bill Bishop, Michelle Brown, Nekoda Campbell, Debbie Delattre, Paul Dunk, Obinna Emeadi and family, Angela Ezugwu and family, Ghazal Geshnizjani, Kelly Krause and Family, Christiane Martins and family, Gabriel Magill, Chuka Moneme and family, Kenny Norris, Felix Nwashi and family, Ikechukwu and Uzoamaka Obodo, Patricia Ofili, Christian Ogbonna, Grace Ogor, Chioma and Uche Ojiako, Uzonna Okonkwo and family, Cosmas Onyenuforo, Fidelia Otokhina, Fr Phil Reily of St Louis parish, Waterloo, Paul Richards, Dr Paul Togunde and family, Amichai Tsarfati, James Ugwuogo and family and many other numerous friends and relatives.

This doctoral journey would not have started if not for the Perimeter Scholars International (PSI) programme. I would like to express my sincere appreciation to director, Neil Turok; Academic Program Coordinator, Debbie Guenther; Librarian, Dawn Bombay; PSI Fellow, Agata Branczyk; and many other past and present staff of the Perimeter Institute for theoretical Physics; Judy McDonnell, Heather Anderson and other staff of UWaterloo Department of Physics, Our dear Friends at St Louis Parish, Waterloo,and friends at Kw redeemers, Kitchener. Pierre -Andre Pashley, who sent me a great selection of my favourite Hillsong music to listen to during my recovery, Ourlaine Constant-Pashley, who got lots of fashionable hats for me to help with my self-esteem pending the replacement surgery of my right bone flap.

Writing this thesis would have been more tedious if not for the great strategies recommended by Nadine Fladd at the UW Writing and Communication Centre and her numerous Dissertation bootcamps that have helped my productivity. Even though you are so little to understand this, I appreciate you, my little boy, Munachi Okoli for motivating me to justify my absence when I leave you in the hands of another caregiver everyday. The smiles you bring to my life everyday are priceless. Sondra Dickin – you are amazing at providing care for my little munchkin; I am so confident he receives the best possible care, in my absence, at your place. I appreciate your sacrifice in making him comfortable. To my dear spouse, Felix Okoli, with whom I have weathered different storms and life challenges, I appreciate your support and sacrifice over the last nine years; in all honesty, your support made being a wife and mother seem so effortless.

As an international student, I appreciate the hospitality of Canadians and the support of the Federal and Ontarian governments towards my graduate-school funding and making me comfortable to call Canada home after five years. Finally, to the Author and Finisher of my faith, I am only a pencil in Your hands.

DEDICATION

This thesis is dedicated to my parents – Chief Sunday Nwosu and Late Mrs Louisa Ngozi Nwosu – and all the First responders in the duty of saving lives all over the world.

Table of Contents

List of Figures

Chapter 1

Introduction

About 85% of the matter content of the universe is dominated by Dark Matter – a name coined to mean matter that interacts with gravity but is non-interacting or weakly interacting via electromagnetic force to emit photons. Evidence for dark matter dates back to the measurement of the velocity dispersion of galaxies in a cluster– Coma cluster [184] and the rotation curve of galaxies – the Andromeda galaxy [143]. Recent evidence includes the measurement of the Cosmic Microwave Background in the sky by the *Planck* Collaboration [136], gravitational lensing of a galaxy due to a nearby cluster [167], and the Bullet Cluster [38] – the collision between two clusters that shows X-rays emitted from the regions concentrated with baryonic gas due to the heating of the gas being very different from the region that contains the majority of the mass seen in gravitational lensing.

1.1 Some Dark Matter Candidates

There are different proposals regarding the nature of dark matter including, but not limited to, weakly interacting massive particles (WIMPs), sterile neutrinos, axions, massive compact halo objects (MACHOs) such as brown dwarfs or black holes. MACHOs are expected to contribute a small percentage to, not entirely make up the total percentage of, dark matter [11]. Large scale structure observations are compatible with dark matter being massive and relatively cold, i.e. electrically neutral particles whose masses are higher than the keV scale and have very low thermal velocity, restricting this thesis to the investigation of Weakly interacting massive particles (WIMPs) in Chapter 3. Some more exotic options include dark matter as superfluids [11] and Bose-Einstein Condensates [44]. Detecting the WIMP using indirect detection techniques require good knowledge of the structure of dark mater on small scales. Our current knowledge of dark matter stems largely from N-body simulations. However, N-body simulations are currently limited in resolution to study small- scale structure today. Using alternative techniques, this thesis provides an analytic understanding of the internal structure of, and studies substructures present in, dark matter haloes while also predicting the large-scale effect of dark matter haloes in the presence of cosmological neutrinos. In the next few sections, we cover some basic results of simulated structure formation and dark matter halo properties such as the halo density profile and halo concentrations, and a few basic properties of cosmological neutrinos.

1.2 Cold Dark Matter Haloes

Most of the properties we know about dark matter haloes have been studied using numerical N-body simulations. N-body simulations numerically solve the equations of motion of N dark matter particles interacting through Newtonian gravity. These simulations begin from a high redshift, say $z = 100$ and follow through until today, $z = 0$. At the end of the simulation, snapshots of the particles are taken, from which dark matter haloes are then identified. Identification of haloes usually involve two known algorithms – spherical Overdensity (SO) [139], a method in which the centre of the halo is located as the minimum of the gravitational potential and the radial extent is the radius of the sphere at which the mean density of the halo is 200 times the critical density of the universe and friends-of-friends (FOF) [45], a method which also identifies the minimum of the gravitational potential and links particles that are closer than 0.2 times the mean inter-particle distance. An illustration of a density slice of the cosmic web is shown in Figure 1.1

Dark Matter haloes are theoretically believed to be the gravitational bedrock responsible for creating the deep potential required to begin the formation process of galaxies. Haloes are simply approximated as spherical objects and have been shown from early simulations [124] to follow the cuspy two-parameter radial profile given below:

$$\rho_{\rm NFW} = \frac{\rho_c \delta_c}{\left(\frac{r}{r_s}\right)\left(1+\frac{r}{r_s}\right)^2}, \tag{1.1}$$

where ρ_c is the critical density of the universe, r_s is a scale radius where the density profile is roughly isothermal and δ_c is an over-density parameter. This form of the density profile, initially proposed by Navarro, Frenk and White [124] (hereafter the NFW density profile, $\rho_{\rm NFW}$) is seen to be universal for different masses and variants of the universe such as flat, open, and closed universes. From the form of the profile, $\rho \propto 1/r$ in the innermost regions

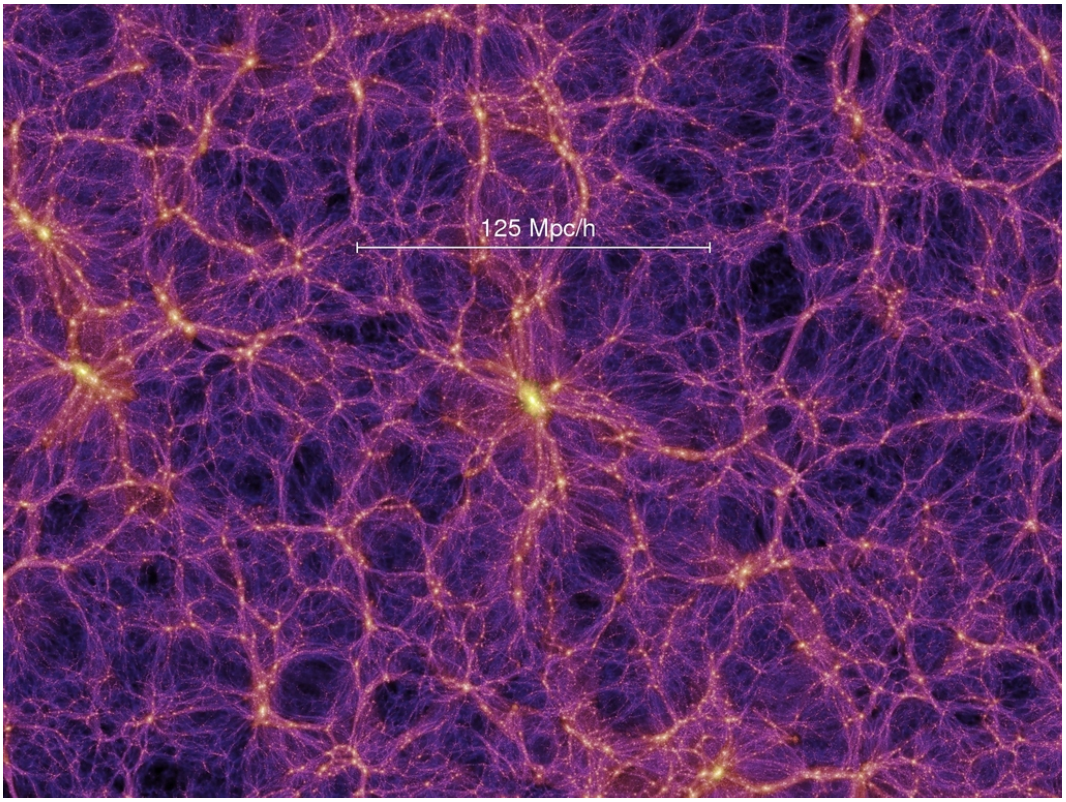

Figure 1.1: A slice of the density field of dark matter from an N-body simulation box from https://wwwmpa.mpa-garching.mpg.de/galform/virgo/millennium/

of the halo and $\propto 1/r^3$ in the outer regions of the halo. The above density profile may be rewritten in terms of the halo mass and halo concentration, with the concentration defined as $c_{200} \equiv \frac{r_{200}}{r_s}$. From N-body simulations, there exists a relation between the halo mass and halo concentration, matter density fluctuations using a single parameter. Results from simulations revealed that the halo concentrations in a ΛCDM universe increase with matter density fluctuations using a single parameter, an increase in the normalization of the power spectrum, σ_8. Physically, the redshift for collapse increases with the normalization of the power spectrum which then leads to higher concentration since the haloes are formed in the earlier epoch of the universe. In addition, the mass dependence of the halo concentrations for large mass haloes weaken as the spectral index becomes more negative.

1.3 Einasto Density Profile

Another profile that fits the density profile of simulated haloes is the three-parameter Einasto density profile, given by

$$\ln\left(\frac{\rho_{\mathrm{EINASTO}}}{\rho_{-2}}\right) = -2/\alpha\left[\left(\frac{r}{r_{-2}}\right)^{\alpha} - 1\right], \tag{1.2}$$

where similar to the ρ_s and r_s of the NFW profile, ρ_{-2} and r_{-2} are defined as the characteristic density and radius of the halo where the logarithmic slope of the density is -2. The third parameter α is the shape parameter that better determines the curvature of the inner part of the profile. A comparison of both profiles for a given mass and concentration is shown in Figure 1.2

1.4 Basic Neutrino Properties

In this section, we will introduce some basic properties of cosmological neutrinos. The introduction section of Chapter 4 will focus more on the role that neutrinos play in cosmology.

Neutrinos are the second most abundant particles of the Standard model after the Microwave photons that permeate the Cosmic Background. According to the Big Bang theory, neutrinos decoupled barely a second after the Big bang, prior to the decoupling of photons. Existing in three different flavours, the average temperature of each species is given by $T_{\nu,0} = \left(\frac{4}{11}\right)^{1/3} T_{\mathrm{CMB}}$, where $T_{\mathrm{CMB}} \approx 2.73K$ is the current average temperature of the cosmic microwave Background (CMB) photons. The current average number density is given as

$$n_{\nu,0} = \frac{6\pi\zeta(3)}{4}\left(\frac{kT_{\nu,0}}{hc}\right)^3, \tag{1.3}$$

where $\zeta(3)$ is the Riemann-Zeta function. The contribution to the total number density is given by

$$\Omega_{\nu,0} = \frac{\Sigma_i^3 m_i}{94.07h^2\mathrm{eV}} \tag{1.4}$$

At the very early times the neutrinos were relativistic but became non-relativitstic as the universe cooled down. The particular redshift at which each species became non-relativistic is given by $1+z_{\mathrm{nr}} = \frac{m_\nu}{5.28\times10^{-4}\mathrm{eV}}$ with an average thermal velocity that is given by $\langle v_{th}\rangle = 81(1+z)\left(\frac{\mathrm{eV}}{m_\nu}\right)\mathrm{kms}^{-1}$

1.4.1 Neutrino Mass Hierarchy

Neutrinos exist in three different flavours, the electron neutrino ν_e, muon neutrino ν_μ and tau neutrino, ν_τ The flavour eigenstates, ν_e, ν_μ, ν_τ are a coherent superposition of the mass eigenstates, ν_1, ν_2, and ν_3 through a unitary matrix, U such that

$$\begin{pmatrix}\nu_e\\ \nu_\mu\\ \nu_\tau\end{pmatrix} = \begin{pmatrix}U_{e1} & U_{e2} & U_{e3}\\ U_{\mu1} & U_{\mu2} & U_{\mu3}\\ U_{\tau1} & U_{\tau2} & U_{\tau3}\end{pmatrix}\begin{pmatrix}\nu_1\\ \nu_2\\ \nu_3\end{pmatrix} \tag{1.5}$$

The mixing matrix U is known as the Pontecorvo-Maki-Nakagawa-Sakata (PMNS) matrix. The mass hierarchy describes the assumed ordering of the masses of the different flavours and may be classified into the normal or inverted hierarchy, i.e whether the ν_3 mass eigenstate is heavier or lighter than the ν_1 and ν_2 mass eigenstates. Figure 1.3 illustrates this difference diagramatically.

1.5 Outline

The outline of this thesis is as follows: Chapter 2 focuses on our model of the theoretical derivation of the dark matter halo mass-concentration relation. This model, together with another model, is then applied to our predictions of the signal-to-noise ratio in the indirect search of dark matter from gamma-rays emitted through the assumed annihilation of dark matter particles in Chapter 3. Chapter 4 explores and quantifies a new effect of cosmological neutrinos on structures.

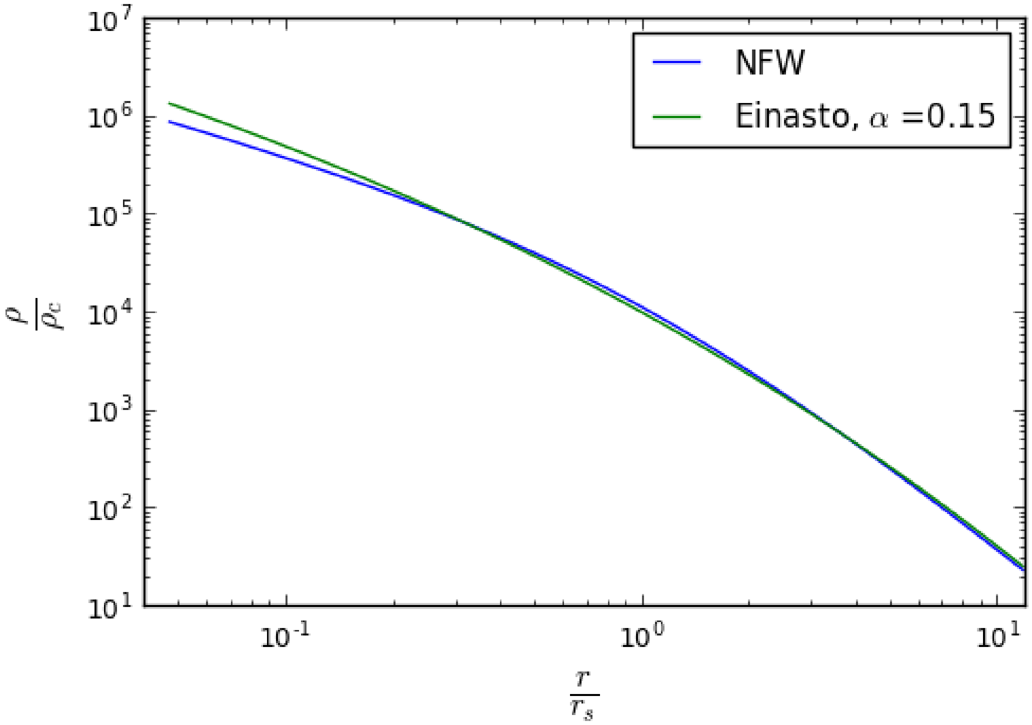

Figure 1.2: A comparison of the NFW and Einasto density profiles for a given mass and given halo concentration.

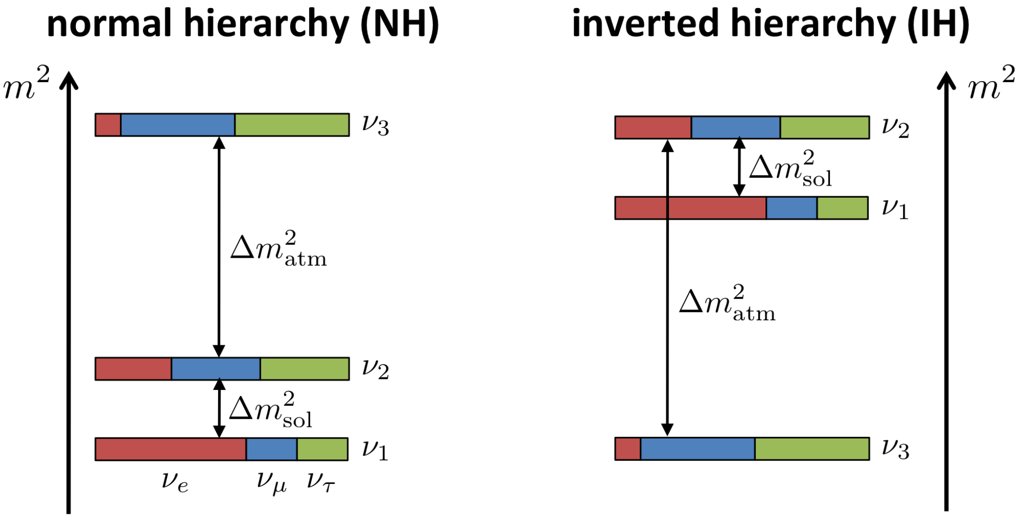

Figure 1.3: Illustration of the two different neutrino mass hierarchies – normal and inverted from http://www.staff.uni-mainz.de/wurmm/juno.html

Chapter 2

Dark Matter Halo Concentration

The concentration–mass relation gives deep insight into the formation and structure of haloes. More accurate concentration-mass relations can also be used to search for the elusive dark matter particles by placing limits on the dark matter annihilation flux from (sub)structures e.g [146]. Indeed, the latter is dominated by smallest haloes not resolved in N-body simulations by $z = 0$. This chapter summarizes a model of our concentration–mass relation for haloes, derived using physical principles of *energy conservation* and *ellipsoidal collapse*, which gives theoretical insight *and* clarity into the origin of such a relation. Our results are then compared with results obtained from simulations to validate our assumptions. Most significantly however, as our framework is rooted in physical principles, it can be applied and trusted well beyond the regime probed by simulations. In the next few sections, we present a short review of halo concentrations, define our random variables, their probability distribution and the initial total energy of a spherical region with random Gaussian initial conditions. The mean and dispersion of our random variables are then related to the concentration through the assumption of energy conservation. Section 2.2.2 incorporates the possibility of non-sphericity using the ellipsoidal collapse model of [150]. We discuss and conclude in Section 2.3.

2.1 A brief review of dark matter halo concentrations

Dark matter halo concentrations are mass dependent, with the high-mass haloes having the lower concentrations. Although the dependence of halo concentration on mass was initially thought to be a continually decreasing function of mass, [180] were the first authors to point out that the mass-concentration relation flattens at the high mass end at $z = 0$, (verified by a number of authors such as [127, 129]) with a minimum concentration of about 3.5. The exact mass at which the relation starts flattening is dependent on the redshift, it decreases to lower masses as the redshift increases. In order words, the mass-concentration relation becomes weaker at higher redshifts i.e the mass-concentration relation evolves faster at lower redshift ($z < 3$) than at higher redshift ($z > 3$) [127, 54, 123, 170, 129]. On the mass scales, low-mass haloes evolve more with redshift than high-mass haloes. This correlation between concentration and mass may be explained using the mass accretion rate [181]. According to [181], the concentration is constant at the high mass end because the massive haloes are in a fast accretion phase (where mostly major mergers occur) and the scale radius changes as the viral radius changes whereas the small mass haloes have higher concentrations because they are in the slow accretion phase (with mainly minor mergers) where the scale radius is more or less constant while the virial radius gradually builds up.

To predict the mass-concentration relation for any cosmology, redshift or any form of the power spectrum of matter fluctuations, concentrations may be related to a universal model of the mass accretion history (MAH) established through the mass accretion rate [181]. This model of concentration in terms of the MAH was the first attempt at making halo concentrations universal and also attempts to explain the redshift evolution of halo concentrations. The results from this model indicate that the haloes evolve in redshift not simply as $\frac{1}{1+z}$ as initially thought by [35], but in a more complex form. Therefore, a model for the halo concentrations may be built by relating the concentration to the time when the main progenitor had accreted 4% of its final mass (extracted from the MAH). According to [181], the time evolution of the concentration is given by

$$c = 4\left\{1 + \left(\frac{t}{3.75t_{0.04}}\right)^{8.4}\right\}^{1/8}, \tag{2.1}$$

where $t_{0.04}$ is the time when the main progenitor has accreted 4% of its final mass. In a similar vein, the distribution of halo concentrations may be extracted from the distribution of the formation times of the halo for a given mass. This approach was investigated by [69] by characterizing a relation between the distribution of halo formation times and the mass of the main progenitor using simulations. Defining the formation time as the earliest time when the main progenitor of the halo has a mass $m > fM_0$ for a mass M_0 today, a strong correlation was found between the halo concentrations and time provided the time when the halo had assembled about 4% and half of its total mass is known. Given a MAH, one can then cast the concentration-time relation into a concentration-mass relation.

Notwithstanding the fact that mass-concentration relations have been all expressed as power law fits in terms of mass up to this point, [138] introduced a fit, closer to being universal, of the mass-concentration relation by expressing the halo concentrations in terms of the root mean square (RMS) of the matter density fluctuations $\sigma(M, z)$. In addition, the concentrations were measured using a more profile independent method ($\frac{V_{max}}{V_{200}}$) rather than making a given fit to an assumed density profile (say NFW or Einasto). Over six orders of magnitude in mass and redshifts that range from $0 < z < 10$, the results of the concentrations show interesting features. The form of the halo concentrations as a function of mass show three distinct features - a region of decreasing halo concentration with mass (in the low-mass end), a region of flattening, and a region in which the halo concentrations increase with mass (the high-mass end), which was first observed in [95]. This upturn in the halo mass-concentration relation at the high-mass end is due to the massive haloes having particles falling into mostly radial orbits. To confirm that the upturn in halo concentrations isn't due to non-equilibrium effects, a sample of relaxed haloes displayed similar features. On a different note, [108] do not find the upturn at large masses when considering only relaxed haloes and the similar concentration measurements of [138]. They expressed concerns that the criteria by [138] for selecting the relaxed haloes was less stricter than theirs (those of [108]). The explanation for the supposed increase in concentration at the high mass end is that most of the systems are not yet virialized and that the accreted material are most likely experiencing their first pericentric passage. Intuitively, it is not clear that the concentrations increase at the high mass end since halo concentrations are related to the formation time of the haloes. and the high-mass systems have only being recently formed. A universal relation for concentrations was finally presented in [49] which is parametrized in terms of the peak height parameter and the local slope of the power spectrum n_{eff}. Expressing halo concentrations in terms of the slope of the power spectrum affects both the normalization and the slope of the concentration-mass relation.

So far, we have discussed concentration-mass relations measured from N-body simulations and then calibrated using a model. [129] presented a theoretical concentration-mass relation using arguments that include the conservation of energy and the ellipsoidal collapse model of [150]. This analytic concentration-mass relation will be the subject of the next sections in this chapter. This relation agrees very well with simulation results, in the realm where they exist and can be extrapolated to small mass regions, where we have no simulation data. The model also shows a flattening of the halo concentrations at large masses.

We will assume the Planck-15 cosmological parameters [136]: $\Omega_m = 0.3089$, $\Omega_b = 0.0486$, $h = 0.677$, $n_s = 0.967$, $\Omega_\Lambda = 0.6911$, $\sigma_8 = 0.8159$ when needed for our calculations.

In general, non-linear gravitational dynamics is difficult to deal with analytically; however, the assumption of the symmetry of the system simplifies the dynamics. For simplicity and since haloes are usually approximated as spherical systems, we consider a spherical overdensity field. We also ignore the tidal effects of neighbouring density perturbations upon the evolution of the isolated homogeneous spherical density perturbation. In what follows, we calculate the initial energy of this region (Section 2.1.1) and its virialization time (Section 2.1.2). These are then related to random variables whose probability distribution will play a key role in predicting the mean and dispersion of halo concentrations presented in Section 2.2.

2.1.1 Initial Energy

The total energy of an isolated system at a given time can be given as the sum of the kinetic energy and potential energy at that time. Thus, we derive the initial kinetic energy and potential energy of a spherical volume prior to collapse. For the kinetic energy of the region, we note that the velocity can be written as a function of gravitational potential ϕ_i [1] [131],

$$\mathbf{v} = H_i\mathbf{x} - \frac{2}{3H_i}\nabla\phi_i, \tag{2.2}$$

where H_i is the Hubble constant at the initial time. However, note that our results are independent of this choice of initial time, as long as it is in the linear regime. Writing the initial density of the region as a perturbation to the initial mean density of the universe

$$\rho(\mathbf{x}, t_i) = \rho_i[1 + \delta_i(\mathbf{x})],$$

the kinetic energy, to linear order in the perturbation, is then given by

$$K_i = \frac{1}{2}\rho_i \int (H_i^2|\mathbf{x}|^2 - \frac{4}{3}\mathbf{x}\cdot\nabla\phi_i + H_i^2|\mathbf{x}|^2\delta_i)d^3x. \tag{2.3}$$

The perturbation δ_i can be substituted in favour of the gravitational potential with the aid of the Poisson equation, then simplified further using the Friedmann equation to give

$$\begin{aligned} K_i &= \frac{1}{2}\rho_i \int (H_i^2|\mathbf{x}|^2 + \frac{2}{3}x^2\nabla^2\phi_i - \frac{4}{3}\mathbf{x}\cdot\nabla\phi_i)d^3x & (2.4)\\ &= \frac{1}{2}\rho_i \int (H_i^2|\mathbf{x}|^2 + \frac{4}{3}x^2\nabla^2\phi_i)d^3x - \frac{1}{3}\rho_i \oint x^2\nabla\phi_i\cdot d\mathbf{a}, & (2.5)\end{aligned}$$

where we have used the divergence theorem in simplifying Equation 2.5. Neglecting deviations from spherical symmetry at the boundary, we have

$$\nabla\phi_i = \frac{G\delta M}{R_i^2}\hat{r} = \hat{r}\frac{G\rho_i}{R_i^2}\int \delta_i d^3x.$$

---

[1] i here stands for the initial time

Finally, the kinetic energy is given as

$$K_i = \frac{4\pi G\rho_i^2}{3}\int_0^{R_i}\left[x^2 + \delta_i(2x^2 - R_i^2)\right]d^3x. \tag{2.6}$$

Clearly, the kinetic energy is the sum of that expected from spherical volume with mean density and that due to the perturbation. Similarly, the initial gravitational potential energy of the spherical region can be expressed as

$$U_i = -\frac{G\rho_i^2}{2}\int\int\frac{[1+\delta_i(\mathbf{x}_1)]\,[1+\delta_i(\mathbf{x}_2)]}{|\mathbf{x}_1 - \mathbf{x}_2|}d^3x_1d^3x_2 \tag{2.7}$$

To linear order in δ_i and using the symmetry under the interchange of x_1 and x_2, the potential energy is re-expressed as

$$\begin{aligned} U_i &= -\frac{G\rho_i^2}{2}\int[1+2\delta_i(\mathbf{x}_1)]d^3x_1\int\frac{d^3x_2}{|\mathbf{x}_1 - \mathbf{x}_2|} \\ &= -\frac{4\pi G}{3}\rho_i^2\int_0^{R_i}(1+2\delta_i)\left(\frac{3R_i - x^2}{4}\right)d^3x, \end{aligned} \tag{2.8}$$

where we arrived at the last part of Equation 2.8 by taking the second integral in a spherical volume. The initial energy, which is the sum of the initial kinetic energy and potential energy, is then given by

$$\begin{aligned} E_i &= -\frac{10}{3}\pi G\rho_i^2R_i^5\left[\int_0^{R_i}\delta_i(\mathbf{x})\frac{1}{R_i^3}\left(1 - \frac{x^2}{R_i^2}\right)d^3x\right] \\ &= -\frac{10}{3}\pi G\rho_i^2R_i^5B. \end{aligned} \tag{2.9}$$

The parameter B is thus defined as

$$B \equiv \int_0^{R_i}\delta_i(\mathbf{x})\frac{1}{R_i^3}\left(1 - \frac{x^2}{R_i^2}\right)d^3x. \tag{2.10}$$

It is important to note that the integral in the definition of B is a three dimensional integral whose domain is within a sphere of radius R_i, and we assume $\delta_i(\mathbf{x})$ is a random Gaussian field. Physically, B is the linear overdensity in the inner regions of a spherical region of initial radius R_i. For a given halo with initial radius R_i, the total initial energy of the halo fixes B.

2.1.2 Virialization Time

In the linear regime, density perturbations grow linearly with scale factor until they reach a critical value, after which they turn around from the uniform expansion of the universe and collapse to form virialized dark matter haloes. Various relaxation processes occur during the collapse of a spheroid from rest which prevents the object from collapsing to a point. However, one can safely assume that the collapsing object virializes at around half its radius at turnaround [72]. To examine this, consider a test particle with unit mass on the boundary of a spherical region of radius R_i, and initial mass, M, the total energy e of the particle is given as

$$e = \frac{\mathbf{v}_i^2}{2} - \frac{GM}{R_i}.$$

Assuming that the collapse time of the particle is approximately the same time necessary for the particle to be virialized, the collapse time t can be written as

$$t = \frac{2\pi GM}{(-2e)^{3/2}}. \tag{2.11}$$

With the mass, M interior to the test particle assumed to be virialized at t, we then relate the initial density to the collapse time through

$$-2e = \frac{5}{4\pi} H_i^2 R_i^2 \int_0^{R_i} \delta_i \frac{d^3x}{R_i^3}. \tag{2.12}$$

Using the Friedmann equation and that $M = (4/3)\pi R_i^3 \rho_i$, we define

$$A \equiv \int_0^{R_i} \delta_i \frac{d^3x}{R_i^3} = \frac{2}{5}\left(\frac{3\pi^4}{t^2 G\rho_i}\right)^{1/3} \tag{2.13}$$

Therefore, A relates the initial density perturbation of a spherical region to the virialization/formation time of a dark matter halo. Physically, in contrast to B, A is the mean linear overdensity of a region before collapse. Notice that Eq. (2.13) is equivalent to the standard spherical collapse threshold, when translated into linear overdensity today: $A \to \frac{4\pi}{3}\delta_{\rm sc} \simeq \frac{4\pi}{3} \times 1.686$ for Einstein-de Sitter cosmology [72].

2.1.3 Probability Distribution of the Parameters A and B

The parameters A and B are dependent on the linear density field which is a random Gaussian field. In this subsection, we study the resulting joint probability distribution of

A and B. Recall that we had defined

$$A \equiv \int_0^{R_i} \delta_i(\mathbf{x}) \frac{d^3x}{R_i^3},$$

and

$$B \equiv \int_0^{R_i} \delta_i(\mathbf{x}) \frac{1}{R_i^3} \left(1 - \frac{x^2}{R_i^2}\right) d^3x.$$

Assuming Gaussian statistics for the linear density field, the probability distribution function for A and B takes the form:

$$\begin{aligned} &P(A, B)dAdB = \\ &\frac{1}{2\pi\sqrt{L}} \exp\left[-\frac{1}{2L}\left(\left\langle B^2\right\rangle A^2 + \left\langle A^2\right\rangle B^2 + 2\left\langle AB\right\rangle AB\right)\right] dAdB, \end{aligned} \tag{2.14}$$

where $L = \langle A^2\rangle \langle B^2\rangle - \langle AB\rangle^2$. To determine this distribution, the values of the various spectra, $\langle B^2\rangle$, $\langle A^2\rangle$, and $\langle AB\rangle$ will have to be evaluated. To this end, we rewrite A as

$$A = \int \frac{d^3x}{R_i^3} \delta_i(\mathbf{x}) U(\mathbf{x}),$$

where $U(\mathbf{x}) \equiv \theta(R_i - |\mathbf{x}|)$, is a step function. Evaluating the average of the square of A in the Fourier space gives

$$\left\langle A^2\right\rangle = \frac{1}{2\pi^2} \int_0^{\infty} \frac{k^2 dk}{R_i^6} \left|\widetilde{U}(k)\right|^2 P(k), \tag{2.15}$$

where $\widetilde{U}(k)$ is the Fourier transform of $U(x)$ and the power spectrum, $P(k)$ is defined by

$$(2\pi)^3 \delta^3(\mathbf{k} + \mathbf{k}')P(k) = \left\langle \delta_{\mathbf{k}} \delta_{\mathbf{k}'}\right\rangle.$$

The power spectrum is the Fourier transform of the spatial correlation function, which is invariant under spatial translations and rotations. It is pertinent to note that this invariance is expected since the cosmological field is spatially homogeneous and isotropic. We should note that the standard definition of the variance of a spherical top-hat linear density perturbations is related to $\langle A^2\rangle$ by

$$\sigma^2(M) = \left(\frac{4\pi}{3}\right)^{-2} \left\langle A^2\right\rangle, \tag{2.16}$$

after extrapolating A using linear growth to today.

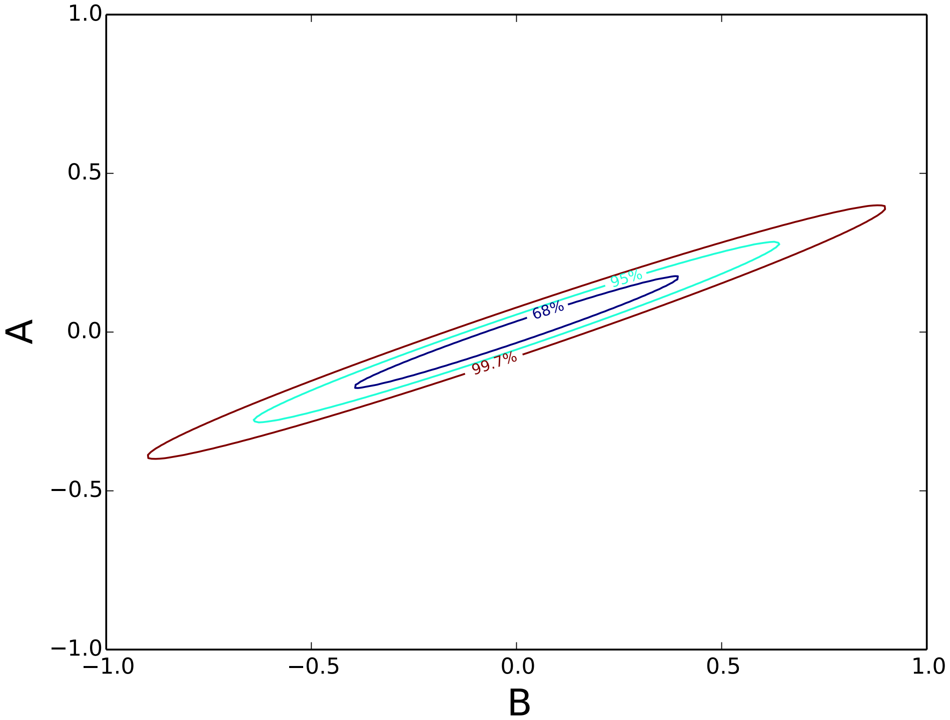

Figure 2.1: A typical joint probability distribution of the parameters A and B (extrapolated to today using linear growth) for a spherical region of comoving radius, $R = 8h^{-1}$ Mpc ($M_{200} \simeq 3 \times 10^{14} M_{\odot}$). The contours show the 0.68, 0.95, 0.99 confidence regions in the distribution.

2.1.4 Jeans Equation

The spherical Jeans equation relates the integrated mass, $M(r)$ of a spherically symmetric, dispersion-supported, collisionless system to its radial velocity dispersion, $\sigma(r)$ and mass density, $\rho(r)$, under the assumption of dynamical equilibrium. In a generalized coordinate system, the Jeans equation governing a system in dynamical equilibrium [31] is given as

$$\frac{\partial}{\partial t}\left(\rho\left\langle v_j\right\rangle\right)+\frac{\partial}{\partial x_i}\left(\rho\left\langle v_i v_j\right\rangle\right)+\frac{\partial \Phi}{\partial x_i}\rho\delta_{ij}=0. \tag{2.17}$$

Note that if the density, ρ, and the potential, Φ, are known, then this is a system of three equations with six unknown second order velocity moments. To close this system of equations, we assume that the mean velocity (streaming motion) of the particles in any direction, and the velocity covariance among different components are zero.

Evaluating Equation 2.17 in spherical coordinates, the spherical Jeans equation in the static limit is given by

$$\frac{\partial\left(\rho\left\langle v_r^2\right\rangle\right)}{\partial r}+\frac{2}{r}\rho\left\langle v_r^2\right\rangle-\frac{\rho}{r}\left\langle v_\theta^2\right\rangle-\frac{\rho}{r}\left\langle v_\phi^2\right\rangle=-\rho\frac{d\Phi}{dr}. \tag{2.18}$$

In terms of the dispersion, σ_i^2, the velocity anisotropy parameter is defined as,

$$\beta=1-\left(\frac{\sigma_t}{\sigma_r}\right)^2, \tag{2.19}$$

where $\sigma_t^2\equiv\frac{\sigma_\theta^2+\sigma_\phi^2}{2}$ and σ_r are the tangential and radial component of the velocity dispersion respectively. Thus, the familiar Jeans equation for a spherically symmetric system in equilibrium is given by,

$$\frac{d}{dr}\left(\rho\sigma_r^2\right)+\frac{2}{r}\rho\beta\sigma_r^2=-\rho\frac{d\Phi}{dr}. \tag{2.20}$$

The velocity anisotropy parameter β measures the deviation of the motion of a system of particles from isotropy. For purely circular orbits, $\sigma_r=0$, $\beta=-\infty$, whereas for purely radial orbits $\sigma_\theta=\sigma_\phi=0$, $\beta=1$. For isotropic motion, $\sigma_r=\sigma_\theta=\sigma_\phi$, $\beta=0$. The Jeans equation can be solved for the dependence of the radial velocity dispersion on radius for a fixed density profile and velocity anisotropy profile. While it is easy to solve Jeans equation for isotropic velocity dispersions, simulations show that haloes are not isothermal and thus have radially dependent velocity anisotropy profile. Various studies have revealed that this velocity anisotropy profile is a nonzero radially varying function, with a value close to 0 in the centre to approximately 0.4 in the outer regions of the halo [47, 75, 81, 177, 74, 82, 154].

[177] likened this relation to the ratio of the gravitational potential energy to the kinetic energy within the NFW scale radius for haloes with the NFW-like density profiles. For the purpose of our calculations, we assume that the anisotropic velocity dispersion parameter $\beta(r)$ is linearly related to the logarithmic slope of the density profile, $\frac{d\ln\rho(r)}{d\ln r}$ [75, 177] in an almost universal way by

$$\beta(r) = 1 - 1.15\left[1 + \frac{1}{6}\frac{d\ln\rho(r)}{d\ln r}\right]. \tag{2.21}$$

The solution to the Jeans equation is thus given by

$$\rho(r)\sigma_r^2(r) = \frac{\int_r^\infty dr' F(r')\rho(r')\frac{d\phi(r')}{dr'}}{F(r)}, \tag{2.22}$$

$$F(r) \equiv \exp\left(\int_0^r 2\frac{\beta(r')}{r'}\right), \tag{2.23}$$

where we have assumed $\rho(r)\sigma_r^2(r) \to 0$ as $r \to \infty$. Numerically calculating the velocity dispersion as a function of radial distance for a halo with an NFW profile, a concentration of 4, and an anisotropy profile given by Equation 2.21 yields the velocity dispersion profile shown in Fig. 2.2. The radial distance is in units of virial radius, r_{200}, while the radial velocity dispersion is normalized to its value at the virial radius. The velocity dispersion increases rapidly with radius at small radii (near the minimum of the potential), reaches a peak and then decreases outwards.

Although haloes are approximated to be in equilibrium at the virial radius, there is a continuous infall of matter onto the halo boundary and therefore a considerable amount of surface pressure at the boundary [166]. Integrating the Jeans equation (2.20) over a spherical region, the expected correction to the virial theorem due to infalling matter at the boundary is then given as

$$2K + U \simeq 4\pi r^3\rho\sigma_r^2\Big|_{r=r_{200}}. \tag{2.24}$$

The first term on the LHS is twice the total kinetic energy of the region, while the second term is the gravitational potential energy. The RHS in the Eq. (2.24) appears due to the non-vanishing external pressure at the boundary. For a vanishing pressure on the boundary, we have the familiar virial relation – the sum of the potential energy and twice the kinetic energy is zero. We can now solve the Jeans equation (2.20), using the anisotropy parameter $\beta(r)$ (2.21) and virial theorem (2.24), for any density profile $\rho(r)$ (e.g. NFW or Einasto) to find:

$$\omega \equiv -\frac{4\pi r^3\rho\sigma_r^2}{U}\Big|_{r=r_{200}}, \tag{2.25}$$

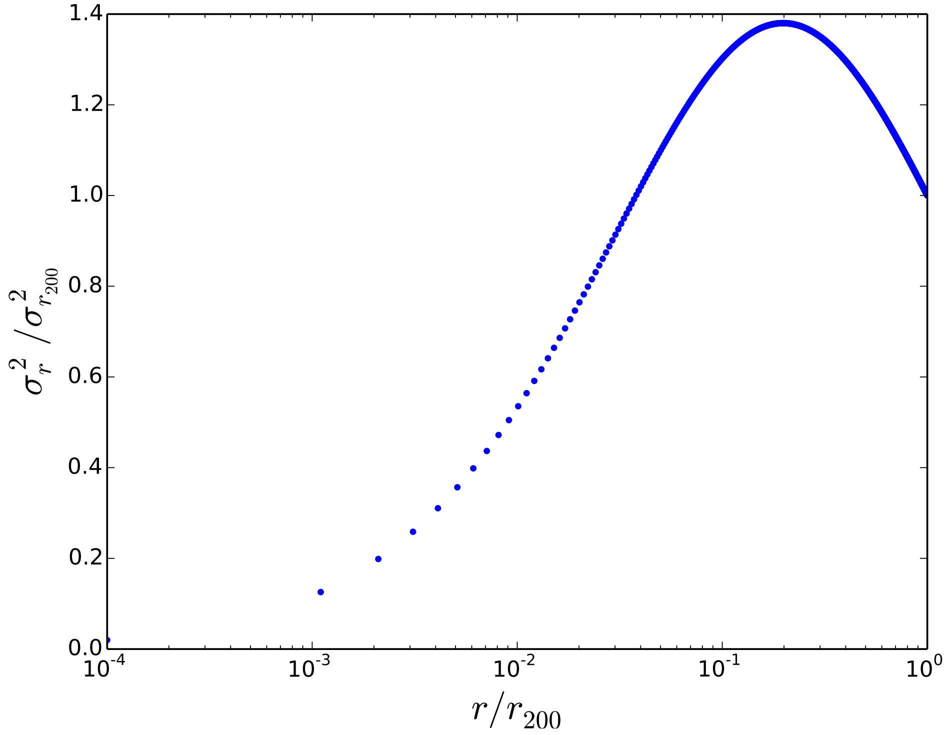

Figure 2.2: Radial dependence of the radial velocity dispersion, based on solving the Jeans equation with anisotropy parameter (2.21), for an NFW halo with $c = 4$. The radial distance is in units of virial radius, r_{200} while the radial velocity dispersion is normalized to its value at the virial radius.

2.2 Halo Concentration and Mass

In this section, we derive a relation between the concentration and mass of dark matter haloes by assuming that the total energy of a spherical region before collapse is equal to the total energy of the virialized halo formed from the collapse. This assumption is justified for spherical regions which are not coupled to the expansion of the background.

2.2.1 Spherical Collapse

The spherical collapse model [72] describes the formation of structure from the collapse of a spherical region perturbed in density. Let us first define a dimensionless measure of the total energy of the halo, E, as:

$$y \equiv -\frac{4E}{3M_{200}}\left(\frac{1}{2\pi G M_{200} H}\right)^{2/3}. \tag{2.26}$$

We can use the modified virial theorem (Equations 2.24-2.25) to find the final energy E_f of the virialized halo in terms of its density profile:

$$\begin{aligned} y_f &\equiv -\frac{4E_f}{3M_{200}}\left(\frac{1}{2\pi G M_{200} H}\right)^{2/3} = -\frac{1}{3}\left(\frac{200}{\pi^2}\right)^{1/3}\frac{r_{200}(1-\omega)U}{GM_{200}^2} \\ &= \frac{1}{3}\left(\frac{200}{\pi^2}\right)^{1/3}(1-\omega)\int_0^1 \frac{m(<x)}{x}dm, \end{aligned} \tag{2.27}$$

where x and $m(<x)$ are the radius and enclosed mass in units of r_{200} and M_{200}.

After solving the Jeans equation to find ω, as described in the last section, Equation 2.27 gives y_f in terms of concentration of the halo for any assumed halo profile. A fitting relation for $c(y_f)$ accurate to 10% for $0.5 < y_f < 20$ and $0.1 < \alpha < 0.52$ for the Einasto profile is given by:

$$\log c_{\text{Einasto}} \simeq a_1(\alpha)\ln {y_f}^2 + a_2(\alpha)\ln y_f + a_3(\alpha), \tag{2.28}$$

where

$$\begin{aligned} a_1(\alpha) &= -1.14\alpha^2 + 0.89\alpha - 0.17 \\ a_2(\alpha) &= 0.35 + 0.04\alpha^{-1.13} \\ a_3(\alpha) &= 0.50\alpha^{-0.43}. \end{aligned} \tag{2.29}$$

We have also already derived the initial energy, E_i, of the spherical region in Section 2.1.1. Combining Equations (2.9) and (2.13), we find:

$$y_i \equiv -\frac{4E_i}{3M_{200}}\left(\frac{1}{2\pi G M_{200} H}\right)^{2/3} = \frac{B}{A}\,(Ht)^{-2/3}\,, \tag{2.30}$$

which only depends on cosmology and the statistics of the linear initial density field (through A and B). A similar relation accurate to 10% also for $0.5 < y_f < 10$ using the NFW profile is

$$\log c_{\rm NFW} \simeq 0.78 \ln y_f + 1.09. \tag{2.31}$$

Fixing the virialization time, t, fixes A (or the spherical collapse threshold) through Equation (2.13), which in turn fixes the probability distribution of B through Equation (2.14):

$$\left\langle \frac{B}{A} \right\rangle = \frac{\langle B \rangle}{A} = \frac{\langle AB \rangle}{\langle A^2 \rangle} \approx 0.42, \tag{2.32}$$

with a Gaussian dispersion from the mean given as,

$$\frac{\Delta B}{A} = A^{-1}\sqrt{\frac{L}{\langle A^2 \rangle}} \approx 0.083\nu^{-0.6} \qquad (0.1 \leq \nu \leq 10) \tag{2.33}$$

where $L = \langle A^2 \rangle \langle B^2 \rangle - \langle AB \rangle^2$, and $\nu \equiv \delta_{\rm sc}/\sigma(M)$ is the standard measure of peak height with $\delta_{\rm sc} \approx 1.68$. Fig 2.3 shows the behaviour of $\left\langle \frac{B}{A} \right\rangle$ and its dispersion as a function of radius (mass). Note that, while Equations (2.32-2.33) provide accurate fits for ΛCDM linear power spectrum, they can be used for arbitrary power spectra and cosmologies using their definitions in Sec. (2.1.3)

We are therefore completely armed with all the necessary tools to derive the concentration–mass relation, simply by assuming:

$$y_i = y_f \tag{2.34}$$

in Equations (2.28-2.33). Fig. 2.4 shows our derived relation for the spherical collapse model using the NFW profile. This shows a nearly constant relation, irrespective of mass, and a scatter that decreases with mass. For the Einasto density profile, the expected concentration is 10% higher than that of the NFW profile. These results clearly do not agree with the well-known results from N-body simulations – the concentration–mass relation decreases with mass [124, 35, 127, 108, 138, 106]. However, as we will show in Section 2.3, they agree reasonably well at large masses. One reason for this is that the spherical

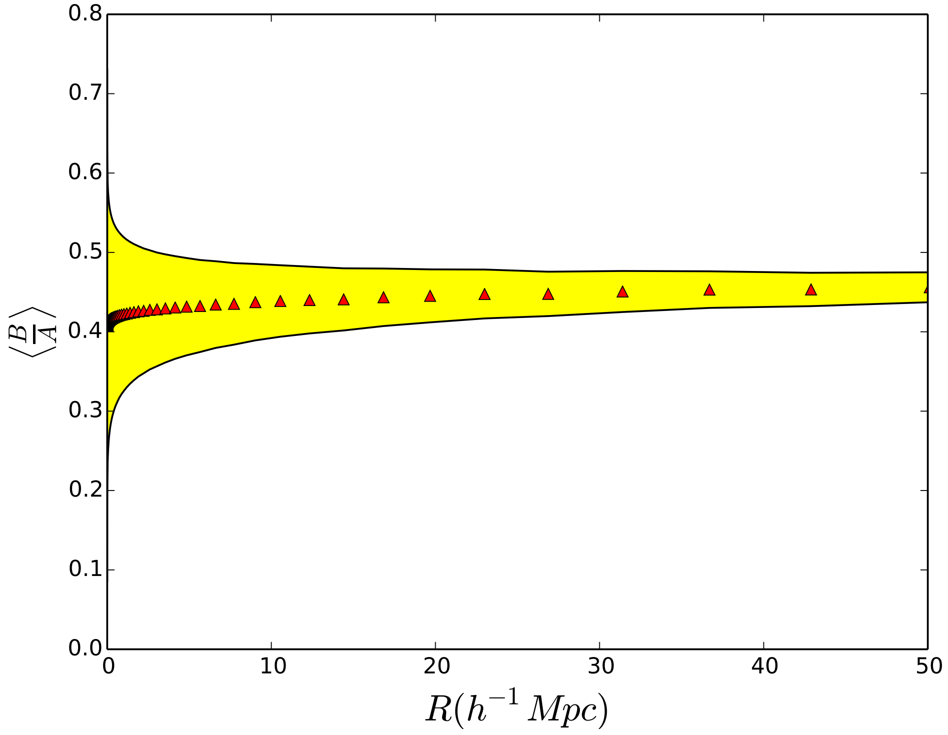

Figure 2.3: The average value of $\left\langle \frac{B}{A} \right\rangle$ and its dispersion, ΔB for various radii (masses).

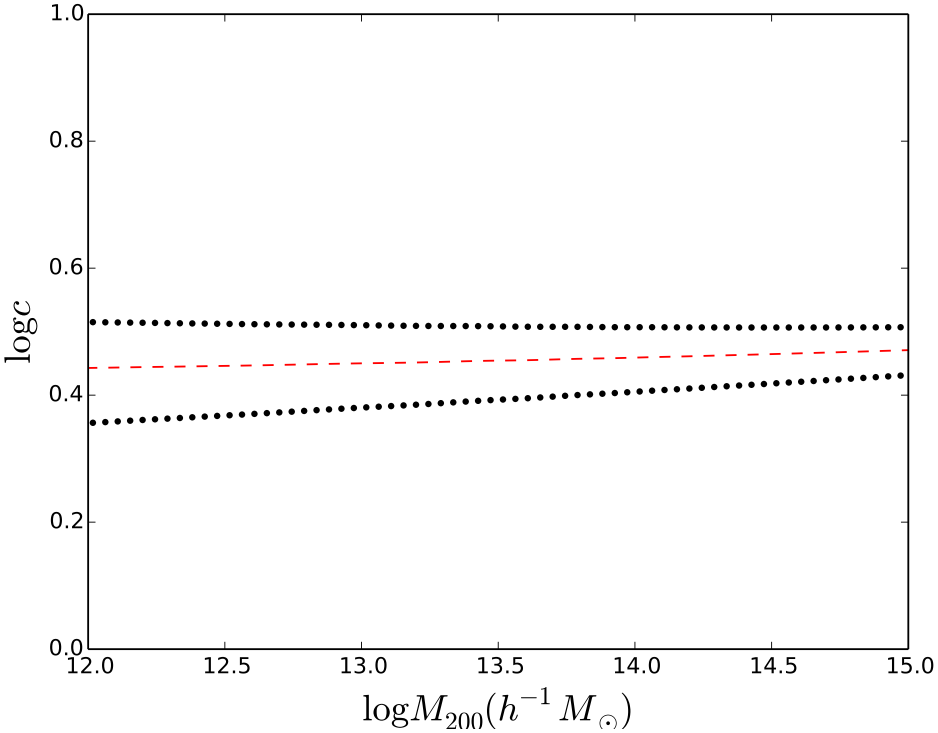

Figure 2.4: The mass–concentration relation of dark matter haloes with an NFW density profile derived from the spherical collapse model for the ΛCDM cosmology at $z = 0$. The red dashed line gives the average value while the region between the thick black dots gives the dispersion in concentration for a fixed halo mass.

collapse model is well suited for collapse of high mass haloes but fails at low masses [150]. The spherical collapse model also evolves weakly with redshift (our relation changes little with redshift through the Ht variable y_i), thus agrees with the results of [65] and [106] that concentration of high mass haloes evolves weakly with redshift. In the next subsection, we incorporate the corrections due to the ellipticity of the low mass haloes to the mass–concentration relation.

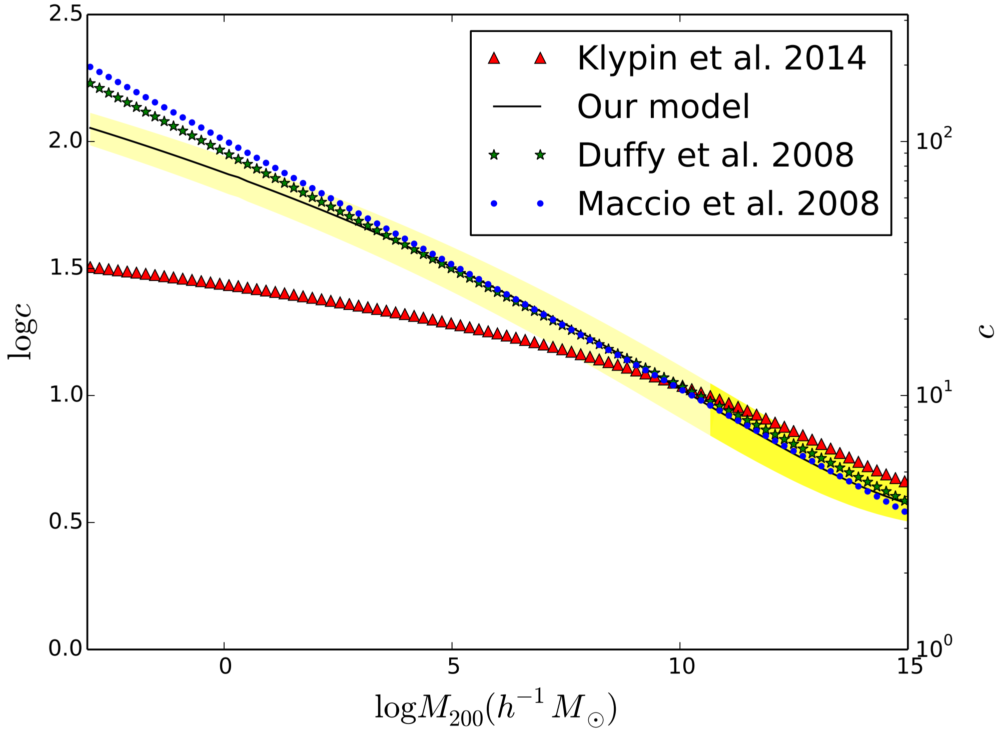

Figure 2.5: The concentration of dark matter haloes as a function of mass for haloes with NFW density profile and ΛCDM universe (WMAP5 Cosmology) at $z = 0$. The black line shows the results of the mean concentrations derived from our model with the yellow region as the dispersion for fixed masses. Also shown are the concentrations from recent literature [54, 109, 94]. The region in darker yellow show the range of masses probed by most N-body simulations, while lower masses use extrapolations by different groups. The decrease in concentration with mass can be interpreted as a result of the decrease in the critical collapse density as the mass increases. Previous results [124, 65, 86] reveal that the halo concentration is a measure of the density of the universe at formation since smaller masses form earlier.

2.2.2 Ellipsoidal Collapse Model

The spherical collapse model in its simplicity oversimplifies the formation of bound objects from collapse. Our modifications to the spherical collapse model stems from the assertion that perturbations in Gaussian density fields are triaxial [51]. Although the spherical collapse model makes reasonably simple analytic predictions regarding the shape of the mass function of bound objects, when compared to simulations, it has more low mass haloes and less high mass haloes [150]. The considerable reduction of this discrepancy with haloes remodelled with the ellipsoidal collapse model motivates the consideration of a similar remodelled collapse in the concentration–mass relation. The spherical collapse model described in Section 2.2 assumes that collapse occurs if the mean initial density of a region exceeds a critical value, δ_{sc}. This critical value is independent of mass or radius (only dependent on redshift, z) of the region and is thus known as the constant barrier. This implies that at a fixed redshift, all haloes with average initial overdensity greater than δ_{sc} will collapse. However, [150] modified this relation for assumptions of ellipsoidal collapse, also known as the moving barrier. This modification is based on the fact that the critical overdensity for ellipsoidal collapse, δ_{ec} depends on the mass or size of the collapsing region. An interesting consequence of this mass dependence is that smaller objects, which are more likely to be influenced by external tides, should have larger initial overdensities to hold them together as they collapse. This effect leads to a higher collapse time which verifies the results of [48]. Although a fixed mass fixes the collapse time (equation 2.13) for the spherical collapse model, due to the range of ellipticities and prolatenesses in an ellipsoidal collapse, there is a range of collapse times for any fixed region (mass).

$$\begin{aligned}\rho(\mathbf{r},t) &= \frac{\rho_b(t)}{\det\left(\partial x_j/\partial q_i\right)} \\ &= \frac{\rho_b(t)}{\det\left[\delta_{ij} + D(t)(\partial p_j/\partial q_i)\right]}. \end{aligned} \tag{2.35}$$

The tensor $\frac{\partial x_i}{\partial q_j}$ is known as the deformation tensor. This matrix can be diagonalized at every point, $\mathbf{q}$ to yield a set of eigenvalues as a function of $\mathbf{q}$. The eigenvalues, $\lambda_1 \geq \lambda_2 \geq \lambda_3$, define a coordinate system in which a certain volume preserves its original orientation upon deformation. Alternatively, one can also describe the shape of a region by its ellipticity, e, and prolateness, p, [150] defined by

$$e = \frac{\lambda_1 - \lambda_3}{2\delta} \text{ and } p = \frac{\lambda_1 + \lambda_3 - 2\lambda_2}{2\delta} \tag{2.36}$$

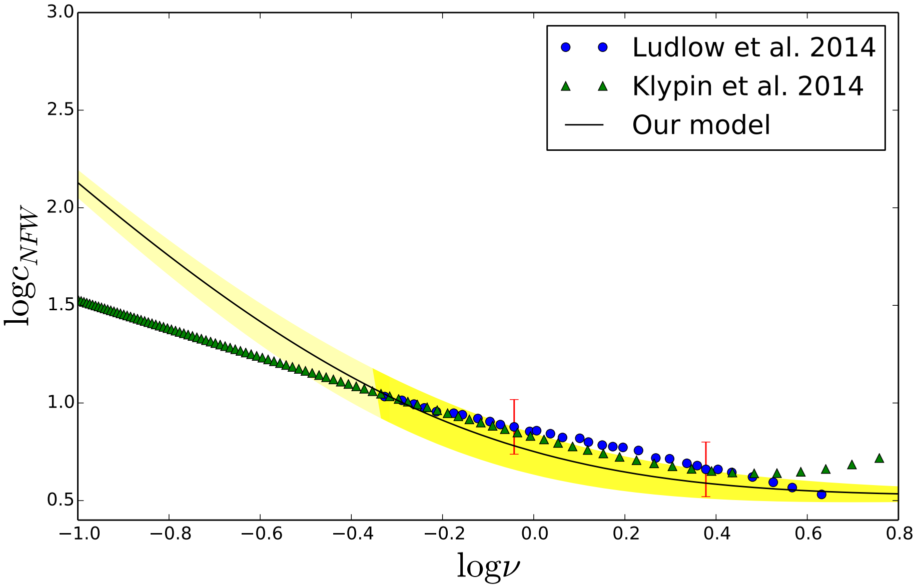

Figure 2.6: The concentration of dark matter haloes as a function of $\nu = \delta_c/\sigma(M, z)$ for haloes with NFW density profile for the ΛCDM universe (Planck Cosmology) at $z = 0$. The parametrization in terms of ν is preferable since it incorporates both the mass dependence and redshift dependence of the concentration. As in Figure 2.5, the black line shows the results of the concentrations derived from our model, while the regions in darker colour show the mass range probed by N-body simulations. Also shown are the concentrations from recent literature [106, 94]. The red error bars show the dispersion of the results for [106].

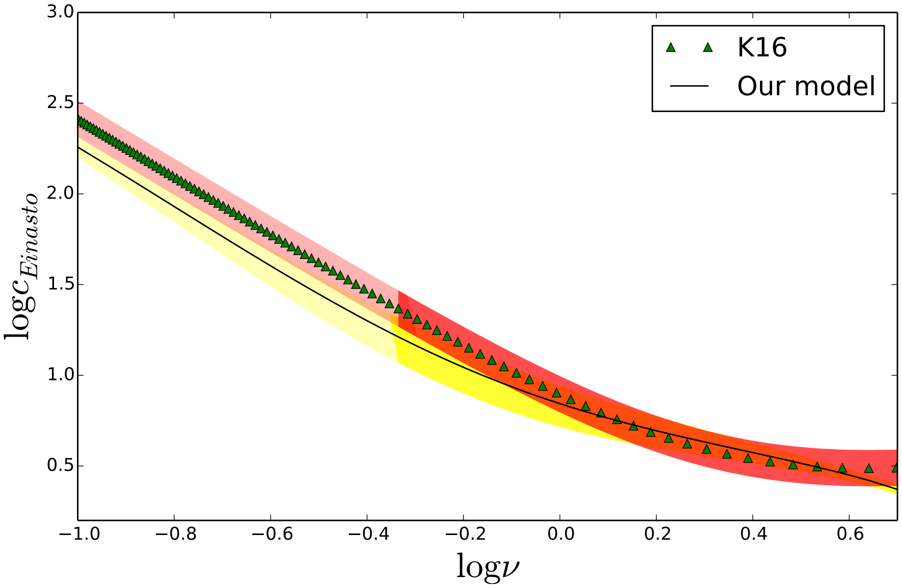

Figure 2.7: The concentration of dark matter haloes as a function of $\nu = \delta_c/\sigma(M,z)$ for haloes with Einasto density profile for the ΛCDM universe (Planck Cosmology) at $z = 0$. As in 2.5, the black line (yellow region) shows the results (dispersions) of the concentrations derived from our model. Also shown are the concentrations from [94] with its 10% dispersion at fixed mass. The difference in color shades have the same meaning as in Figure 2.5

The eigenvalues are ordered such that $e \geq 0$ if $\delta > 0$, and $-e \leq p \leq e$. A spherical region has $e = 0$ and $p = 0$. Following [150], the evolution of an ellipsoidal perturbation is specified by the eigenvalues of the deformation tensor or alternatively by the density contrast δ and the initial ellipticity, e and prolateness, p of the linear tidal field. One can then construct the initial overdensity for collapse $\delta_{\rm ec}(e, p)$, for any e and p. An average collapse overdensity $\delta_{\rm ec}(\sigma)$, can be estimated on a scale R parametrized by σ by averaging over the distribution of e, p, and δ. For $p = 0$, the relation between $\delta_{\rm ec}$ and mass is fitted by

$$\delta_{\rm ec}(\nu) \approx \delta_{\rm sc}\left(1 + \kappa\nu^{-2\gamma}\right), \quad \text{with } \kappa = 0.47 \text{ and } \gamma = 0.615, \tag{2.37}$$

where $\nu \equiv \delta_{\rm sc}/\sigma(M)$ is the standard definition of the peak height parameter.

All these steps can be combined into three lines to give concentration at 10% precision, for arbitrary redshift, cosmology, and halo mass (as long as the power spectrum does not deviate too widely from ΛCDM):

$$\boxed{\begin{aligned} y &= \frac{0.42 + 0.20\nu^{-1.23} \pm 0.083\nu^{-0.6}}{(Ht)^{2/3}}, \\ \log c_{\rm Einasto} &= a_1(\alpha)\log {y_f}^2 + a_2(\alpha)\log y_f + a_3(\alpha), \\ \log c_{\rm NFW} &= 0.78\ln y + 1.09. \\ & \end{aligned}} \qquad \begin{array}{r}(2.38)\\(2.39)\\(2.40)\\(2.41)\end{array}$$

2.3 Discussion and Conclusion

Qualitatively, the concentration of dark matter haloes is a decreasing function of mass that flattens at very low and very high masses. This feature – decrease of concentration with mass – can be attributed to major mergers that lead to bigger haloes, but disrupt the inner regions of haloes that subsequently decreases concentration. We have used the conservation of energy to derive the concentration–mass relation of CDM haloes. The robustness of our prescription lies in the fact that one can compute the concentration–mass relation for any cosmology by using the cosmology-dependent power spectrum, cosmic age, and linear ellipsoidal collapse threshold, $\delta_{\rm ec}$. Our results show that the concentration of a halo is set by the initial total energy of the region prior to collapse, as well as the cosmological parameters at collapse time. Small mass haloes mostly collapse from ellipsoidal regions and are better described by the ellipsoidal collapse model while large mass haloes are well described by spherical collapse model.

Several analytical relations exist in the literature for the concentration–mass of CDM haloes, though fitted through numerical simulations. [106]'s model generates the concentration of CDM haloes from simulated and analytic mass accretion histories of haloes. Their model predicts that at very low masses, the concentration varies slower than one should expect from power law fits at high masses. This feature, according to the authors, is a consequence of the shallow slope of the linear power spectrum at very low masses/small scales. However, at high masses, it approaches a constant value. This characteristic corroborates the expectations from our model and is consistent with earlier results of [180]. [145] also predict a theoretical mass-concentration relation through their theoretical density profile which relates to the accretion rate of haloes. The free parameter of their model is then fit to the mass-concentration relation of [180]. The concentration-mass relation agrees with ours within the simulated range, flattening around $10^{15}M_{\odot}$ with a surprising upturn beyond $2 \times 10^{15}M_{\odot}$. Although the concentrations derived from our model may be different when compared to those from the millennium simulations at some masses, it is marginally consistent within the range of dispersion as shown in Fig. 2.6. Our predicted halo concentrations also have dispersions around the median at fixed masses [35, 97]. A novel feature of our prediction is the decrease in the dispersion of the concentration with mass. This agrees with the results of [127], which suggests it may be the result of massive haloes collapsing recently and are thus more homogeneous. On average for different mass bins, [127] had dispersions in their concentrations of about $\sigma_{log_{10}c} = 0.1$ for relaxed haloes, which is marginally consistent with our dispersions at fixed a masses for medium-sized haloes. At $z = 0$, our predictions are consistent with the concentrations of [13] and [86] for very small microhaloes. Our method does not suffer from the lack of scalability [138], it is therefore applicable to any set of cosmological parameters. Though our results have been exclusively reported for $z = 0$, it is applicable to different redshifts through the redshift dependence of ν – the usual scaling of the variance $\sigma(m)$ by the cosmological growth function, $D(z)$ and slightly through the Ht parameter in the definition of y, Equation 2.38.

Chapter 3

Prospects for the Indirect Detection of Dark Matter from Gamma rays

The ΛCDM (Λ cold dark matter) cosmological model predicts that over 25% of the total energy density in the universe is contained in cold dark matter – particles with generally small random velocities [136]. The gravitational effect of dark matter was originally inferred from unexpected high velocity dispersion of galaxies in the Coma cluster [184]. This evidence was further supported by the flattening of the rotation curves, with increasing distance from the galactic centre, of spiral galaxies [143] and through gravitational lensing – the bending of light path when it passes by a massive object The mass reconstruction of a galaxy-cluster collision indicates that the ratio of non-luminous matter to luminous matter is very high [38]. Given these pieces of evidence, techniques to detect the dark matter particle abound. Candidates for dark matter include the sterile neutrinos – hypothetical particles proposed to explain the mass of the Standard Model (SM) neutrinos observed via neutrino oscillations and the see-saw mechanism; weakly interacting massive particles (WIMPs) – hypothetical stable, neutral, massive particles with weak interaction cross-sections and could account for the current dark matter density e.g. the neutralino (the lightest neutral particle in an extension of the Standard Model, Supersymmetry); and axions – a massive particle that appears in a symmetry that solves the strong CP problem in Particle Physics (See [151] for more details). Dark matter particles may be detected through their direct scattering with atomic nuclei [116], through their production from Standard Model particles in particle colliders or through the products of their annihilation such as neutrinos, gamma rays, matter and anti-matter [92]. Signal from products of annihilation such as gamma rays may be detected via the Fermi gamma-ray space telescope, major atmospheric gamma imaging Cherenkov (MAGIC) telescope, high energy stereoscopic system (HESS) or very energetic radiation imaging telescope array system (VERITAS) at the centres of galaxies including the Milky Way. The Large Hadron Collider (LHC), on the other hand, searches for dark matter particles that may be produced from the collision of protons at high energies of 7 TeV [90]. Direct detection experiments on the other hand search for nuclear recoils that may appear through the scattering of a dark matter particle and a target nuclei. These experiments include DAMA, CDMS, CRESST-II, XENON, LUX, etc; see [116] for a more comprehensive review of direct detection experiments. This chapter sharpens our search for dark matter through indirect detection using individual haloes as targets.

In order to clearly detect the signal from products of dark matter annihilation, a good understanding of the distribution of haloes in the Universe, substructure in haloes, and the radial distribution of particles in a halo is required. These include the density profile of haloes, the concentration-mass relation of dark matter haloes, and the modelling of subhaloes in individual haloes. In addition, the assumed mass of the particle and the cross-section for interaction both play various unique roles in the predictions. Current knowledge of these halo properties stem largely from numerical N-body simulations and are occasionally supplemented by semi-analytic models of structure formation. Although there is uniformity in these estimated properties within the regions explored by the simulations, extrapolating these relations to low masses (where resolution effects prevent the direct exploration of these regions in numerical simulations) lead to quite a disparity in the estimates of various authors. In addition to studying the uncertainty from dark halo concentration and substructure models, this chapter explores and predicts the signal- to noise ratio from gamma rays as a function of mass. The dark matter annihilation signal from the galactic and extragalactic region have been explored in [14, 4, 2, 10] and the effects of substructure considered in [159, 96, 134, 92]. This work differs from similar works in this area through the inclusion of the noise sources of gamma rays from individual haloes – due to activities such as star formation leading to a predicted signal-to-noise ratio as a function of halo mass. The outline of this chapter is given as follows: we introduce and estimate the boost from individual haloes due to structure and the different halo properties in Section 3.1, we study the effects of including the subhaloes in haloes in Section 3.2, we make estimates for the expected signal-to-noise ratio as a function of halo mass in Section 3.4

3.1 Boost estimates from the individual halo properties

3.1.1 Boost over a halo

Given a neutrally-charged dark matter particle χ and its antiparticle $\bar{\chi}$, its rate of annihilating into another particle and antiparticle is given by

$$R = \frac{\langle \sigma v \rangle}{m_\chi^2} \int \rho^2 dV, \tag{3.1}$$

where m_χ is the mass of the particle and $\langle \sigma v \rangle$ is the velocity-averaged cross section of the particles. The density profile of the halo of DM particles in a region of volume V is given by ρ. For a smooth halo of constant density $\bar{\rho}$, the integral in Equation (3.1) is simply given as $\bar{\rho} M_h$. For haloes with radially varying profiles, Equation (3.1) depends on the details of the halo density profile. In general, Equation (3.1) is rescaled by a boost factor for real haloes. The dimensionless boost factor B_h may be defined as

$$B_h \equiv \frac{\int \rho_h^2 dV}{\bar{\rho}^2 V.} \tag{3.2}$$

Evaluating B_h depends on the density profile and the truncation radius of the halo (for the rest of these work the halo will be truncated at the virial radius – R_{200}).

Figure 3.1 shows the dependence of B_h on the concentration of haloes for the NFW profile and the Einasto profile (for four different constant shape parameters α). The boost from the haloes starts to steepen for haloes with concentrations $c \geq 3$. Although the NFW profile is a universal profile for different masses, the value of the shape parameter in the Einasto profile isn't universal. It increases as the mass of the halo increases [65, 56, 94]. In terms of the linearly extrapolated overdensity δ_c and the density variance $\sigma(M, z)$, the variation of the shape parameter in mass is parametrized with the peak height parameter $\nu \equiv \frac{\delta_c}{\sigma(M,z)}$:

$$\begin{aligned} \alpha(\nu) &= 0.155 + (0.0095\nu^2) \\ \alpha(\nu) &= 0.115 + (0.014\nu^2) \end{aligned} \tag{3.3}$$

for [65] and [94] respectively. In the following subsection, the effect of the concentration of haloes on the boost factor is discussed.

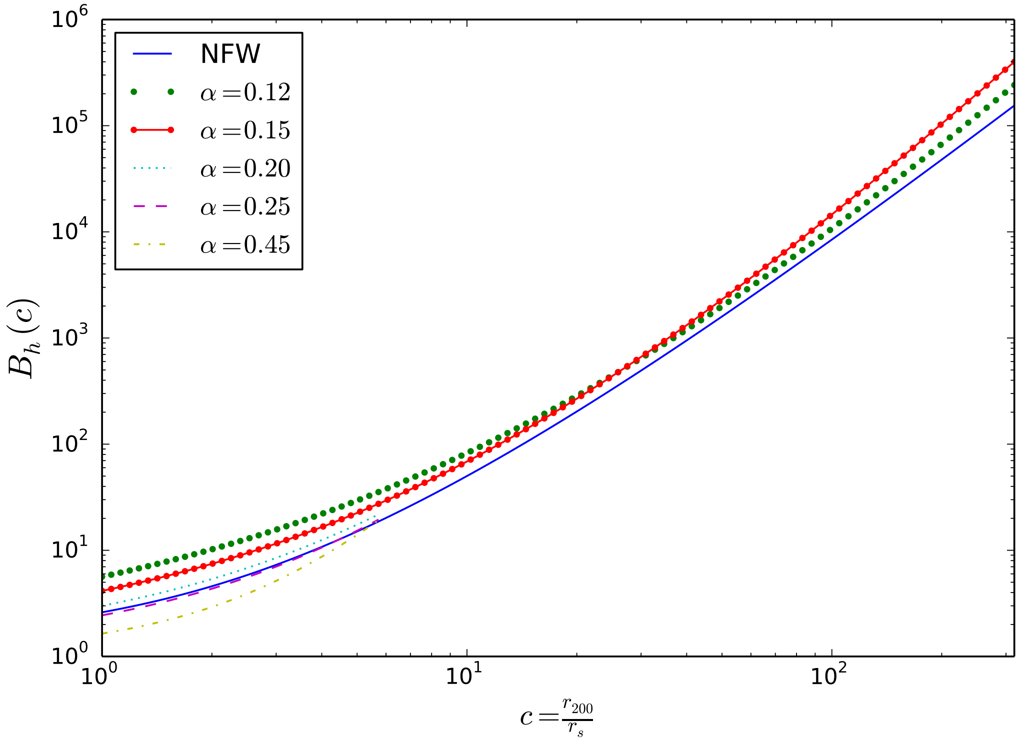

Figure 3.1: The range of boost predictions as a function of concentration for the NFW and Einasto profile (with four different shape parameters).

3.1.2 Effects of the concentration-mass relations

Following the study of the halo profile and initial modelling of halo concentrations by [124], a number of concentration-mass relations/models have been proposed over the years. Our aim in this section is to quantify the range of realistic concentrations allowed by a number of concentration-mass relations in the literature. The concentration reflects the density of the universe at the formation epoch of the haloes [35, 124] – high mass haloes have smaller concentration because they recently formed and the small mass haloes have a higher concentration because they formed at a time when the universe was denser. Halo concentrations are also related to the different regime of a haloes history, with the rapid accretion regime having a constant concentration and the slow accretion regime with a higher concentration [181] and in general the mass accretion history of a halo [170, 106]. So far, all the above prescriptions agree that the concentration is a decreasing function of mass or plateaus at high masses at low redshifts.

Contrary to the above expectations for high masses, some concentration-mass relations predict an increase with mass for high masses and at high redshifts especially for masses higher than the typical collapse mass for that redshift [95, 138, 56, 49]. Although this reported upturn has been controversial, a recent paper [94] aimed at investigating this disagreement found that the concentration-mass relation has, in fact, three trends – a regime of decreasing concentration with mass, one of roughly constant concentration with mass and a trend in which high mass haloes have higher concentrations. Higher-than-expected concentrations for the high ν end are attributed to the fact that the high ν haloes are not well fit by the NFW density profile but by the Einasto profiles. As expected from [65], at z=0, the high ν haloes have higher values of the alpha parameter and the concentrations of haloes of a given mass are higher for haloes with higher alpha. Thus, contrary to the speculations that the higher concentrations measured for high peak haloes at high redshifts are due to non-equilibrium effects [108] or the prescription for calculating the concentration (using the peak circular velocity or the fits to the density profile) [see [56]], [94] concur that these relations are real and that their very large suite of simulations had good mass resolution to probe this effect.

The concentration-mass relations have been traditionally based on the fits to the halo mass. However as pointed out by [109], these fits in terms of mass are only good for the cosmology for which it was fitted and may not be used for a given set of different cosmological parameters such as Ω_m, h, σ_8. In addition, extrapolations of these relations to lower masses lead to very high concentrations ($c \sim 1000$ at the present day) that have been ruled out by high redshift simulations such as [13, 86]. These simulations start up with initial conditions at $z \sim 400$ and run till $z = 32$. The masses of the microhaloes are

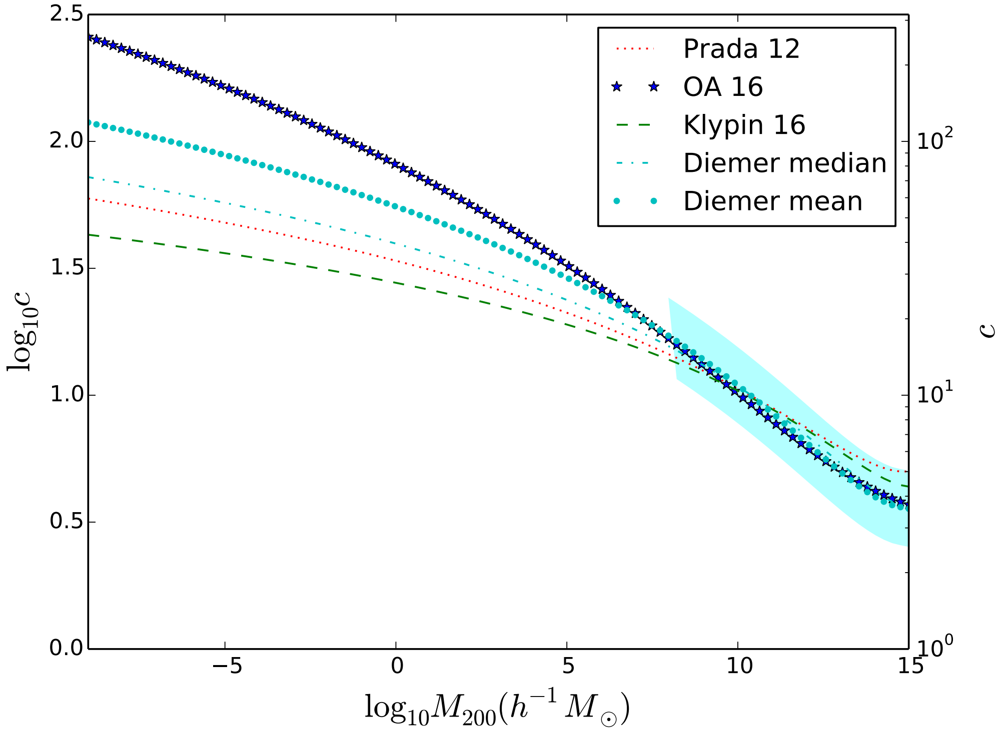

Figure 3.2: The range of concentration for haloes at $z = 0$ for four different models of concentration-mass relations. The mass range of the cyan region shows the regions that have mostly been sampled by N-body simulations. The vertical range of the cyan region depicts the mean dispersion in the simulated halo concentration.

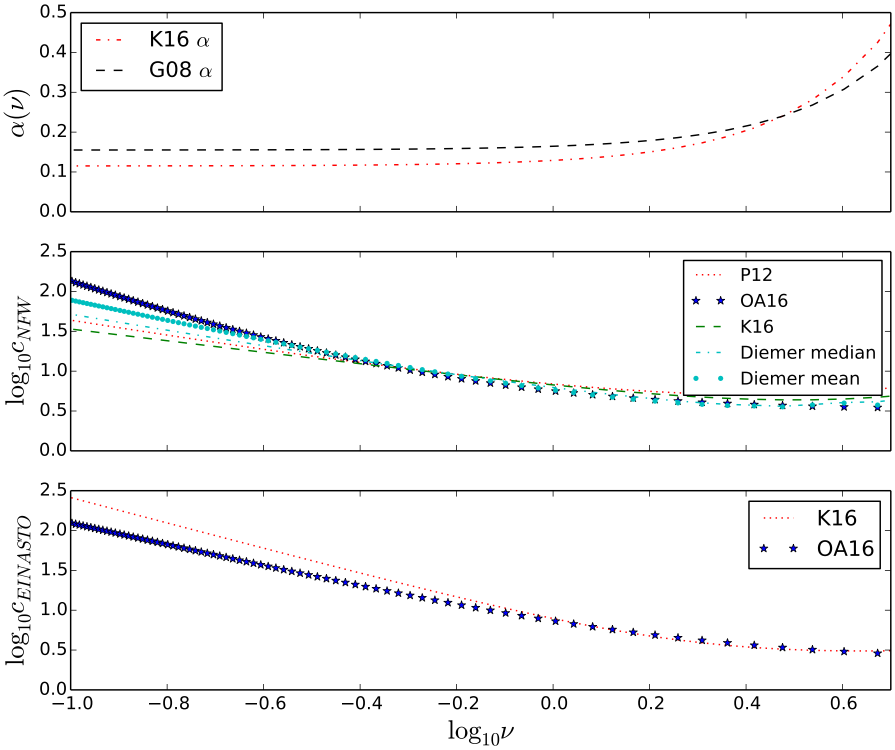

Figure 3.3: The top plot shows the two variants of the $\alpha(\nu)$ relation from [65] and [94] while the bottom plots shows the $c-\nu$ relation from [129] (OA16) and [94] (K16) for the NFW profile and Einasto profile.

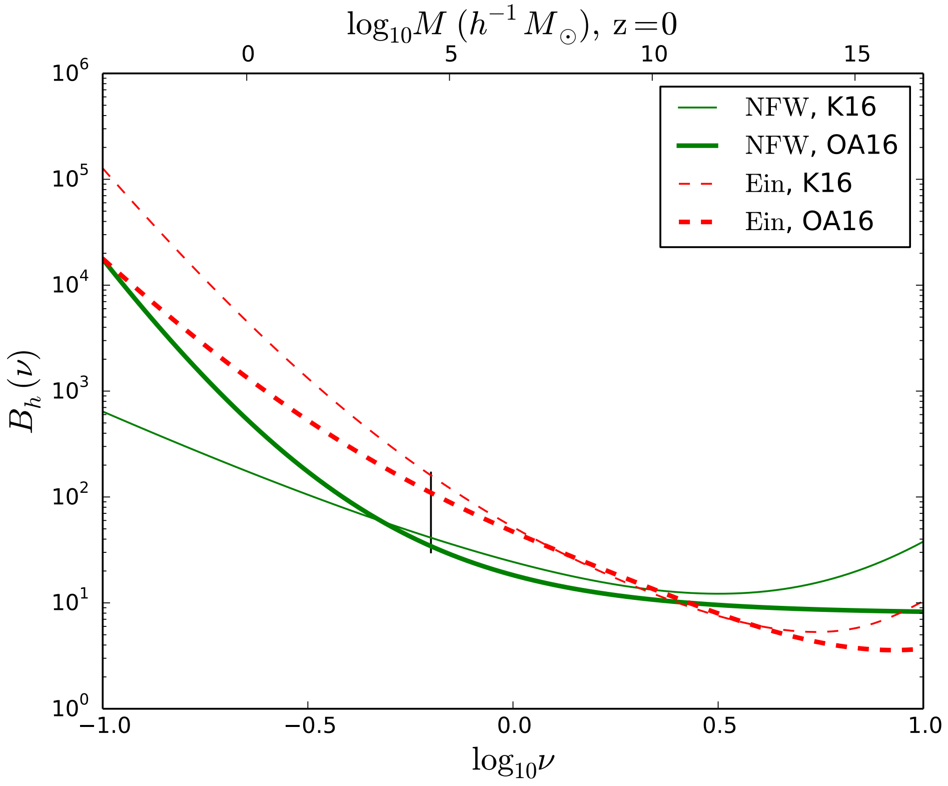

Figure 3.4: The range of a single halo boost as a function of ν given different choices of the density profile, α shape parameter and halo concentrations at $z = 0$. The thick red (black) curves are the concentration-nu relation from [94] ([129]) for a given profile. The thick lines are for the NFW profile while the thin-dashed (thick-dashed) lines are for the Einasto profile with the $\alpha(\nu)$ relation of [65] and the c-ν relation of [94] ([129]).

Earth-sized, which are closer to the cutoff scale of the dark matter particles. Although the density profiles of these microhaloes were different from those of NFW, the measured concentrations were rescaled to those expected from an NFW profile at the present day to give median concentrations of $60-70$ for the [86] simulation and $94-124$ for the [13] results. [35], [181] and [138] are some of the models that express the concentration in terms of $\sigma(m)$, the variance of density fluctuations. The parametrization in terms of σ or the peak height parameter ν scales out the dependence on cosmology and partly the redshift (see [49] for more details). In the concentration-mass space, the concentration then flattens out at very small masses [146]. Given the shortcomings of the parameterization in terms of mass discussed earlier, we will focus on concentration relations parametrized in terms of the mass variance $\sigma(m)$ or the peak height parameter $\nu \equiv \delta_c/\sigma(m)$. Figure 3.2 bears out the current range of the concentrations for different halo masses at $z=0$. The high mass end has been sampled a lot more and thus the relations agree to within 20%. The low mass end has a wide range of median concentrations which subsequently leads to a range of uncertainties in the boost prediction ($\sim$ an order of magnitude). For predicting the uncertainty in concentration in the rest of this work, we will adopt the lowest and the highest low-mass concentration estimates i.e [94] and [129] respectively which are given by:

$$c_{\mathrm{NFW}} = 0.522\left[1+7.37\left(\frac{\sigma}{0.95}\right)^{3/4}\right]\left[1+0.14\left(\frac{\sigma}{0.95}\right)^{-2}\right] \tag{3.4}$$

and

$$c_{\mathrm{NFW}} = \left[3.2+\left(\frac{0.696}{\nu}\right)^{2.32}+\left(\frac{1.71}{\nu}\right)^{1.31}\right] \tag{3.5}$$

respectively. Similar equations may be written for the concentration of haloes with the Einasto profile in the same order as follows:

$$c_{\mathrm{EINASTO}} = 6.5\nu^{-1.6}\left(1+0.21\nu^2\right) \tag{3.6}$$

$$c_{\mathrm{EINASTO}} = 2.28+\left(\frac{3.25}{\nu}\right)^{1.38} \tag{3.7}$$

The above relations are usually the mean/median concentration-mass relation for a range of masses. It is paramount to note that the for a given mass, distribution of concentrations is a log-normal with a scatter $\sigma_{\log_{10} c}$ of about 0.18 [88, 35]. [127] also investigated the distribution of concentrations and concluded that the distribution for the relaxed (unrelaxed) haloes agrees well with a lognormal distribution with some mean and scatter (smaller mean and larger dispersion). The dispersion also has a weak mass dependence in which the large mass haloes have lower values. The values include 0.106 for haloes of $\sim 10^{12}h^{-1}M_\odot$ to 0.06 for large mass haloes of about $\sim 10^{15}h^{-1}M_\odot$. This may be attributed to the rarity of the large mass haloes and the fact that abundant smaller haloes have a wide range of assembly redshifts. The cyan region in Figure 3.2 shows a mean mass independent range of halo-to-halo scatter given the average concentrations.

For a single halo, the uncertainties in the halo profile, the various choice of the α relation (discussed in the previous section) and overall uncertainty of the concentration-nu(mass) relation may be combined to give an expected boost as a function of the peak height parameter ν. These combined effects are depicted in Figure 3.4. For the rest of this chapter, the NFW profile will be used as the baseline, while allowing for about 2 orders of magnitude on estimates for the Einasto profile, the various shape parameters and different halo concentrations.

3.1.3 Scatter in the halo concentrations

In making the boost estimates in the previous section, we have used the mean of the halo concentrations. However, the concentrations are log normally distributed for a given mass. In the following, we will consider the effect of this scatter on halo concentrations on the expected boost for a given halo. Consider the distribution of concentrations at a fixed mass given as

$$P(\log(c)) = \frac{1}{\sqrt{2\pi}\sigma} \exp\left\{-\frac{(\log c - \log \bar{c})^2}{2\sigma^2}\right\} d\log c \tag{3.8}$$

Also, $P(c)$ my be expressed as

$$P(c) = \frac{1}{\sqrt{2\pi}\sigma c} \exp\left\{-\frac{(\log c - \log \bar{c})^2}{2\sigma^2}\right\} dc \tag{3.9}$$

Since B_h is a monotonically increasing function of c, say $h(c)$ as seen in Fig 3.1, one can find the inverse function that gives c as a function of B_h, $h^{-1}(B_h)$. The distribution of the boost can be derived from the distribution of the concentrations, given a relation between the boost and the concentrations, as

$$P(B_h) = P(c(B_h)) \left| \frac{dh^{-1}(B_h)}{dB_h} \right| \tag{3.10}$$

Relative to other uncertainties, we found that the effect of the scatter in halo concentrations after all calculations, at a fixed mass, in the estimate of the boost is negligible for the range of halo masses we are interested in and will therefore be ignored henceforth.

3.2 Effects of substructure

3.2.1 P^2SAD prescription

In this section, we investigate the effects of substructure using the particle phase space average density (P^2SAD) of [178]. This model is based on the stable clustering hypothesis in phase space which may be simply written – that for very small separations in phase-space coordinates Δx and Δv, the average number of particles within a particle does not change with time. This hypothesis, together with a tidal stripping model, successfully described the survival fraction and spatial distribution of subhaloes in a halo. Thus, the contribution of substructure (which includes all subsequent layers of substructure if there are any) to the boost factor may be estimated for various mass and redshift. Towards this end, the relevant equation for the boost due to existing substructure is given by

$$B_{sub} = \frac{8\pi^{1/2} b^3 200 \rho_{c,0} f_{sub} M_{200}}{9\delta_c^3} \int_{m_{\min}}^{m_{\max}} \mu(m_{col}) m_{col}^{-2} d[m_{col}^2 \sigma^3(m_{col})], \tag{3.11}$$

where $B_{sub} \equiv \int \rho^2 dV$ is the contribution to dark matter annihilation due to substructure, $\mu(m_{col})$ is the mean fraction of particles that are bound for a given mass that collapsed earlier into a larger structurem_{col}, δ_c is the spherical collapse density, $b = 3.53$, $m_{\min}$ and $m_{\max}$ are the minimum and maximum masses in substructure for a given halo mass and $\sigma(m)$ is the cosmological variance in density perturbations for a given mass. Thus to relate this boost factor to our previous definitions of the boost, (i.e relative to the mean density), we define the boost including substructure as B_{hs} and is given as

$$\begin{aligned} B_{hs} &= \frac{R_{sm} + R_{sub}}{\bar{\rho}^2 V} \\ &= B_h \left(1 + \frac{R_{sub}}{R_{sm}}\right) \end{aligned} \tag{3.12}$$

The P^2SAD prescription thus includes the effect of the substructure to the expected boost from the presence of structure B_h. Figure 3.6 illustrates the effect of substructure on the boost using the P^2SAD prescription.

3.2.2 Analytic substructure model

In this section, we consider the effect of substructure within a given halo using some proven analytic prescriptions. Consider a main halo of mean density $\bar{\rho}$ and volume V, with the smooth component of mean density ρ_1 contained in a volume V_1 and the subhalo of mean density ρ_2 contained in volume V_2, then the estimated total boost from these two subvolumes is given by

$$\begin{aligned} f(V = V_1 + V_2) &= \left[\left(\frac{\bar{\rho}_1}{\bar{\rho}}\right)^2 \left(\frac{V_1}{V}\right) f(V_1) + \left(\frac{\bar{\rho}_2}{\bar{\rho}}\right)^2 \left(\frac{V_2}{V}\right) f(V_2)\right] \qquad (3.13) \\ &= \left[\left(\frac{\bar{\rho}_1}{\bar{\rho}}\right) \left(\frac{M_1}{M}\right) f(V_1) + \left(\frac{\bar{\rho}_2}{\bar{\rho}}\right) \left(\frac{M_2}{M}\right) f(V_2)\right], \qquad (3.14) \end{aligned}$$

where M_1 and M_2 are the smooth and subhalo mass contribution to the total mass M respectively and $f(V_1)$ and $f(V_2)$ are the boost estimates from the smooth component and the subhalo component respectively. To first approximation, the mean density of the smooth component is approximately same as the mean density of the halo. Thus, $\bar{\rho} \approx \bar{\rho}_1$. Assuming the mass fraction in subhaloes is X, then the fraction in the smooth component is $(I - X)$. The total boost may then be written as

$$f(V) = (1 - X) f(V_1) + \left(\frac{\bar{\rho}_2}{\bar{\rho}}\right) X f(V_2) \,. \qquad (3.15)$$

Till this point, we have only assumed a single subcomponent to the main halo. In reality, however, we expect a halo to have multiple subhaloes. Generalizing equation 3.15 to include multiple components gives

$$f_h = (1 - X) f_{\mathrm{sm}} + \sum_{i \,\in\, \mathrm{subhaloes}} \left(\frac{\bar{\rho}_i}{\bar{\rho}_h}\right) X_i f_i \,. \qquad (3.16)$$

While the properties of the smooth haloes are estimated within the virial radius r_{vir}, the properties of the subhaloes – such as M_i, $\bar{\rho}_i$, f_i are estimated within the tidal radius, r_t. The tidal radius is the radius where the tidal force from the host halo becomes equal or greater then the self gravity of the subhalo. As a subhalo orbits a host halo, mass is lost due to tidal stripping until it gets to the tidal radius. Thus to estimate the boost contribution from subhaloes, we need to find the mass fraction contributed by subhalo i, (X_i), the average density of a subhalo, i within its tidal radius relative to the main halo's average density $\frac{\bar{\rho}_i}{\bar{\rho}_h}$, and the boost of the subhalo within its tidal radius, f_i. We will enumerate on how to determine these parameters below.

1. Subhalo boost of each subhalo within its tidal radius

To estimate the subhalo boost within its tidal radius, we will use an equation analogous to equation 3.2 but with the density profile of the subhalo and the truncated at the tidal radius. The density profile of a surviving tidally truncated subhalo is expected to change from the initial density profile as the substructure orbits within its host [76]. This density profile is a modification of the NFW profile which is given as

$$\rho_{\text{sub}} = \frac{f_t}{1+(r/r_t)^3}\rho_{\text{NFW}}, \tag{3.17}$$

where f_t measures the change in the central density due the tidal heating and r_t is the tidal radius. For the purpose of our simple estimates, we will assume that the central density is unaffected by tidal heating and take $f_t = 1$. Given the density profile of a surviving subhalo in a host, the boost from that subhalo, f_{sub} is given as

$$f_{sub} \equiv \frac{\int \rho_{\text{sub}}^2 dV}{\bar{\rho}_{\text{sub}}^2 V}, \tag{3.18}$$

which is estimated within the tidal radius r_t. Given a subhalo that fell into the host with some initial mass, m_o and radius, r, and tidally stripped to a later mass m and r_t, we will denote the bound mass fraction as $\kappa \equiv \frac{m}{m_o}$. In line with [76], we will assume that this bound mass fraction at $z = 0$ is given as $\kappa(z = 0) = 0.2 + 0.8\exp(-z_{_{infall}})$, where $z_{_{infall}}$ is the infall redshift of the subhalo. This expression implies that subhaloes/material that fell in at an earlier time are expected to be bounded the least. For a host at a redshift, z, the bound mass fraction is given as $\kappa(z) = 0.2 + 0.8\exp[-(\frac{a}{a_{_{infall}}} - 1)]$, where a and $a_{_{infall}}$ are the scale factors that correspond to z ad $z_{_{infall}}$ respectively. Given an expression for the bound mass fraction, the tidal radius is chosen such that it satisfies the following equation for the NFW profile at all redshifts:

$$\frac{m'(< r_t)}{m(< r)} = \kappa(z).$$

2. Mass fraction per individual subhalo

   To calculate the mass contribution to the host from each subhalo, we first need to understand how the halo accretes mass over time. This accumulation of mass is described using the mass accretion history (MAH) of the halo. Given an analytic form of the MAH of the halo as a function of redshift, M (z), the mass accumulated in small redshift steps is given as $dM = (dM/dz)\Delta z$. This build-up in mass includes both bound and smooth material. To account for the bound material, the accumulated mass will be modulated by the fraction of bound haloes of a given mass in

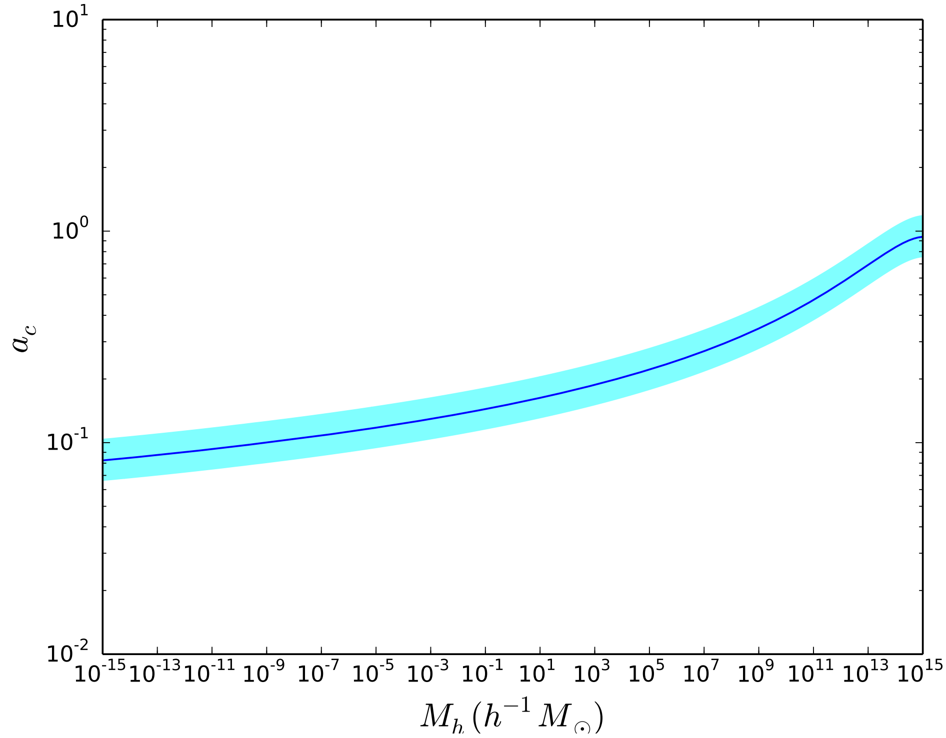

Figure 3.5: The range of formation times, in terms of the scale factor, for various halo masses following the prescription of [170].

the universe at a particular redshift, $f_{bh}(M, z)$. Not every bound material initially accreted survives due to the tidal force of the host halo, thus the surviving mass of subhaloes is the accreted material modulated by the surviving bound mass fraction, $\kappa(z)$. Mathematically, the mass fraction in subhaloes of a given mass at $z = 0$ is given by

$$X_{sub}(M; z = 0) = \frac{1}{M_0} \int_0^\infty \frac{dM}{dz} f_{bh}(M, z) \kappa(z = 0) dz, \tag{3.19}$$

where M_0 is the host halo mass at $z = 0$. To estimate this subhalo mass fraction at $z = 0$, we will assume the form of the mass accretion history given by [170], related to the scale factor at the formation epoch of the halo, a_c and concentration of the halo at $z = 0$, c. The MAH is expressed as $M(z) = M_0 \exp(-2a_c z) = M_0 \exp(-\frac{8.2z}{c})$. Figure 3.5 shows the mean formation scale factor and scatter for different halo masses. For redshifts different from zero, the mass fraction in substructure may be generalized to

$$X_{sub}(M; z' \neq 0) = \frac{1}{M(z')} \int_{z'}^\infty \frac{dM}{dz} f_{bh}(M, z)\, \kappa(z)\, dz \tag{3.20}$$

The fraction of a given mass in haloes at a given redshift $f_{bh}(M, z)$ is expressed as

$$f_{bh}(M, z) = \int_M^{M+\Delta M} \frac{m}{\rho_m} \frac{dN}{dm}(m, z) dm, \tag{3.21}$$

where $\frac{dN}{dm}(m, z)$ is the halo mass function – the number density of haloes of a given mass at a given redshift – and ρ_m is the mean matter density of the universe. This fraction has been estimated using the halo mass function of [140]. Thus, the mass fraction in subhaloes of different masses can be estimated at different redshifts.

3. Density enhancement of each subhalo relative to the main halo

   The final parameter that needs to be estimated is the enhancement of the subhalo density relative to that of the host halo. Prior to being accreted into the host, a subhalo is assumed to be virialized on average at a given redshift z, and should have a density of $200\rho_c(z)$, where $\rho_c(z)$ is the critical density of the universe at that redshift. However, since the subhalo ends up being tidally stripped, this factor increases by the ratio of the mean density within the tidal radius to the mean density within its virial radius r_{vir} at the time of accretion. Thus,

$$\begin{aligned}\frac{\bar{\rho}_{sub}(z)}{\bar{\rho}_h} &= \frac{\rho_c(z)\bar{\rho}(<r_t)}{\rho_c(0)\bar{\rho}(<r_{vir})} \\ &= \frac{\rho_c(z)m'(<r_t)r_t^3}{\rho_c(0)m(<r_{vir})r_{vir}^3} \\ &= \kappa(z)\frac{\rho_c(z)r_t^3}{\rho_c(0)r_{vir}^3} \qquad (3.22)\end{aligned}$$

Putting all these factors together results in the estimation of a modified form of equation 3.16 which is given as

$$\frac{f_h}{f_{\rm sm}} = (1-X) + \sum_{i\,\in\,\rm subhaloes} \int_0^\infty \left(\frac{\bar{\rho}_i(z)}{\bar{\rho}_h}\right)\frac{dX_i}{dz}(z)\frac{f_i(z)}{f_{\rm sm}}\Delta z\,. \qquad (3.23)$$

and shown in Figure 3.6 as a function of halo mass. The plot has been made assuming the concentration-mass relation of [94]. At a given mass M_0, all substructure with $m < M_0$ contribute to the substructure boost.

3.3 Free-Streaming Mass scale

There exists a minimal mass of structure in the cold dark matter universe, M_{lim} due to the cut-off in the primordial power spectrum of density fluctuations. This cut-off in the power spectrum may be due to the damping from the kinetic decoupling of the neutralino or that due to free-streaming after the last scattering of the neutralino [80]. The exact value for this cut-off mass scale depends on the particular details assumed for the dark matter particle. We investigate the effect of the cut-off mass of substructure by varying the limit for M_{lim} between $10^{-6}M_\odot$ and $1M_\odot$ and is shown in Figure 3.8

3.4 Signal-to-Noise Ratio

3.4.1 Signal

The gamma-ray luminosity of the halo due to dark matter annihilation is given by the boost factor calculated previously, times the halo mass, mean density, and the particle

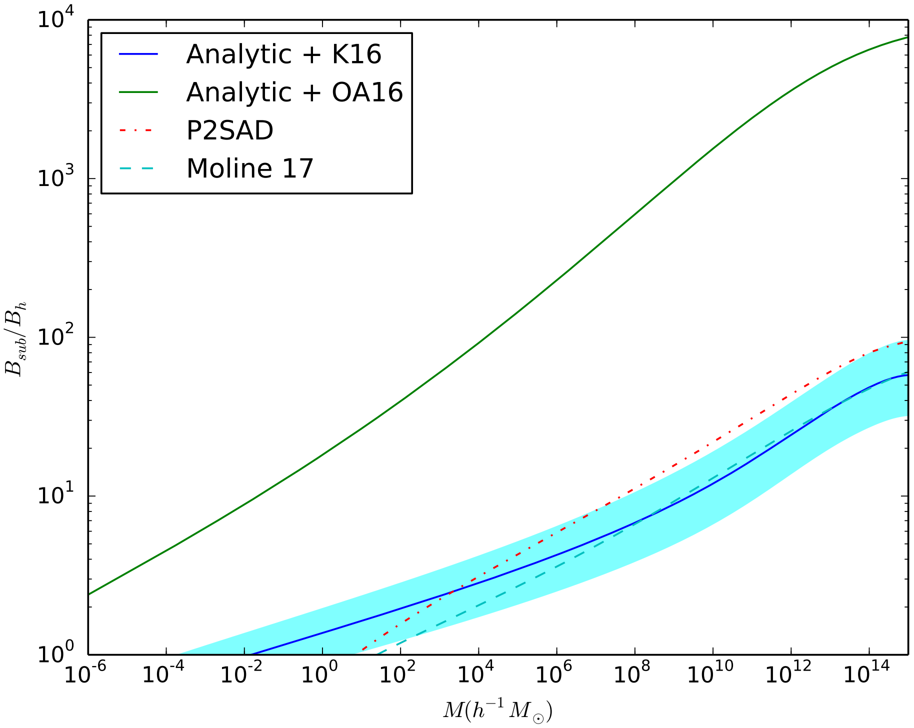

Figure 3.6: The boost from substructure relative to that of the smooth halo using two different prescriptions – P2SAD and an analytic model. Also plotted is the expectation from the tidal stripping model of [121] for $\alpha = 2$. The halo concentrations assumed are those of [94]. The cyan region illustrates the effect of different formation epochs for a given halo mass from the scatter in the halo concentration.

factors discussed in section 3.1.1:

$$L_h \equiv \frac{\langle \sigma v \rangle}{2m_\chi^2} B_{hs} 200 \times \rho_c(0) M_h N_\gamma, \tag{3.24}$$

where B_{hs} is the total boost from the halo, including the effects of substructure, M_h is the mass of the halo and N_γ is the number of photons above a given threshold, say 1 GeV, produced by a pair of WIMPs annihilating.

As a concrete example, we will assume $\langle \sigma v \rangle = 3 \times 10^{-26}\,\mathrm{cm}^3\,\mathrm{s}^{-1}$, $m_\chi = 100$ GeV, $N_\gamma = 30$ and $\Delta t = 8$ years. The effective area for the Fermi LAT is $7200\,\mathrm{cm}^2$ [1]. For these parameters, and for a source distance of $D = 10$ Mpc, figure 3.7 shows the expected counts from annihilation (top panel), from star formation (middle panel), and from the IGRB (bottom panel). The annihilation calculation assumes an NFW profile, the concentration relation of K16, and a mass limit of $m_{\mathrm{lim}} = 10^{-6} M_\odot$.

3.4.2 Baryonic Noise Sources of Gamma rays

Given the expected gamma ray signal from annihilation for individual haloes, in this section we investigate other sources of gamma ray signals that can contribute to noise that may hinder the signal. Sources of gamma rays include pulsars, cosmic rays – from their interaction with the stellar remnants of star formation such as supernovae or the gas in the galaxy – in the galaxies. The dominant source of gamma ray noise is expected to be the latter due the dominance of stars the pulsars in galaxies. Therefore, we will focus on the gamma ray signal due to activities of star formation. To this end, we will need to assign stellar masses to our haloes and then estimate the gamma ray luminosity from the star formation rates (SFR).

Haloes are usually populated with galaxies using a variety of techniques which include the abundance matching, halo occupation distribution (HOD) modelling, conditional luminosity function (CLF) modelling, and using observed galaxy properties. In this work, we will use the five-parameter function for the stellar mass-halo mass (SMHM) relation at $z = 0$ given by [23]. This relation, chosen to maximize the likelihood of being consistent to the observational constraints of stellar mass function (SMF), specific star formation rate (SSFR) of galaxies, and the cosmic star formation rate (CSFR) at redshifts ($z = 0$ to $z = 8$), may be expressed as

---

[1] http://www.slac.stanford.edu/exp/glast/groups/canda/lat_Performance.htm

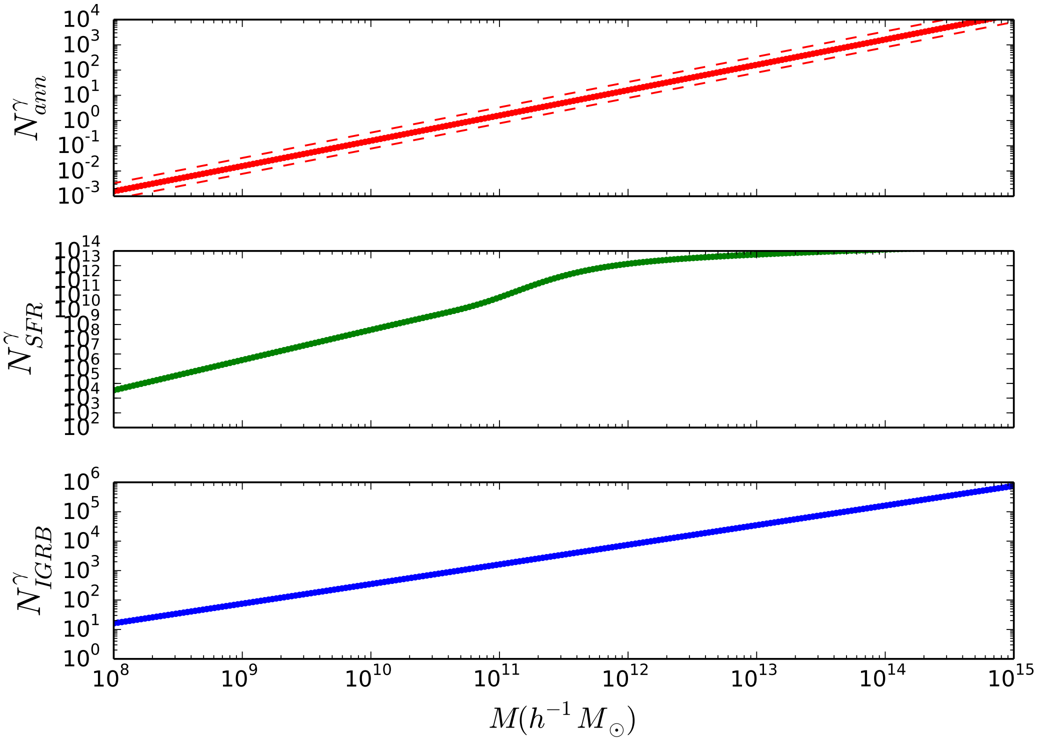

Figure 3.7: Gamma-rays produced by dark matter annihilation (top panel) ,star formation (middle panel), and from the IGRB (bottom panel), as a function of halo mass. The annihilation counts assume a velocity-averaged annihilation cross-section $\langle \sigma v \rangle = 3 \times 10^{-26}\,\mathrm{cm}^3\,\mathrm{s}^{-1}$, a WIMP mass of $m_\chi = 100$ GeV, $N_\gamma = 30$, and an observing time of $\Delta t = 8$ years, for the Fermi LAT (effective area $7200\,\mathrm{cm}^2$). The boost factor used assumes a NFW profile, the concentration relation of K16, and a mass limit of $m_{\mathrm{lim}} = 10^{-6} M_{\odot}$. The star formation counts assume the luminosity-SFR relation from equation 3.25.

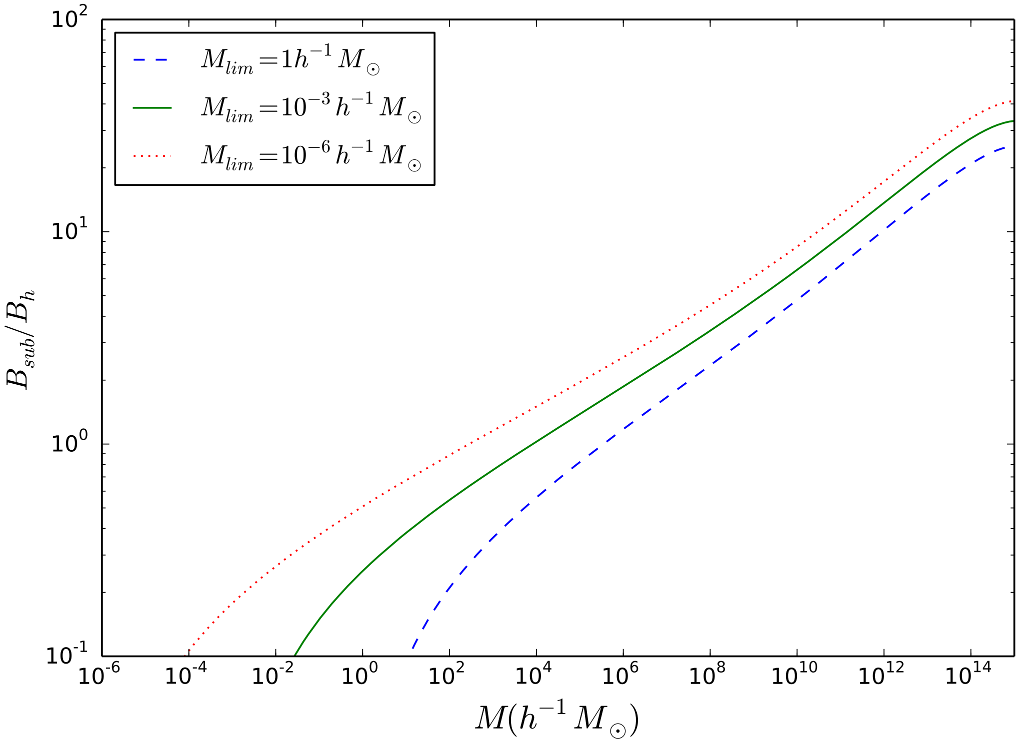

Figure 3.8: The boost from substructure, relative to the smooth halo boost factor, as a function of halo mass, for three different values of the lower mass limit to CDM structure, $M_{\rm lim}$. In each case, we have assumed a NFW profile with the concentration-mass relation of K16.

Star Formation

Star-forming regions produce cosmic rays, whose interactions with molecular gas in turn lead to pion creation. The resulting decays produce gamma-ray emission at energies where it could mask dark matter annihilation. Earlier work by [3] and [5] showed that the total gamma-ray luminosity seen by *Fermi LAT* above 100 MeV correlates closely with the star formation rate (SFR) for the nearby galaxies that have been detected individually. More recently, gamma-ray emission from star-forming galaxies has been considered in detail by a number of authors e.g [157, 22, 133]. For the purpose of this calculation, however, we will assume the simple empirical relationship of [3]:

$$L_{\mathrm{SFR}} = 7.4 \times (\mathrm{SFR})^{1.4}, \tag{3.25}$$

where L is in units of 10^{41} photons s^{-1}, and the SFR is in $M_\odot\,\mathrm{yr}^{-1}$.

We use the stellar-to-halo-mass-ratio (SHMR) relation of [23] at $z = 0$ to estimate the mean stellar mass of the central galaxy in a given halo. This five-parameter function was derived by fitting the stellar mass functions and specific star formation rates of galaxies at redshifts $z = 0$–8, as well as the cosmic star formation rate over this range. It may be expressed as

$$\log_{10}(M_*(M_h)) = \log_{10}(\epsilon M_1) + f\left(\log_{10}\left[\frac{M_h}{M_1}\right]\right) - f(0), \tag{3.26}$$

where

$$f(x) \equiv -\log_{10}(10^{\alpha x} + 1) + \delta\frac{(\log_{10}(1 + \exp(x)))^\gamma}{1 + \exp(10^{-x})}\,.$$

For $z = 0$, the parameters, α, δ, γ, $\log_{10}\epsilon$, and $\log_{10} M_1$ have best-fit values -1.412, 3.508, 0.316, -1.777, and 11.514 respectively.

Given the stellar mass of the central galaxy, we then estimate its mean star formation rate, by assuming the galaxy lies on the 'star formation main sequence' e.g. [147], such that

$$\log_{10}\mathrm{SFR} = \alpha\log_{10}\left(\frac{M_*}{M_{9.7}}\right) + \beta, \tag{3.27}$$

where α, β, and $M_{9.7}$ are 1.04, 1.01 and $10^{9.7}M_\odot$ respectively, and the SFR is in units of $M_\odot\,\mathrm{yr}^{-1}$. Given this rate, we can derive a gamma-ray luminosity due to star-formation from equation 3.25 above.

With increasing exposure, Fermi LAT has detected gamma-ray emission from a number of individual galaxies e.g. [3, 7], and possibly also from some galaxy clusters [149]. Most recently, [7] found emission from the centre of M31 that could indicate dark matter annihilation, though it may also come from more mundane sources such as pulsars. In general, for typical galaxies a stronger contaminant in dark matter annihilation searches are the contributions from the isotropic gamma-ray background (IGRB) [6], ongoing star formation within the galaxy itself, and/or emission from an active galactic nucleus. While it should be possible to avoid galaxies with AGN and/or spatially resolve out this emission in the nearest galaxies, star formation is more ubiquitous and spread out, and thus harder to avoid, while the contribution from the IGRB is unavoidable. Thus, we will focus on star formation and the IGRB as the most important noise source in annihilation searches, at least for haloes of group-scale or lower mass.

The IGRB

The diffuse isotropic gamma ray background (IGRB) is an all-sky gamma-ray emission from unresolved sources after accounting for resolved sources, diffuse Galactic emission, the Cosmic Ray background, and the Solar contribution from the total all-sky background. Measurements of the IGRB using the LAT detector of the Fermi Gamma ray Space Telescope at energies from 100 MeV to 820 GeV from over fifty months of LAT data indicate an integrated intensity for energies above 100 MeV of 7.2×10^{-6} photons $\mathrm{cm}^{-2} s^{-1} \mathrm{sr}^{-1}$ [6]. Using this intensity, the estimated luminosity from the IGRB from individual haloes is given by

$$L_{IGRB} = 7.2 \times 10^{-6} 4\pi R_{200}^2, \tag{3.28}$$

where R_{200} is the virial radius of the halo.

3.4.3 Signal-to-Noise Ratio

Observing a source at distance D for a time Δt with a detector of effective area A_{det}, the signal-to-noise ratio is then given as

$$SNR = \frac{L_h A_{\mathrm{det}} \Delta t / 4\pi D^2}{\sqrt{(L_{\mathrm{SFR}} + L_h + L_{IGRB}) A_{\mathrm{det}} \Delta t / 4\pi D^2}} \, . \tag{3.29}$$

where A_{det} is the Fermi LAT detector area, D is the estimated distance to a halo, and Δt is the observation time.

To estimate the signal-to-noise of the annihilation signal for an individual halo, we will estimate the stellar mass of its central galaxy, the typical star formation rate for an object with that stellar mass, and the resulting gamma-ray luminosity from star formation and the IGRB using the relation above (Equation 3.29). We will then compare this 'noise' to the 'signal' (Section 3.4.1)

We can consider the SNR in two cases, either that we observe different haloes at a fixed distance, or that for each halo mass, we find and observe the nearest system. The average distance to the nearest halo of mass M in a cosmological volume will be related to the number density of haloes of that mass by $D = n(M)^{-1/3}$. Thus, given a halo mass function $n(M)$, we can calculate $D(M)$ and use this in equation 3.29 to get the SNR for a typical closest source, as a function of halo mass.

Finally, the dashed (blue) curves on figure 3.9 show the importance of halo-to-halo scatter; considering the effect on dark matter structure alone, there should be a factor of 2 or more scatter in the SNR for individual haloes. Since the primary origin of this scatter is the variation in halo concentration, independent estimates of this quantity could help select more promising objects for stacking. Variations in SFR will increase this variation further. For fixed dark matter properties, targeting passive galaxies in concentrated haloes may yield SNRs many times those of the median relation.

3.5 Discussion and Conclusion

To estimate the signal from annihilation for individual halos, the boost factors from smooth haloes and substructure will have to be taken into account including the uncertainties in the halo concentration. In addition to focusing on the uncertainties that arise in the predictions of the dark matter annihilation, we have developed an analytical estimate for the signal-to-noise ratio(SNR) as a function of individual halo mass that includes the scatter due to halo concentration. Our estimates have been made using a conservative model of the halo concentration and include the effects of baryonic noise from the background gamma-ray radiation and that due to the formation of stars in the host galaxy(ies) present in the halo. As seen in Figure 3.6, our estimates compare pretty well with those of [121] for the same halo concentration model.

Based on our estimates, one can see that nearby groups of galaxies are good targets for annihilation detection. Given that the biggest source of disparity arises due to variation in halo concentration at the low-mass end that dominates the uncertainty in the estimated boost from structure for the annihilation signal, more work is probably needed to understand the concentration of micro haloes or at least to investigate the limiting mass for surviving substructure orbiting in haloes today through simulations or observations.

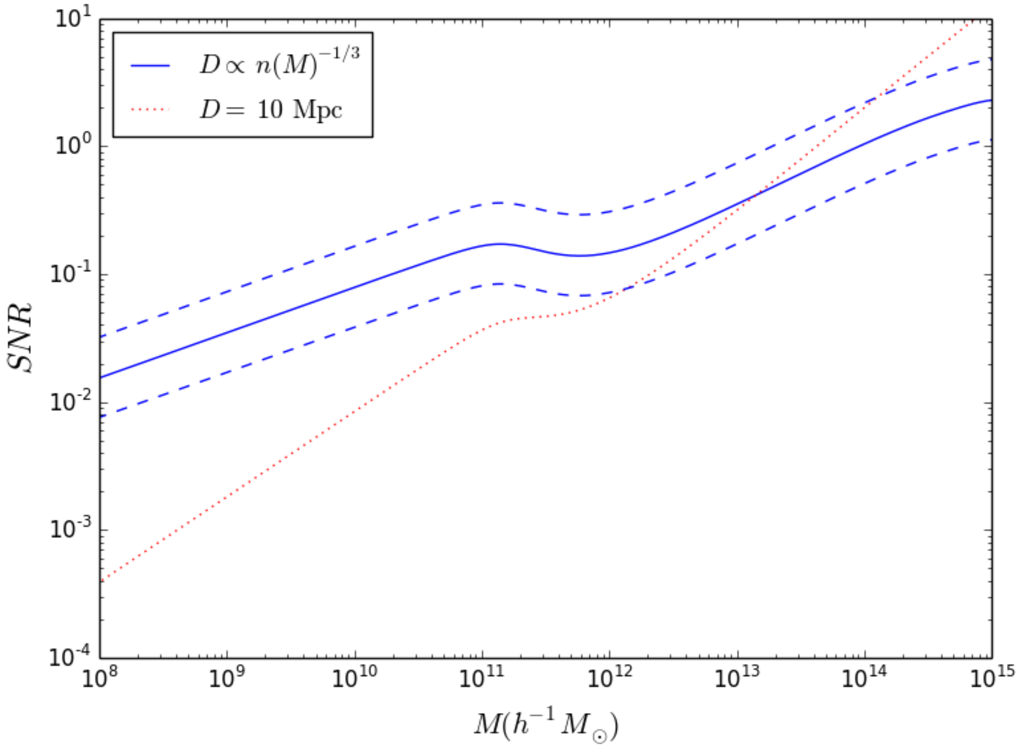

Figure 3.9: The SNR of the annihilation signal in our fiducial calculation, as a function of halo mass. The solid (blue) curve assumes we observe the nearest halo of that mass, at a distance scaling as $D = n(M)^{-1/3}$. The dotted (red) curve assumes we observe haloes at a fixed distance of 10 Mpc, independent of mass. The dashed lines show the 68% halo-to-halo scatter, due primarily to differences in concentration.

Chapter 4

Cosmological Neutrinos

Neutrinos are an interesting component of the Standard Model of particles that play a number of unique roles in particle physics, astroparticle physics and cosmology. In the Standard Model of particle physics, they are depicted as massless and not clearly associated as Majorana or Dirac particles. Observations of flavour oscillations in solar and atmospheric neutrinos point to the existence of neutrino mass. In cosmology, the presence of massive active[1] neutrinos potentially resolves some of the tension between the observed galaxy counts and those predicted by the *Planck* cosmological parameters as suggested by [175, 21, 29].

Constraints on the mass-squared difference of neutrinos via oscillation experiments give best-fit values of $\Delta m_{12}^2 \equiv m_2^2 - m_1^2 = 7.54 \times 10^{-5}\mathrm{eV}^2$ and $\Delta m_{13}^2 \equiv m_3^2 - (m_1^2 + m_2^2)/2 = 2.43(2) \times 10^{-3}\mathrm{eV}^2$ for the normal (inverted) hierarchy [64, 113]. These constraints lead to a lower limit on the sum of the masses of these neutrinos, $M_\nu \equiv \sum_i m_i > 0.058\,\mathrm{eV}$ for the normal hierarchy and $M_\nu > 0.11\,\mathrm{eV}$ for the inverted hierarchy. See [101, 102] for a more comprehensive review of the role of massive neutrinos in cosmology. Thus, any limit on $M_\nu < 0.1\,\mathrm{eV}$ rules out the inverted neutrino hierarchy. Alternative limits on the sum of the neutrino mass M_ν may also be placed by cosmological observations and measurements. Although some degeneracy exists between the Hubble constant and the neutrino mass on the background cosmology, the cosmic microwave background (CMB) temperature perturbations are affected by the neutrino mass through the early-time integrated Sachs-Wolfe (ISW) effect and the lensing effect on the power spectrum. The baryon acoustic oscillations (BAO) and measurements of the CMB temperature anisotropy have placed limits on the sum of the mass of the neutrinos as $M_\nu < 0.23\,\mathrm{eV}$ [135]; albeit, slightly dependent on the

---

[1] In contrast to being sterile

assumed cosmological model parameters. First described by [33], galaxy surveys present yet another method to constrain the mass of neutrinos as presented in [142]. Suppression of structure below the free-streaming scale of the neutrinos, when they first become non-relativistic, leads to a decline in the matter power spectrum (usually at the per cent level). However, in practice, galaxy power spectra are measured and so precise knowledge of the galaxy bias as a function of scale is required since the galaxies do not cluster as matter. Notwithstanding, [142] explored this technique in the WiggleZ Dark Energy Survey and placed an upper limit on the sum of the neutrino masses, $M_\nu < 0.18\,\mathrm{eV}$ for three degenerate neutrino species with no prior placed on the minimum sum of neutrino masses. More recent estimates by [43] using the WiggleZ Dark Energy Survey and SDSS-DR7 LRG, together with the BAO and CMB temperature and polarisation anisotropies measurements by *Planck* have yielded even tighter constraints of $M_\nu < 0.13\,\mathrm{eV}$ at the 95% C.L. on the sum of the neutrino masses

A complementary technique to measure the neutrino masses using their peculiar velocities relative to dark matter has been suggested by [183]. The relative velocity between the neutrinos and dark matter leads to an observable dipole distortion in the cross correlation of different tracers. This effect is similar to the relative velocity between baryons and cold dark matter, first suggested by [163] and explored in a number of other works, including [176]. The neutrino particles stream coherently across the CDM haloes over a coherence/Jeans scale of $20 - 50\ h^{-1}$Mpc.

In this chapter, we provide a semi-analytic derivation of this effect in the nonlinear regime, which is equivalent to the dynamical friction for CDM haloes moving in the primordial neutrino sea. The outline is as follows: Section 4.1 introduces the relations between velocities and density perturbations for both neutrinos and cold dark matter in the linear regime. Section 4.2 examines the effect of dynamical friction on the dark matter structures due to the streaming neutrinos. We then present the methodology, and expected signal to noise for detecting this effect in current and future surveys in Section 4.3. Finally, Section 4.4 summarizes our results and concludes the chapter, while the appendices A.1 and A.2 provide details of signal-to-noise calculations, and comparison to nonlinear effects in ΛCDM simulations without neutrinos.

For the calculations below, we use a ΛCDM CAMB [104] power spectrum with *Planck*[2] parameters $(\Omega_{m0}, \Omega_{\Lambda 0}, \Omega_{0b}) = (0.32, 0.68, 0.049)$, Hubble parameter $h = 0.67$, rms (root mean square) density fluctuation in $8\,h^{-1}$ Mpc spheres, $\sigma_8 = 0.8344$ and scalar spectral index $n_s = 0.963$. We also utilize the analytic power spectrum of [59] where necessary. The dark energy density and total matter density $\Omega_{m0} = \Omega_{c0} + \Omega_{b0} + \Omega_{\nu 0}$ are kept fixed

---

[2] [135]. We use the Planck-only best fit values.

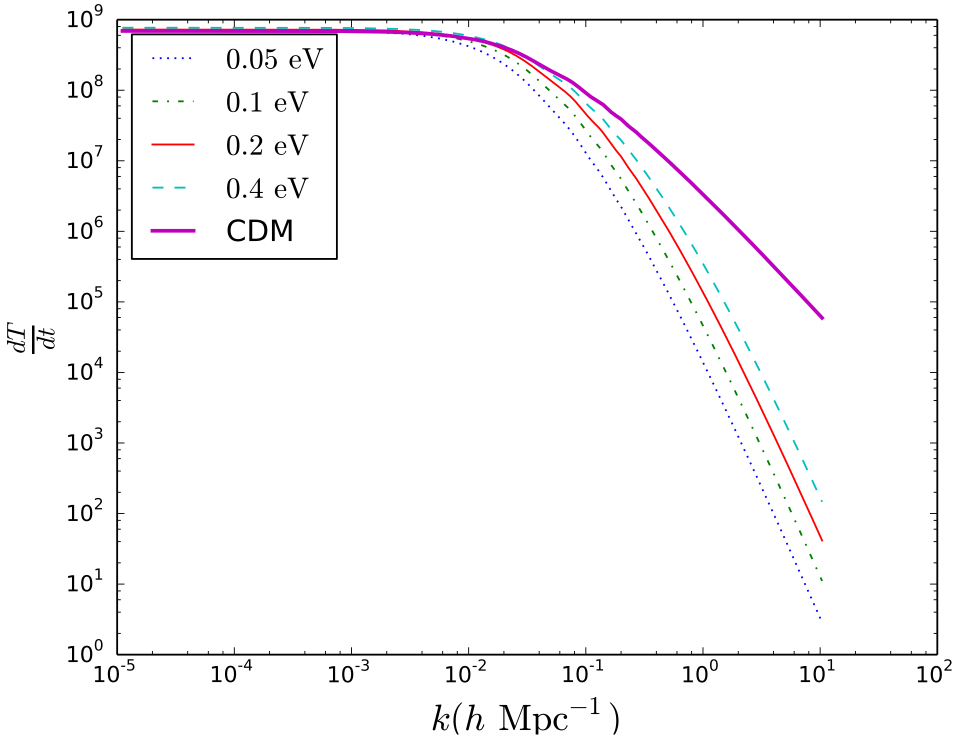

Figure 4.1: Time derivative of the transfer function, $\dot{T}(k) = dT(k)/dt$, at $z = 0$ for cold dark matter and neutrinos of different masses.

while the cold dark matter density Ω_{c0} and the neutrino density $\Omega_{\nu 0}$ are adjusted as needed. The relation between the neutrino density and neutrino mass is given by

$$\Omega_{\nu 0} = \frac{\sum_{i=1}^{3} m_i}{94.07 h^2\,\mathrm{eV}}, \tag{4.1}$$

with the sum being over the three neutrino species. We assume an effective number of relativistic species $N_{\mathrm{eff}} = 3.046$ [135]necessary for estimating the power spectrum from CAMB. The notation $M_\nu \equiv \sum_{i=1}^{3} m_i$ will be mostly used to replace the sum over neutrino mass in the rest of this chapter.

4.1 The Neutrino - CDM relative velocity

We proceed to calculate the CDM-neutrino relative velocity power spectrum following [163] and [183]. The relative velocity, as we will see in the next section, is relevant for estimating the dynamical friction on a halo due to neutrinos. Assuming the linearized continuity equation holds for both neutrinos and cold dark matter (on scales $k \lesssim 1\mathrm{h/Mpc}$), in Fourier space it is given by

$$\boldsymbol{v}(k) = -\frac{i\boldsymbol{k}a}{k^2}\dot{\delta}(k) \tag{4.2}$$

where $a = 1/(1+z)$ is the cosmic scale factor and we have assumed that there is no vorticity (curl of the vector perturbation is zero). This is tested in [85], where the velocity was seen to be curl-free on scales $k \lesssim 1\mathrm{h/Mpc}$.

The variance in the relative velocity $\boldsymbol{v}_{\nu c} \equiv \boldsymbol{v}_\nu - \boldsymbol{v}_c$ between neutrinos (ν) and cold dark matter (c) can be calculated to be

$$\begin{aligned}\langle v_{\nu c}^2(R,a)\rangle &= \frac{a^2}{2\pi^2}\int k^2 dk \left[\frac{\dot{\delta}_\nu(k,a) - \dot{\delta}_c(k,a)}{k}\right]^2 \widetilde{W}^2(kR) \\ &= a^2 \int \frac{dk}{k}\Delta^2_{v\nu c}(k,z)\widetilde{W}^2(kR)\end{aligned} \tag{4.3}$$

where $\widetilde{W}(kR)$ is the Fourier transform of the window function, and $\Delta^2_{v\nu c}(k,z)$ is the neutrino - cold dark matter relative velocity power spectrum. The essence of the window function is to filter the velocity perturbation field to get a smooth field. We will adopt one of the most commonly used window functions – the spherical top-hat [3]– defined as

$$W(x;R) = \left(\frac{4\pi}{3}R^3\right)^{-1} \begin{cases} 1 & \text{for } |x| \leq R \\ 0 & \text{for } |x| \geq R. \end{cases} \tag{4.4}$$

In Fourier space, it is given by

$$\widetilde{W}(kR) = \frac{3j_1(kR)}{kR}, \tag{4.5}$$

where j_1 is the first order spherical Bessel function. The relative velocity power spectrum can be written in terms of the transfer functions of neutrinos and CDM as

$$\Delta^2_{v\nu c}(k,z) = \mathcal{P}_\chi \left[\frac{\dot{T}_\nu(k,z) - \dot{T}_c(k,z)}{k}\right]^2, \tag{4.6}$$

---

[3] The advantage of using top-hat window function is that it is localized in real space, and thus can be applied to finite real-space data. However, we do not expect our conclusions to be sensitive to this choice.

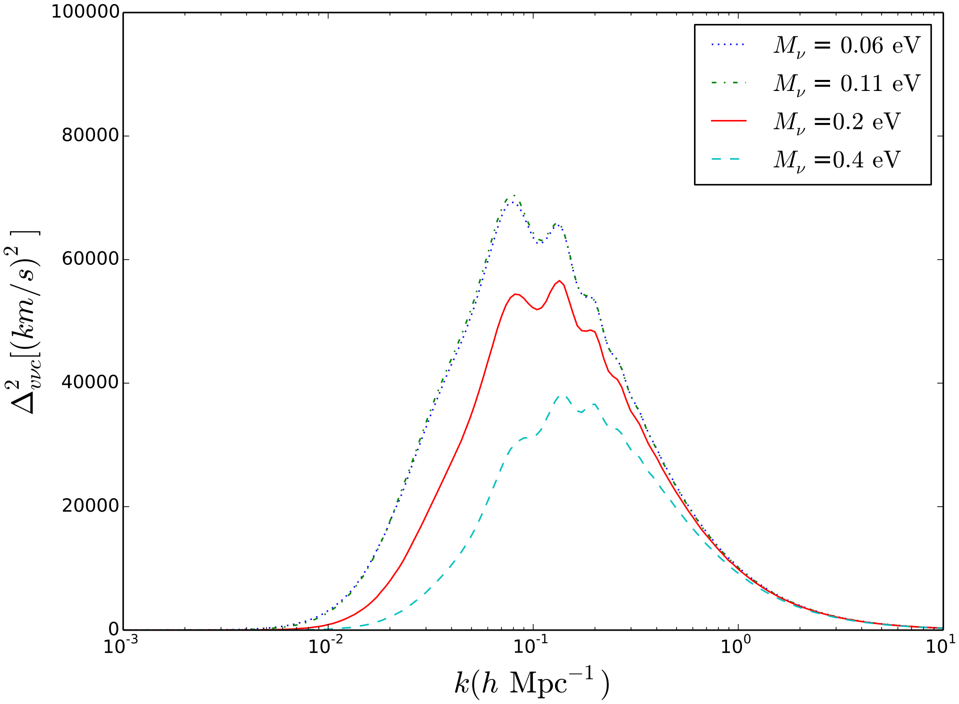

Figure 4.2: The power spectrum of the relative velocity between the neutrinos and cold dark matter. The different curves represent different values of $M_\nu = \sum m_\nu$ (assuming normal hierarchy). This plot is reproduced from [183]. The two lowest M_ν's are close due to the fact that the most massive of the three neutrinos in each sum have similar masses and dominate in the sum.

where $\mathcal{P}_\chi \propto k^{n_s+3}/(2\pi^2)$ is the primordial power spectrum of density perturbations and $\dot{T}(k,z)$ is the time derivative of the transfer function at redshift z.

We show the derivative of the transfer function, $\dot{T}$, at $z = 0$ for cold dark matter and neutrinos of different masses, in Figure 4.1, which demonstrates the impact of free steaming on their density perturbations. As expected, more free streaming leads to more suppression of growth on small scales for lighter neutrinos. The relative velocity power spectrum for different sum of neutrino masses (unless otherwise stated, all sum of neutrino masses assume the normal hierarchy) is shown in Figure 4.2.

Obviously in Figure 4.2, the power lies in the range $k \sim [0.01, 1]$. The rms relative velocity $v_{\nu c}$ within a sphere as a function of the radius of the window function used is shown in Figure 4.3 for different sum of neutrino masses.

4.2 Dynamical Friction

Dark matter haloes sitting in a streaming background of neutrinos will experience a deceleration due to dynamical friction. Larger haloes experience a larger dynamical friction force than smaller-mass haloes, and so larger- and smaller- mass haloes will have different displacements relative to the neutrino streaming direction.

In this section, we calculate the general structure of massive neutrino wakes, and their dynamical friction force on dark matter haloes with an NFW profile. This drag on the halo should lead to a displacement, which is nonexistent in the absence of neutrinos. This displacement Δx, in the halo's position, will be first estimated by approximating dark matter haloes as single spheres in Section 4.2.1. We then develop the general formalism for computing the neutrino wake in Fourier space in Section 4.2.2, and use it to derive dynamical friction assuming the full halo model in Section 4.2.3. The halo model consists of contributions from the 1-halo and 2-halo terms. We shall see that, while the 1-halo term is equivalent to the solid sphere approximation, the 2-halo term dominates the drag on small haloes.

4.2.1 Solid sphere approximation

The phase-space distribution of neutrinos is given by the Fermi-Dirac distribution:

$$d\mathcal{N}_\nu = \frac{d^3x d^3p}{(2\pi\hbar)^3} f_\nu(\boldsymbol{p}) = \frac{d^3x d^3p}{(2\pi\hbar)^3} \frac{2N_\nu}{\exp(pc/T_\nu)+1}, \tag{4.7}$$

where

$$T_\nu = \left(\frac{4}{11}\right)^{1/3} T_{\rm CMB} \simeq 1.95\,{\rm K}, \tag{4.8}$$

where $T_{\rm CMB}$ is the temperature of the CMB today, and N_ν is the number of massive neutrino species. In the rest frame of a dark matter halo that moves with velocity $\boldsymbol{v}_{\nu c}$ relative to the neutrinos, the phase-space density takes the form:

$$\begin{aligned} f_\nu(\boldsymbol{p}) &= \frac{2N_\nu}{\exp(|\boldsymbol{p} + m_\nu \boldsymbol{v}_{\nu c}|c/T_\nu) + 1} \\ &\simeq \frac{2N_\nu}{\exp(pc/T_\nu)+1} - \frac{N_\nu m_\nu c\, \boldsymbol{v}_{\nu c}\cdot \boldsymbol{p}}{pT_\nu[1+\cosh(pc/T_\nu)]} + \mathcal{O}(v_{\nu c}^2), \end{aligned} \tag{4.9}$$

with the factor of 2 accounting for antineutrinos along with neutrinos. The dynamical friction force is then given by integrating over all range of impact parameter, b and over a dark matter halo of mass, say M_h:

$$\begin{aligned} \boldsymbol{F} &= \int (2\pi b db) \frac{2[GM_h(<b)]^2 m_\nu^3}{b^2} \int \frac{d^3p}{(2\pi\hbar)^3} f_\nu(\boldsymbol{p}) \frac{\boldsymbol{p}}{p^3} \\ &= -\frac{2N_\nu m_\nu^4 \boldsymbol{v}_{\nu c}}{3\pi\hbar^3} \int \frac{db}{b} [GM_h(<b)]^2 \\ &\simeq -\frac{2N_\nu \ln(\Lambda)(GM_h)^2 m_\nu^4 \boldsymbol{v}_{\nu c}}{3\pi\hbar^3}. \end{aligned} \tag{4.10}$$

Notice that the terms in the integral are similar to the well-known Chandrasekhar dynamical friction formula [31]. The first term in the first integral accounts for the range of impact parameters of interaction between the neutrino and the halo. The second term in the first integral is the drag force due to an interaction between a neutrino and a halo. The second integral incorporates the density distribution of the neutrinos. Using Newton's 2nd law, $\boldsymbol{F} = M\dot{\boldsymbol{v}}$, we can find the change in relative velocity due to dynamical friction, over a Hubble time $t \simeq H^{-1}$:

$$\begin{aligned} \frac{\Delta v_{\nu c}}{v_{\nu c}} &= \frac{2N_\nu \ln(\Lambda) G^2 M_h m_\nu^4}{3\pi H \hbar^3} \\ &= 5.6\times 10^{-3}\, h^{-2} \left(\frac{\ln\Lambda}{\ln 30}\right) \left(\frac{M_h}{10^{15} h^{-1} M_\odot}\right) \\ &\quad \left(\frac{N_\nu}{3}\right) \left(\frac{m_\nu}{0.1\ {\rm eV}}\right)^4, \end{aligned} \tag{4.11}$$

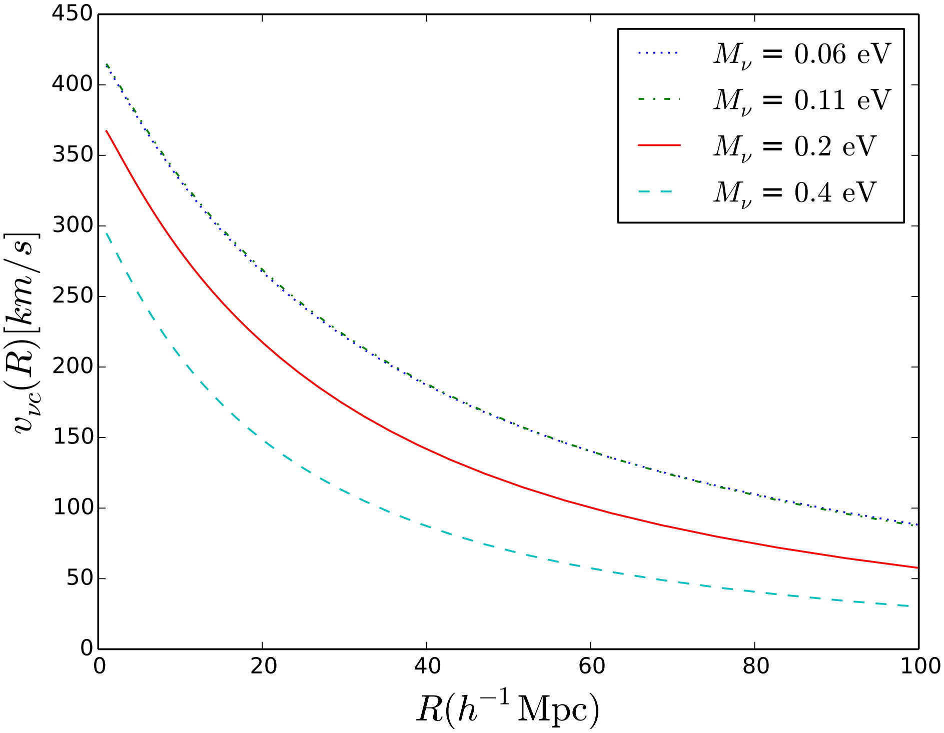

Figure 4.3: Relative CDM-neutrino velocity $v_{\nu c}$ as a function of top hat window function radius R, for four different neutrino masses.

where $H = H(z)$ is the Hubble constant, h is the Hubble parameter, and $\ln\Lambda = \int db/b$ is the Coulomb logarithm. $\ln\Lambda \equiv \ln\frac{b_{max}}{b_{min}}$, where b_{max} and b_{min} are the maximum and minimum impact parameters respectively. Here we use $b_{max} \sim 30$ Mpc as the typical neutrino free steaming length, and $b_{min} \sim 1$ Mpc as the typical size of CDM haloes. This leads to an average displacement over a Hubble time of:

$$\begin{aligned}\Delta x &= \frac{1}{2}\Delta v_{\nu c} \times t \\ &= 6.66\, h^{-3}\,\mathrm{kpc}\left(\frac{v_{\nu c}}{236\ \mathrm{km/s}}\right)\left(\frac{\ln\Lambda}{\ln 30}\right) \\ &\quad \left(\frac{M_{200}}{10^{15}h^{-1}M_\odot}\right)\left(\frac{N_\nu}{3}\right)\left(\frac{m_\nu}{0.1\ \mathrm{eV}}\right)^4 . \end{aligned} \tag{4.12}$$

If there exist different neutrino mass eigenstates, these will have different velocities and different displacements, which can be calculated independently. The total displacement is equal to the sum of displacements due to each neutrino species i, so that $\Delta x_{\mathrm{tot}} = \sum_i \Delta x_i$.

4.2.2 Dynamical friction: general formalism

Now, let's consider a more realistic dark matter distribution. For large thermal velocity of neutrinos $\frac{T_\nu}{m_\nu c} \gg v_{\mathrm{halo}}$, we can assume a steady state neutrino distribution, i.e. it satisfies the time-independent Boltzmann equation:

$$\frac{p^i}{m_\nu}\frac{\partial f_\nu(\mathbf{x},\mathbf{p})}{\partial x^i} - m_\nu \nabla_i \Phi(\mathbf{x})\frac{\partial f_\nu(\mathbf{x},\mathbf{p})}{\partial p^i} = 0, \tag{4.13}$$

where $\Phi(\mathbf{x})$ is the gravitational potential of CDM structure. This approximation is also valid in comoving phase space on large scales, as long as the neutrino thermal velocity exceeds the Hubble flow, i.e. $\Delta x \lesssim 25\ \mathrm{Mpc}\,(m_\nu/0.1\ \mathrm{eV})^{-1}$.

To linear order in Φ (in line with the assumption of linear regime), we can consider linear perturbations $\delta f(\mathbf{x},\mathbf{p}) = f(\mathbf{x},\mathbf{p}) - \bar{f}(\mathbf{p})$ in Fourier space:

$$(\mathbf{p}\cdot\mathbf{k})\delta f_{\nu,\mathbf{k}}(\mathbf{p}) = m_\nu^2 \Phi_{\mathbf{k}}\left(\mathbf{k}\cdot\frac{\partial \bar{f}(\mathbf{p})}{\partial \mathbf{p}}\right). \tag{4.14}$$

The density of the neutrinos in Fourier space is:

$$
\begin{aligned}
\delta\rho_{\nu,\mathbf{k}} &= m_\nu \int \frac{d^3p}{(2\pi\hbar)^3}\, \delta f_{\nu,\mathbf{k}}(\mathbf{p}) \\
&= m_\nu^3 \Phi_{\mathbf{k}} k^i \int \frac{d^3p}{(2\pi\hbar)^3} \frac{1}{\mathbf{p}\cdot\mathbf{k}} \frac{\partial \bar{f}(\mathbf{p})}{\partial p^i} \\
&= 2N_\nu m_\nu^3 \Phi_{\mathbf{k}} k^i \int \frac{d^3p}{(2\pi\hbar)^3} \\
&\quad \left[\frac{1}{(\mathbf{p}-m_\nu \boldsymbol{v}_{\nu c})\cdot\mathbf{k}} \frac{\partial\left[\exp(|\mathbf{p}|c/T_\nu)+1\right]^{-1}}{\partial p^i}\right],
\end{aligned}
\tag{4.15}
$$

where we have changed the integration variable $\mathbf{p} \to \mathbf{p} - m_\nu \boldsymbol{v}_{\nu c}$ in the last step, and used the shifted Fermi-Dirac distribution. We can write the integral in spherical coordinates (using $\mathbf{p}\cdot\mathbf{k} = p|\mathbf{k}|\cos\theta$):

$$
\begin{aligned}
\delta\rho_{\nu,\mathbf{k}} &= 2N_\nu m_\nu^3 \Phi_{\mathbf{k}} |\mathbf{k}| \int_0^\infty \frac{p^2 dp}{(2\pi)^2\hbar^3} \frac{\partial\left[\exp(pc/T_\nu)+1\right]^{-1}}{\partial p} \\
&\quad \int_{-1}^{1} \frac{\cos\theta \cdot d\cos\theta}{p|\mathbf{k}|\cos\theta - m_\nu \boldsymbol{v}_{\nu c}\cdot\mathbf{k}}.
\end{aligned}
\tag{4.16}
$$

The integral over $\cos\theta$ has a singularity and therefore requires regularization. To this end, we need to set the initial conditions upstream in the neutrino flow. Assuming that the gravitational potential of haloes is turned on gradually as $\exp(-\epsilon \boldsymbol{v}_{\nu c}\cdot\mathbf{x})$, which is equivalent to taking $\mathbf{k} \to \mathbf{k} + i\epsilon\boldsymbol{v}_{\nu c}$ in the $\exp(i\mathbf{k}\cdot\mathbf{x})$ Fourier phase factor, we can use Sokhatsky-Weierstrass Identity:

$$
\begin{aligned}
&\frac{1}{p|\mathbf{k}|\cos\theta - m_\nu \boldsymbol{v}_{\nu c}\cdot\mathbf{k} - i m_\nu \epsilon |\boldsymbol{v}_{\nu c}|^2} = \\
&\mathrm{Pr}\frac{1}{p|\mathbf{k}|\cos\theta - m_\nu \boldsymbol{v}_{\nu c}\cdot\mathbf{k}} - i\pi\delta_D\left(p|\mathbf{k}|\cos\theta - m_\nu \boldsymbol{v}_{\nu c}\cdot\mathbf{k}\right).
\end{aligned}
\tag{4.17}
$$

This regularization ensures that neutrino wakes form *behind* the haloes, and is similar to the one used in the derivation of Landau damping in plasmas. e.g [132].

Substituting into the angular integral in Eq. (4.16) yields:

$$\int_{-1}^{1}\frac{\cos\theta\cdot d\cos\theta}{p|\mathbf{k}|\cos\theta-m_\nu\boldsymbol{v}_{\nu c}\cdot\mathbf{k}-im_\nu\epsilon|\boldsymbol{v}_{\nu c}|^2}=$$
$$\frac{2}{p|\mathbf{k}|}+\frac{m_\nu\boldsymbol{v}_{\nu c}\cdot\mathbf{k}}{(p|\mathbf{k}|)^2}\log\left|\frac{p|\mathbf{k}|-m_\nu\boldsymbol{v}_{\nu c}\cdot\mathbf{k}}{p|\mathbf{k}|+m_\nu\boldsymbol{v}_{\nu c}\cdot\mathbf{k}}\right|-$$
$$\frac{i\pi m_\nu\boldsymbol{v}_{\nu c}\cdot\mathbf{k}}{(p|\mathbf{k}|)^2}\Theta\left(p|\mathbf{k}|-m_\nu|\boldsymbol{v}_{\nu c}\cdot\mathbf{k}|\right). \tag{4.18}$$

The real part of this integral is symmetric under $\boldsymbol{v}_{\nu c}\to-\boldsymbol{v}_{\nu c}$, and thus only the imaginary part contributes to the dynamical "friction" of interest. Substituting into Eq. (4.16), the p^2's cancel, making the integrand a total derivative. Therefore, only the boundary term at $p=m_\nu|\boldsymbol{v}_{\nu c}\cdot\mathbf{k}|/|\mathbf{k}|$ contributes to the integral:

$$\delta\rho_{\nu,\mathbf{k}}|_{\text{dyn.fric.}}=-\frac{N_\nu m_\nu^4\Phi_{\mathbf{k}}}{2\pi\hbar^3}\frac{i\boldsymbol{v}_{\nu c}\cdot\mathbf{k}/|\mathbf{k}|}{\exp[(m_\nu c/T_\nu)(\boldsymbol{v}_{\nu c}\cdot\mathbf{k}/|\mathbf{k}|)]+1}, \tag{4.19}$$

which using Gauss's law $\nabla\cdot\mathbf{g}=-4\pi G\rho$, leads to the gravitational field due to dynamical friction:

$$\begin{aligned}\mathbf{g}_{\nu,\mathbf{k}}|_{\text{dyn.fric.}} &= \frac{2N_\nu G m_\nu^4\Phi_{\mathbf{k}}}{\hbar^3|\mathbf{k}|^3}\frac{(\boldsymbol{v}_{\nu c}\cdot\mathbf{k})\mathbf{k}}{\exp[(m_\nu c/T_\nu)(|\boldsymbol{v}_{\nu c}\cdot\mathbf{k}|/|\mathbf{k}|)]+1}\\ &\simeq \frac{2N_\nu G m_\nu^4\mu(|\boldsymbol{v}_{\nu c}|)\Phi_{\mathbf{k}}(\boldsymbol{v}_{\nu c}\cdot\mathbf{k})\mathbf{k}}{\hbar^3|\mathbf{k}|^3},\end{aligned} \tag{4.20}$$

where $0.7\lesssim\mu<1$ captures the velocity dependence of the exponential term in the denominator of first equation. We will assume $\mu=1$ where necessary in our numerical evaluations.

4.2.3 Halo Model

The halo model provides a realistic description of the nonlinear CDM distribution, which includes modelling the profiles of individual haloes, as well as their clustering. See [40] for a general review of the halo model formalism. As a result, clustered haloes will contribute to each other's wakes.

The dynamical friction force on a halo $\mathbf{F}|_{\rm dyn.fric.}$ is given by:

$$\begin{aligned}
\boldsymbol{v}_{\nu c} \quad \cdot \quad \mathbf{F}|_{\rm dyn.fric.} &= \int d^3x\ \rho_{\rm halo}(\mathbf{x})\ \boldsymbol{v}_{\nu c}\cdot\mathbf{g}_\nu(\mathbf{x})|_{\rm dyn.fric.} \\
&= \frac{\mu(|\boldsymbol{v}_{\nu c}|)N_\nu G m_\nu^4 v_{\nu c}^i v_{\nu c}^j}{\hbar^3}\int\frac{d^3k}{(2\pi)^3}\Phi_k\rho_{{\rm halo},k}\frac{k_ik_j}{k^3} \\
&= \frac{4\pi\mu(|\boldsymbol{v}_{\nu c}|)N_\nu G^2 m_\nu^4 v_{\nu c}^2}{3\hbar^3}\int\frac{d^3k}{(2\pi)^3}\frac{\rho_k\rho_{{\rm halo},k}}{k^3}, \qquad (4.21) \\
& \qquad (4.22)
\end{aligned}$$

where in the last two steps, we used spherical symmetry and Poisson's equation. Using the halo model, this can be written as:

$$\begin{aligned}
\boldsymbol{v}_{\nu c}\cdot\mathbf{F}|_{\rm dyn.fric.} = \frac{4\pi\mu(|\boldsymbol{v}_{\nu c}|)N_\nu G^2 m_\nu^4 v_{\nu c}^2}{3\hbar^3}&\int\frac{d^3k}{(2\pi k)^3} \\
&\left[\rho_{{\rm halo},k}^2(M)+\int dM'\frac{dn}{dM'}b(M)b(M')\right. \\
&\left.P_{\rm CDM}(k)\rho_{{\rm halo},k}(M)\rho_{{\rm halo},k}(M')\right], \qquad (4.23)
\end{aligned}$$

where $P_{\rm CDM}(k)$ is the CDM linear power spectrum. The formula for the acceleration due to dynamical friction is then given as

$$\begin{aligned}
\mathbf{a}|_{\rm dyn.fric.} &= M_{\rm halo}^{-1}\mathbf{F}|_{\rm dyn.fric.} \\
&= \frac{2\upsilon(|\boldsymbol{v}_{\nu c}|)N_\nu G^2 m_\nu^4 \boldsymbol{v}_{\nu c}}{3\pi\hbar^3}\int\frac{dk}{k} \\
&\left[\ M_{\rm halo}u(k|M_{\rm halo})^2 + b(M_{\rm halo})P_{\rm CDM}(k)u(k|M_{\rm halo})\right. \\
&\left.\int dM'\frac{dn}{dM'}b(M')M'u(k|M')\ \right]. \qquad (4.24)
\end{aligned}$$

For the halo model, we use the convention of [40] for the normalised Fourier transform of the halo profile (their eq. 107):

$$u(\mathbf{k}|M) \equiv \frac{\int d^3\mathbf{x}\ \rho_{\rm halo}(\mathbf{x}|M)\exp(-i\mathbf{k}\cdot\mathbf{x})}{\int d^3\mathbf{x}\ \rho_{\rm halo}(\mathbf{x}|M)}, \qquad (4.25)$$

where $b(M)$ and dn/dM are the linear bias and mass function, respectively, estimated using the fitting formula of [161, 162] and the concentration-mass relation of [129]. Our final predictions are not sensitive to the specifics of structure formation parameters such as the form of the density profile, the concentration-mass relation, the linear bias model, the mass function, etc. We will also assume the NFW halo mass profile proposed by [124] that has the form (repeated here for clarity):

$$\rho_{\mathrm{NFW}}(r) = \frac{\rho_s}{(r/r_s)(1+r/r_s)^2}, \tag{4.26}$$

where r_s is a characteristic scale radius (the radius at which the logarithmic slope of the density is -2), and ρ_s is an inner density parameter.

Incorporating the details of the halo model, the change in relative velocity for a dark matter halo in terms of the sum of neutrino mass is given by

$$\begin{aligned}\frac{\Delta v_{\nu c}}{v_{\nu c}} = -\frac{2\mu(\boldsymbol{v}_{\nu c}, \boldsymbol{k}) G^2 M_{\mathrm{halo}} N_\nu m_\nu^4}{3\pi H \hbar^3} \int \frac{dk}{k} \\ \Bigg[u(k|M_{\mathrm{halo}})^2 + \frac{b(M_{\mathrm{halo}}) P_{\mathrm{CDM}}(k) u(k|M_{\mathrm{halo}})}{M_{\mathrm{halo}}} \\ \int dM' \frac{dn}{dM'} b(M') M' u(k|M') \Bigg].\end{aligned} \tag{4.27}$$

The first term in square brackets (the 1-halo term) illustrates the contribution to dynamical friction by the main halo (identical to what we found for a solid sphere, Eq. (4.11), for $\mu = 1$) while the second term (the 2-halo term) describes that due to nearby haloes clustered with the main halo. We show the behaviour of the first and second parts of the term in square brackets in Figure 4.4.

The integral over k in Eq. (4.27) is logarithmically divergent since both the 1- and 2-halo terms formally extend to infinity; suitable limits in k must therefore be chosen. In order to set limits that are physically meaningful, we can multiply both sides of Eq. (4.27) by $v_{\nu c}^2$ and incorporate this relative velocity inside the integral (shown in Figure 4.5). At a given wavenumber k, the contribution to the neutrino-CDM relative velocity is only from larger length scales outside the scale of the halo. We also introduce the sum of the different neutrino species. This form integrates the hierarchy of the neutrinos into our calculations and, relaxes the assumption of the degenerate neutrino species. Thus, the equation for

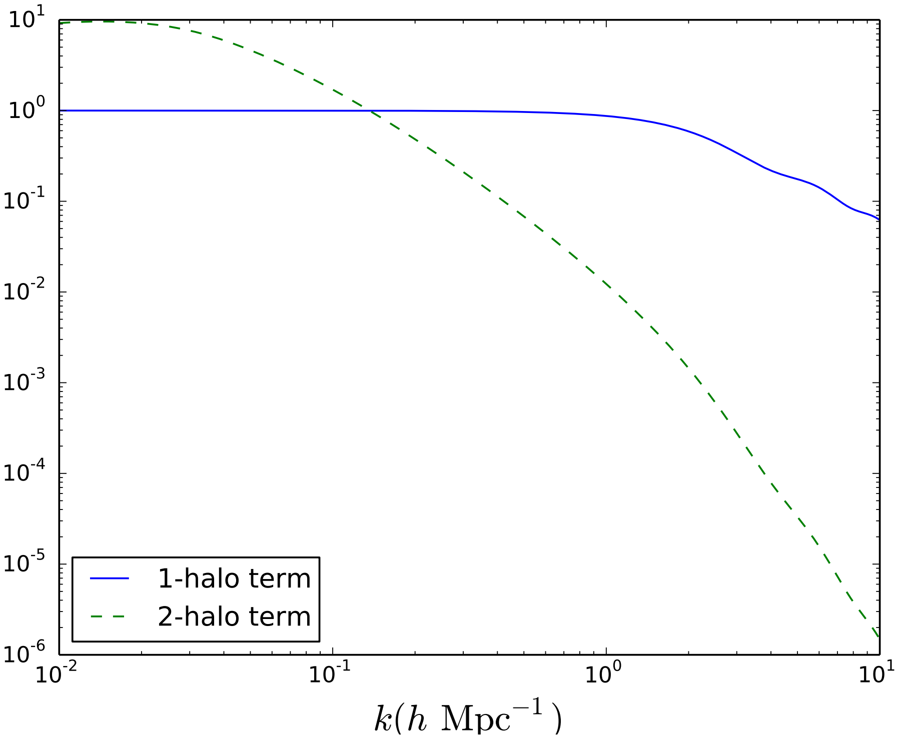

Figure 4.4: The 1-halo and 2-halo terms in square brackets in Eq. (4.27), as a function of k, for $M_{\mathrm{halo}} = 10^{15}h^{-1}M_{\odot}$ and a concentration of 4.

$\Delta v_{\nu c}$ becomes

$$\langle v_{\nu c}\Delta v_{\nu c}\rangle \simeq -\frac{2\mu(\boldsymbol{v}_{\nu c},\boldsymbol{k})G^2M_{\rm halo}}{3\pi H\hbar^3}\sum_{i=1}^{3}m_i^4\int\frac{dk}{k}\langle[v'_{ic}(<k)]^2\rangle$$
$$\left[u(k|M_{\rm halo})^2+\frac{b(M_{\rm halo})P_{\rm CDM}(k)u(k|M_{\rm halo})}{M_{\rm halo}}\right.$$
$$\left.\int dM'\frac{dn}{dM'}b(M')M'u(k|M')\right], \tag{4.28}$$

where

$$\langle[v'_{ic}(<k)]^2\rangle = a^2\int_0^k\frac{dk'}{k'}\Delta^2_{vic}(k')\widetilde{W}^2(k'R), \tag{4.29}$$

and i is for the different neutrino species and $v_{\nu c}$ is the relative velocity from all scales and from all neutrino species.

Recall that the relative velocity between the neutrino and dark matter decreases with scale and goes to zero on very large scales (Figure 4.3). On the other hand, the effects of nonlinearities are expected to be more significant on smaller scales. Therefore, for concreteness, we choose a mid-point of $16h^{-1}$Mpc to filter relative neutrino-CDM velocity field $v_{\nu c}$.

A good fit (for a single neutrino) for the drift velocity $\Delta v_{\nu c}$ and displacement Δx ($\simeq \frac{1}{2}\Delta v_{\nu c}\times t$) over a Hubble time in terms of the neutrino mass m_ν and the halo mass M_h is given by

$$\Delta v_{\nu c} \simeq \frac{\langle v_{\nu c}\Delta v_{\nu c}\rangle}{\langle v^2_{\nu c}\rangle}v_{\nu c} \tag{4.30}$$
$$\simeq (0.2\ \text{km/s})\left[b(M_h)+\left(\frac{M_h}{1.3\times10^{14}h^{-1}M_\odot}\right)^{0.85}\right]$$
$$\left(\frac{m_\nu}{0.1\ \text{eV}}\right)^{2.9}\left(\frac{v_{\nu c,16}}{193\ \text{kms}^{-1}}\right), \tag{4.31}$$
$$\Delta x \simeq (1.5\ \text{kpc})\left[b(M_h)+\left(\frac{M_h}{1.3\times10^{14}h^{-1}M_\odot}\right)^{0.85}\right]$$
$$\left(\frac{m_\nu}{0.1\ \text{eV}}\right)^{2.9}\left(\frac{v_{\nu c,16}}{193\ \text{kms}^{-1}}\right), \tag{4.32}$$

where $v_{\nu c,16}$ is the relative velocity of neutrinos and CDM, averaged over a sphere of radius $16h^{-1}$Mpc, centered around the halo. The explicit dependence of the displacement,

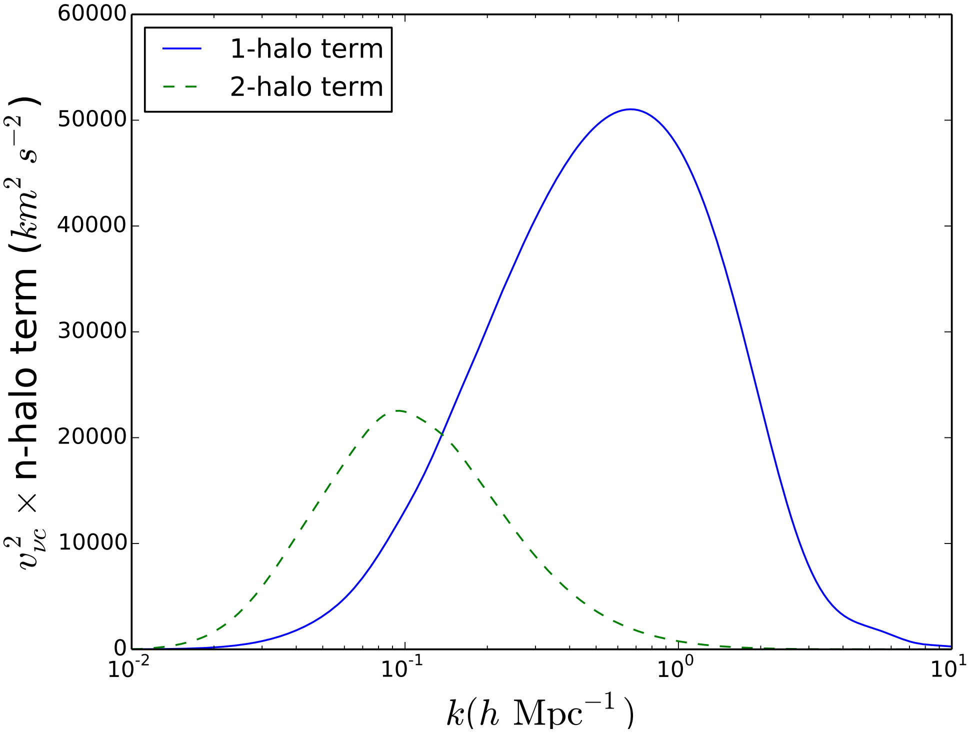

Figure 4.5: The 1-halo and 2-halo terms of the term in square brackets including $[v'_{\nu c}(< k)]^2$ as in Eq. (4.28), for $M_{\rm halo} = 10^{15} h^{-1} M_\odot$ and a $0.2\,\mathrm{eV}$ neutrino.

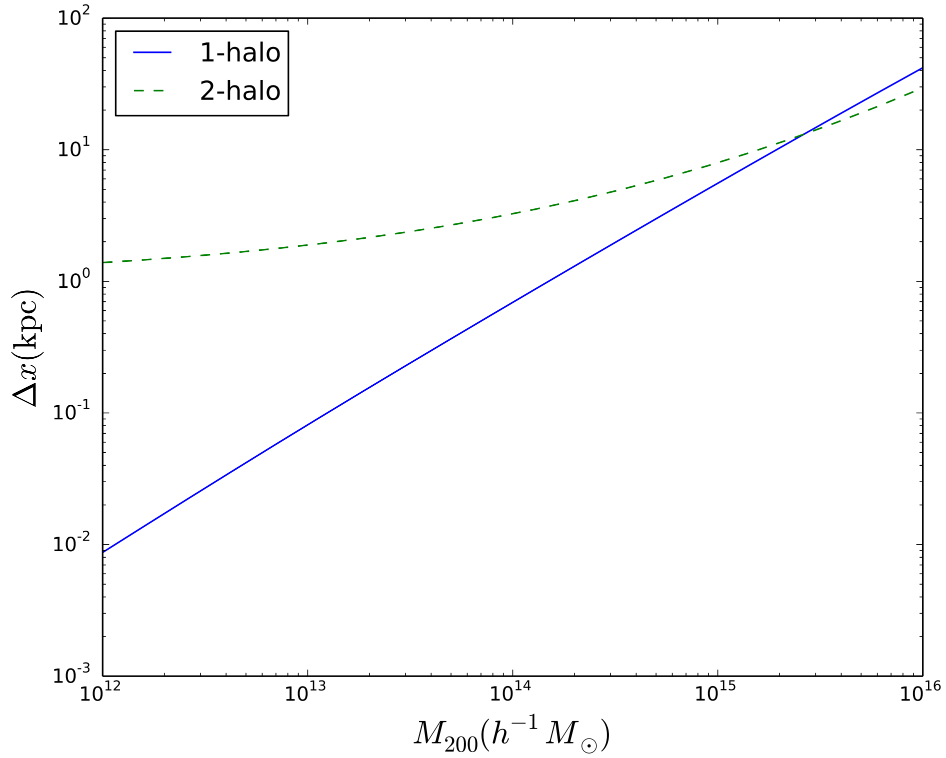

Figure 4.6: The 1-halo and 2-halo contribution to the displacement due to dynamical friction for a 0.1 eV neutrino. It is evident that the 2-halo term dominates for all masses less than $\sim 10^{15}h^{-1}M_\odot$ where the 1-halo term starts dominating.

Δx on the 1-halo and 2-halo terms as a function of mass is shown in Figure 4.6. Figure 4.7 shows a comparison between Δx and the best fit in Eq. (4.32).

4.3 Predicted signal-to-noise for nominal surveys

In this section, we predict the observational prospects for the detection of neutrino dynamical friction in galaxy surveys. One may be tempted to interpret Eq. (4.32) as a relative displacement/velocity of haloes of different mass due the drag by the neutrino wind. However, this is only correct given the assumption that the haloes are not in the

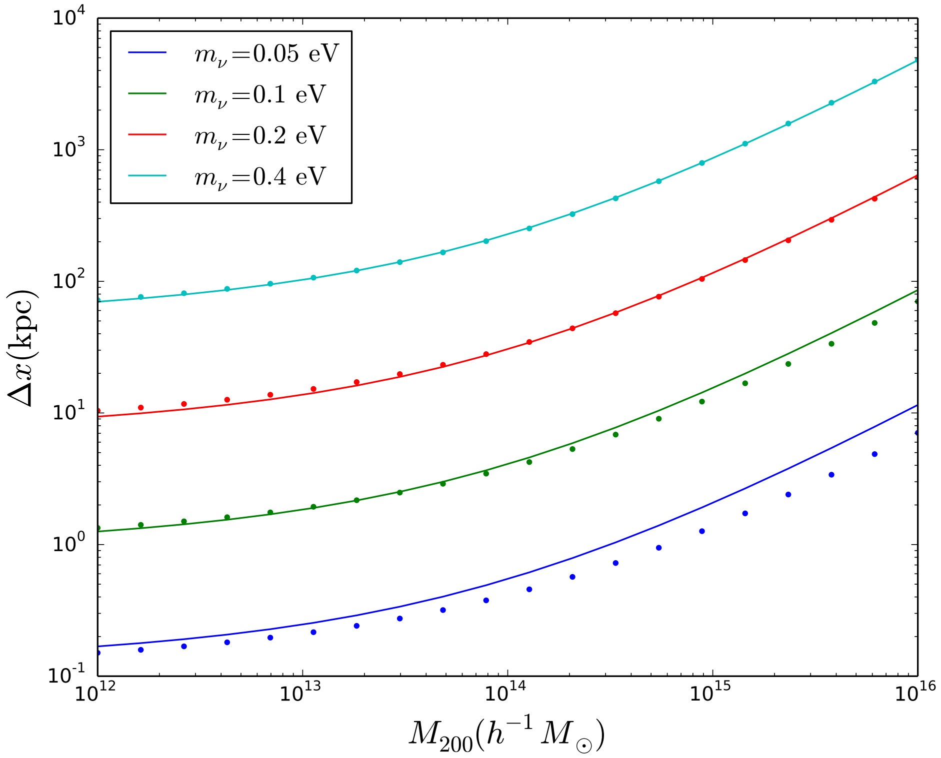

Figure 4.7: A plot comparing the fitting function in Eq. (4.32) with the calculated values for different neutrino masses. The dots are the calculated values while the line is the fitting function.

same neighbourhood and thus have their individual wakes. To make the theoretical predictions in Eq. (4.32), we have averaged over all the haloes distributed around a given halo. In practice, this would lead to an insignificant signal in cross correlating two haloes in the same neighbourhood. The reason for this infinitesimal signal is that they share the same large scale neutrino wake (depicted in Figure 4.8), and thus only experience a small fraction of $\Delta v_{\nu c}$. To achieve an acceptable signal-to-noise estimate, we shall focus on the effect on the large scale distribution of haloes due the gravity of the neutrino wake.

Recall that the effect of dynamical friction on the gravitational field of the halo is given by Eq. (4.20), which is repeated here for convenience,

$$\mathbf{g}_{\nu,\mathbf{k}}\big|_{\text{dyn.fric.}} \;\simeq\; \frac{2Gm_\nu^4\mu(|\boldsymbol{v}_{\nu c}|)\Phi_{\mathbf{k}}(\boldsymbol{v}_{\nu c}\cdot\mathbf{k})\mathbf{k}}{\hbar^3|\mathbf{k}|^3}.$$

This extra effect modifies the total density of gravitating matter in Fourier space, including the neutrino hierarchy, as

$$\begin{aligned}\delta_{m,k} \;&\rightarrow\; \delta_{m,k}\left(1+i\frac{2a^2G\sum_{i=1}^{3}m_i^4\mu\mathbf{v}_{ic}(z)\cdot\mathbf{k}}{\hbar^3|\mathbf{k}|^{\mathbf{3}}}\right),\\ &=\; \delta_{m,k}\left(1+i\phi_{\mathbf{k}}\right), \end{aligned} \tag{4.33}$$

where

$$\phi_{\mathbf{k}} \equiv \frac{2a^2G\sum_{i=1}^{3}m_i^4\mu\mathbf{v}_{ic}(z)\cdot\mathbf{k}}{\hbar^3|\mathbf{k}|^{\mathbf{3}}} \tag{4.34}$$

Thus, the density is modified by an extra time-dependent phase that manifests through the time dependence of the ν-CDM relative velocity. We aim to measure this consequence of dynamical friction due to neutrinos. To this end, we cross-correlate the densities of two tracers (possibly galaxies with different biases) in redshift space. The signal appears as an imaginary term in the redshift-space cross correlation spectrum (see Appendix A.1 for more details). The signal-to-noise for such a measurement is proportional to the difference in bias for the two populations, $(b_l - b_f)$, the effective volume of the survey V_{eff} and the time derivative of the phase term in Eq. (4.34). Let us make some simple theoretical predictions for signal-to-noise for a generic redshift survey. For a given survey with two tracers that have differing bias such as "luminous galaxies" (l) and "faint galaxies" (f), the signal to noise for the imaginary part of the galaxy-cluster redshift-space power spectrum due to the neutrino dynamical friction of the haloes can be calculated to be (see Appendix A.1 for further details):

$$\left(\frac{S}{N}\right)^2_{RSD} = \frac{2V_{\text{eff}}}{(2\pi)^2}\int^{k_{\max}} dk k^2 P_k^2 \Delta b^2 \frac{\langle|\dot{\phi}_{\mathbf{k}}^2|\rangle}{5H^2}|\det C|^{-1}, \tag{4.35}$$

where Δb is the relative linear bias between the two tracers (we include only the linear bias and consider the nonlinear bias a part of the nonlinearities in structure formation under Section 4.4), P_k is the power spectrum of matter fluctuations and V_{eff} is the effective survey volume[4]. We see that the S/N increases with the square root of the survey volume and is larger for tracers with considerable relative bias.

---

[4] For the integral, we have assumed $k_{\max} = 1h^{-1}\text{Mpc}$.

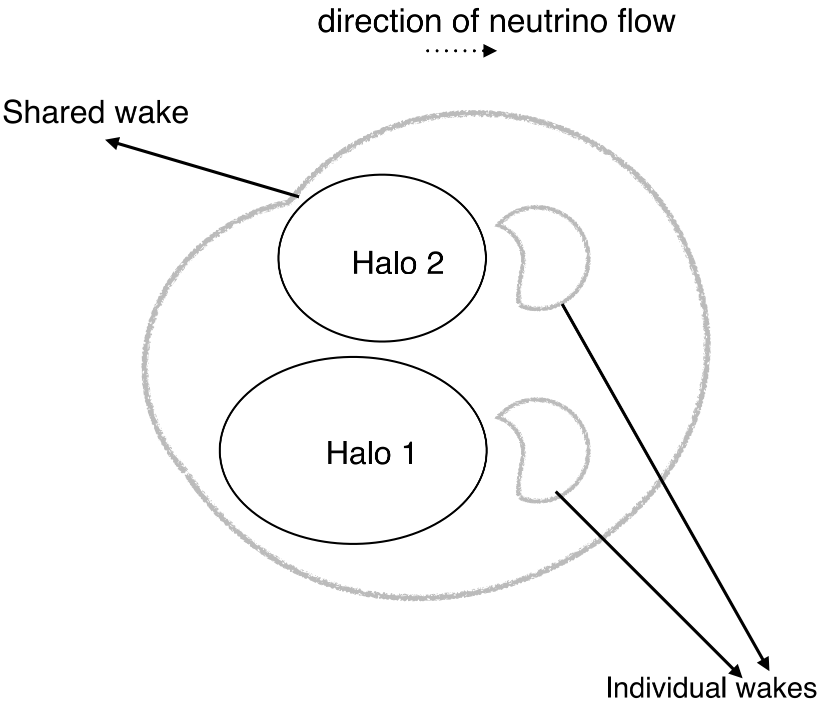

Figure 4.8: A sketch of the effect of shared wakes on the displacement of two haloes.

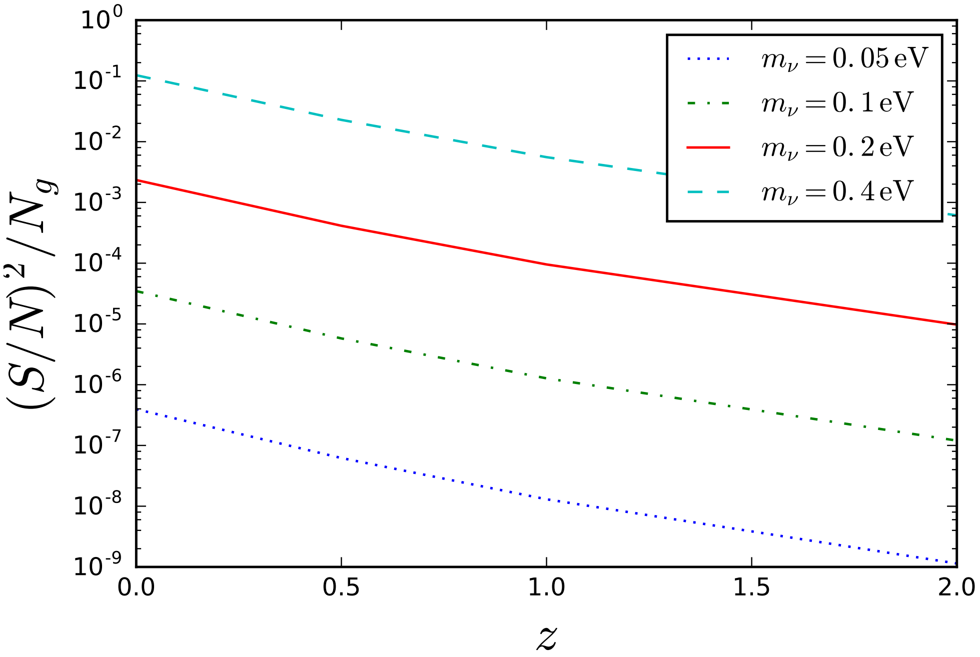

Figure 4.9: The signal-to-noise squared per galaxy as a function of redshift for various neutrino masses. This signal is estimated with a number density $n_l \sim n_f = 0.02\,h^3\mathrm{Mpc}^{-3}$.

Figure 4.9 shows our projection for $(S/N)^2$ per galaxy for the detection of the imaginary part in the redshift-space cross-power spectrum of two tracers (in a nominal survey) with a relative bias $\Delta b \sim 1$ (a typical relative bias between luminous and faint galaxies e.g. [152]), as a function of redshift. These estimates are made over a filtering comoving radius of 16 h^{-1}Mpc. The $(S/N)^2$ per galaxy decreases as the redshift increases due to the steep drop in $\dot{\phi}_{\mathrm{k}}$. For a single neutrino of mass 0.07 eV, a survey with about 2 million galaxies at $z \lesssim 0.5$ can achieve a 2-3σ detection. This may be already achievable by the SDSS main sample [1] or BOSS redshift surveys [9], and will be improved by a factor of 3, in the upcoming DESI survey [103]. Signals from higher neutrino masses due to dynamical friction effects from the neutrino distribution are significantly easier to extract, with $(S/N)^2 \propto m_\nu^6$. For a generic redshift survey, we project that

$$N_g \gtrsim 1.7 \times 10^7 \left(\frac{m_\nu}{0.05 \text{ eV}}\right)^{-6} \frac{28.5^z}{(N_\nu \Delta b)^2} \tag{4.36}$$

galaxies can lead to $> 3\sigma$ detection of the neutrino drag

For constraints on the sum of neutrino masses, M_ν, one will have to sum over the signal from the various contributing species. Figure 4.10 shows these estimates as a function of the minimum neutrino mass (which can be easily related to the sum of neutrino masses, M_ν) for the normal and inverted neutrino hierarchies. Even though we have assumed the number density of the luminous and faint galaxies to be $\sim 0.02\,h^3\mathrm{Mpc}^{-3}$, Figure 4.11 confirms that the signal-to-noise squared per galaxy is insensitive of the number density of galaxies. Thus, the total signal-to-noise squared is proportional to the number of galaxies N_g, Δb^2, and m_ν^6.

An alternative measurement of the dynamical friction effect from neutrinos comes from a direct measurement of the velocities of galaxies, e.g., using the kinematic Sunyaev-Zel'dovich (kSZ) effect e.g. [99, 148, 46]. In this case, the $(S/N)^2$ is given as

$$\left(\frac{S}{N}\right)^2_{\mathrm{kSZ}} = \sum_{N_g} \frac{\Delta v_{\nu c}^2}{\sigma_v^2}, \tag{4.37}$$

with $\Delta v_{\nu c}$ given by Eq. (4.32) and $\sigma_v \sim 1500\,\mathrm{km/s}$. is the velocity error per galaxy, expected from the future CMB S4 kSZ measurements e.g [156]. For a 0.1 eV neutrino and a halo of mass $M_h \sim 10^{13} h^{-1} M_\odot$., in future spectroscopic surveys such as DESI, EUCLID and SPHEREX (spectro), with $\lesssim 10^8$ galaxies, we only get $S/N \lesssim 1$. Therefore, the next generation of kSZ surveys will not be an efficient probe of neutrino dynamical friction.

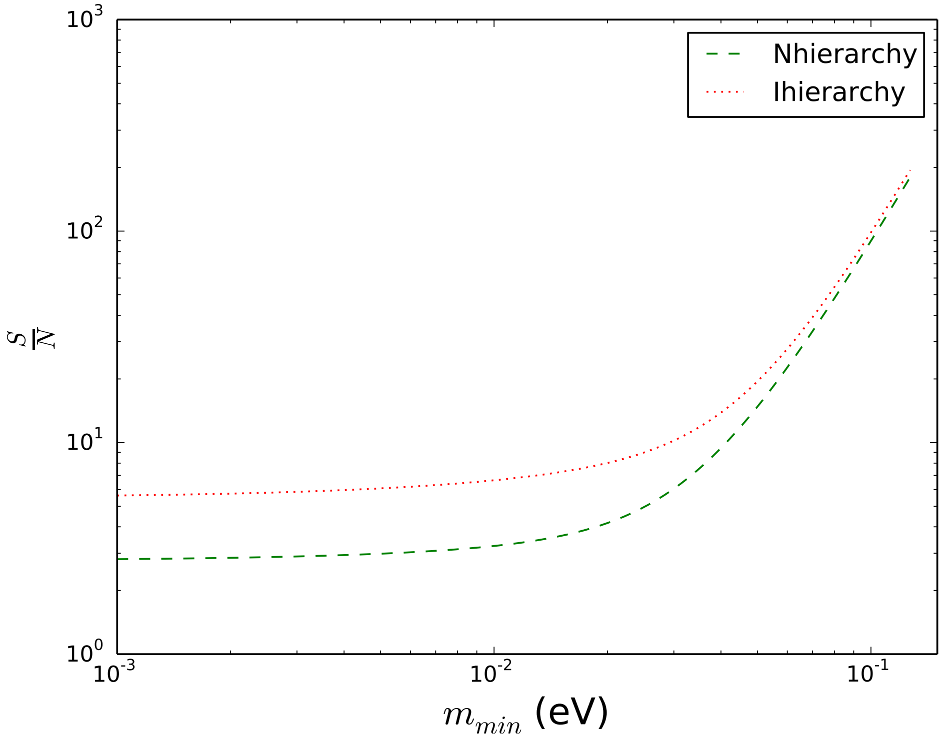

Figure 4.10: S/N for the detection of the imaginary part of the redshift-space cross power spectrum of two tracers due to the dynamical friction effect of massive neutrinos. The dashed and dotted lines represents the S/N for the sum of the neutrino masses assuming the normal and inverted hierarchies respectively. Both plots are for a theoretical survey assuming a volume of $V_{\rm eff} = 1h^{-3}{\rm Gpc}^3$, $\Delta b = 1$ and $n_l \sim n_f = 0.02\ h^3{\rm Mpc}^{-3}$.

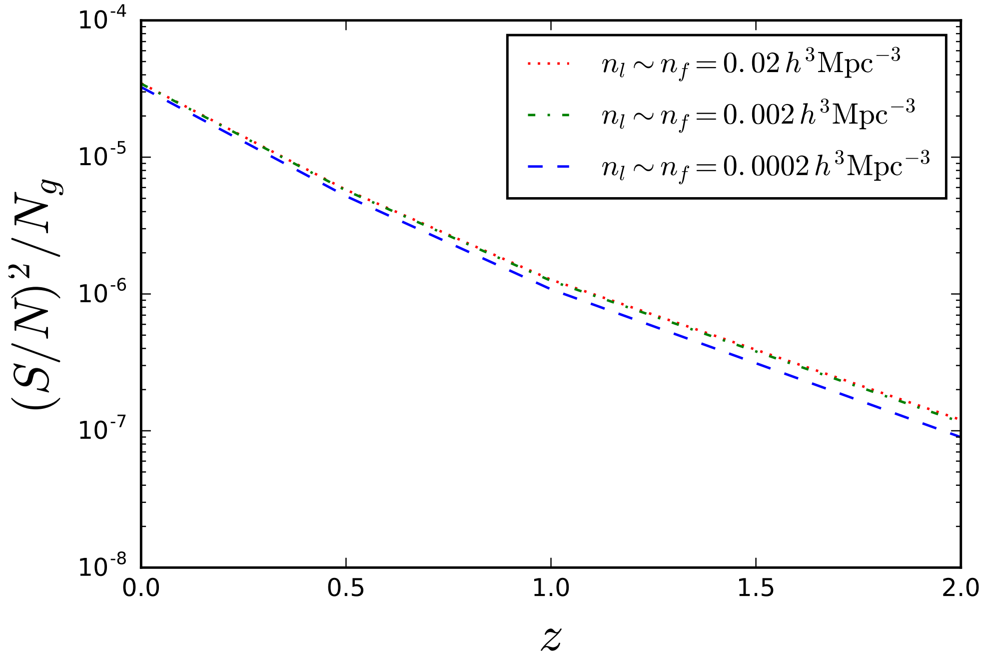

Figure 4.11: The signal-to-noise squared per galaxy as a function of redshift for various number densities, n_l and n_f, expected from the SPHEREX all sky survey [50]. This signal is estimated for a $0.1\,\mathrm{eV}$ neutrino.

4.4 Discussion and Conclusion

We have investigated the prospects for detecting a novel signal from the cross-correlation of different galaxy populations in redshift space expected in the presence of neutrinos. This is due to the dynamical friction drag experienced by dark matter haloes that move in the primordial neutrino sea. Even though the neutrinos and dark matter cannot be observed, these effects make imprints on the galaxies and should be detectable in future surveys. With current surveys, a high ($\gtrsim 10$) S/N is predicted for $M_\nu \sim 0.2\,\mathrm{eV}$, which are marginally allowed by a combination of galaxy surveys and CMB. Given the current limits on the neutrino mass, future generations of high-density redshift surveys such as DESI will be able to detect smaller mass neutrinos or sum of masses $M_\nu < 0.1\,\mathrm{eV}$.

We should note that gravitational redshift can also introduce an imaginary part to the redshift space cross-power spectrum [118]. However, the signal from this effect is smaller than that from the effect of dynamical friction by neutrinos (for a 0.1 eV neutrino) and has a different scale dependence ($\propto k^{-1}$ vs the scale-dependent neutrino signal that peaks at $k \sim 0.01$ Mpc/h).

Other effects of neutrinos on large-scale structure have been discussed by [87]. Their study serves as a method for distinguishing the mass splitting of the neutrinos given a measured constraint on the sum of neutrino masses M_ν. The authors consider the effect of different neutrino masses on the power spectrum on different scales – power suppression on small scales and the change of the matter-radiation equality scale on large scales. They also claim that this method may be used to distinguish the mass splitting of neutrinos given a precise measurement of the matter power spectrum which constrains the sum of neutrino mass. These effects become measurable on large linear scales and do not suffer from nonlinearities and systematic effects. Thus, given a measured constraint on the sum of neutrino masses, this method gives another independent confirmation/test of the mass splitting seen in neutrino oscillation experiments. Yet another impact of neutrinos on large-scale structure was studied by [105], who proposes a method in which neutrino mass may be constrained by the measurement of the scale-dependent bias and the linear growth parameter in upcoming large surveys. Notably, similar to our proposal, this measurement is not limited by cosmic variance.

We next discuss some of the major systematics which may affect our predictions for the signal.

4.4.1 Galaxy and bias

Our estimates for the S/N are based on the number density of galaxies in a survey. Using galaxies requires a good estimate of the galaxy bias. Details and precision in defining the galaxy bias with respect to the total matter in the presence of neutrinos or to the cold dark matter alone [37] are required in constraining the mass of neutrinos through the suppression of power on small scales. However, we expect the exact definition of bias to be less important in extracting the dynamical friction effect, given the large scale coherence of neutrino wind. f The extra scale dependence of the halo bias which may be due to nonlinearities and the free streaming scale of the neutrino is an extra observable proposed by [105]. However, these affect the magnitude, not the phase, of the Fourier amplitudes at percent level, and thus should not bias our projections for neutrino drag.

4.4.2 Nonlinearities in structure formation

The impact of nonlinearities on the CDM-neutrino relative velocity was investigated by [85] in a number of $\nu\Lambda$CDM simulations. The authors were interested in the effectiveness of the simple linear theory approximation given the nonlinear complexities of structure formation. Their measurements show that the relative velocity power spectra predicted from linear theory are higher than that in simulations, but are still within 30% of each other for the empirically allowed neutrino masses. Reconstructing the relative velocity power spectra using the halo density field and the dark matter density field, the authors show that they are correlated with the simulations for scales $k \lesssim 1h/\mathrm{Mpc}$ and also have the right direction of the relative velocity with a mass-dependent correlation coefficient. The magnitude of the reconstruction may be corrected for nonlinearities by the ratio of the nonlinear to linear CDM power spectra. This reconstruction procedure may be implemented in practice to estimate the full neutrino-CDM relative velocity power spectrum.

A more serious issue is whether nonlinear effects in standard nonlinear structure formation can mimic the effect of dynamical friction by neutrinos. After all, the modulation of galaxy (cross-)power spectrum, or relative velocity, by reconstructed $v_{\nu c}$ can be interpreted as a particular contribution to the galaxy bispectrum, which might be partially degenerate with the (much larger) nonlinear halo bispectrum. While Appendix A.2 provides a first look at the magnitude of this degeneracy, a more complete study of this degeneracy in $\nu\Lambda$CDM simulations is planned for the future. Indeed, our preliminary analysis suggests that nonlinear effects are not degenerate with, and only have a marginal impact on our predictions.

4.4.3 Prospects for detection

In practice, measuring the mass of neutrinos from the dynamical friction effect will be quite challenging, and requires a good knowledge and control of standard nonlinear structure formation, neutrino effects, and halo bias. Our S/N estimates have only included the statistical error, and control of systematic uncertainties will only come from a careful study of simulated haloes. Nevertheless, our statistical projection of $S/N \gtrsim 3$ for future surveys (see Eq. 4.36 or Figure 4.9) provides an incentive for further theoretical study and improvement. The dynamical friction effect, described here, may be a powerful complement to the various ways in which neutrinos will be probed over the next decade.

Chapter 5

Conclusion

Given the non – detection of dark matter yet, this thesis has investigated an internal property of dark matter haloes – the concentration of dark matter haloes, which is a characteristic related to the formation epoch of a halo and also plays a vital role in the indirect detection of dark matter (detection of dark matter through the products of its annihilation such as gamma rays, neutrinos, electrons or positrons), using a non-traditional method – a mathematical framework based on two major assumptions – the conservation of the energy of a halo and the inclusion of the ellipsoidal collapse. We then apply this model and another related model of dark matter halo concentration to pinpoint more interesting targets that will probably lead to the end of this hunt for the bulk matter content with enough time of exposure. It is important to note that our estimates have been based on some assumptions about the nature of this particle. Given that the Fermi Gamma ray space telescope has been searching for signs for gamma rays produced from dark matter annihilation, it will be interesting to focus this search to more interesting targets. In which case a null detection may mean constraining the particle property of dark matter such as its mass or cross section area. Like the long-awaited detection of gravitational waves, the hunt for dark matter is possibly nearing the Eureka-moment phase.

Towards the end of the thesis, we digress from the internal properties of dark matter haloes to focus on the large-scale effect haloes may imprint by gravitationally interacting with neutrinos in cosmology; therefore making a prediction of the dynamical friction effect that haloes may feel due the abundant primordial neutrinos streaming in the universe. Although this effect is a theoretical prediction, it can be investigated in a simulation or a galaxy survey with the right properties to make it a detection. This thesis did not cover this interesting investigation but is an avenue for future work related to neutrinos. In any case, cosmology is at a very interesting phase right now.

References

[1] K. N. Abazajian, J. K. Adelman-McCarthy, M. A. Agüeros, S. S. Allam, C. Allende Prieto, D. An, K. S. J. Anderson, S. F. Anderson, J. Annis, N. A. Bahcall, and et al. The Seventh Data Release of the Sloan Digital Sky Survey. *The Astrophysical Journal Supplement Series*, 182:543–558, June 2009.

[2] K. N. Abazajian and M. Kaplinghat. Detection of a gamma-ray source in the Galactic Center consistent with extended emission from dark matter annihilation and concentrated astrophysical emission. *Physical Review D*, 86(8):083511, October 2012.

[3] A. A. Abdo, et al. Fermi Large Area Telescope observations of Local Group galaxies: detection of M 31 and search for M 33. *Astronomy and Astrophysics*, 523:L2, November 2010.

[4] M. Ackermann, M. Ajello, A. Allafort, L. Baldini, J. Ballet, G. Barbiellini, D. Bastieri, K. Bechtol, R. Bellazzini, R. D. Blandford, E. D. Bloom, E. Bonamente, A. W. Borgland, A. Bouvier, T. J. Brandt, J. Bregeon, M. Brigida, P. Bruel, R. Buehler, S. Buson, G. A. Caliandro, R. A. Cameron, P. A. Caraveo, S. Carrigan, J. M. Casandjian, C. Cecchi, E. Charles, A. Chekhtman, C. C. Cheung, J. Chiang, S. Ciprini, R. Claus, J. Cohen-Tanugi, L. R. Cominsky, J. Conrad, A. de Angelis, F. de Palma, E. d. C. e. Silva, P. S. Drell, A. Drlica-Wagner, R. Dubois, D. Dumora, Y. Edmonds, C. Farnier, C. Favuzzi, S. J. Fegan, M. Frailis, Y. Fukazawa, P. Fusco, F. Gargano, D. Gasparrini, N. Gehrels, S. Germani, N. Giglietto, F. Giordano, T. Glanzman, G. Godfrey, I. A. Grenier, S. Guiriec, M. Gustafsson, A. K. Harding, M. Hayashida, D. Horan, R. E. Hughes, T. E. Jeltema, G. Jóhannesson, A. S. Johnson, W. N. Johnson, T. Kamae, H. Katagiri, J. Kataoka, J. Knödlseder, M. Kuss, J. Lande, L. Latronico, S.-H. Lee, M. Llena Garde, F. Longo, F. Loparco, M. N. Lovellette, P. Lubrano, G. M. Madejski, A. Makeev, M. N. Mazziotta, P. F. Michelson, W. Mitthumsiri, T. Mizuno, A. A. Moiseev, C. Monte, M. E. Monzani, A. Morselli, I. V. Moskalenko, S. Murgia, P. L. Nolan, J. P. Norris, E. Nuss, M. Ohno, T. Ohsugi,

N. Omodei, E. Orlando, J. F. Ormes, J. H. Panetta, M. Pepe, M. Pesce-Rollins, F. Piron, T. A. Porter, S. Profumo, S. Rainò, M. Razzano, T. Reposeur, S. Ritz, A. Y. Rodriguez, M. Roth, H. F.-W. Sadrozinski, A. Sander, J. D. Scargle, C. Sgrò, E. J. Siskind, P. D. Smith, G. Spandre, P. Spinelli, J.-L. Starck, M. S. Strickman, D. J. Suson, H. Takahashi, T. Tanaka, J. B. Thayer, J. G. Thayer, L. Tibaldo, D. F. Torres, G. Tosti, T. L. Usher, V. Vasileiou, V. Vitale, A. P. Waite, P. Wang, B. L. Winer, K. S. Wood, Z. Yang, T. Ylinen, M. Ziegler, and Fermi LAT Collaboration. Constraints on dark matter annihilation in clusters of galaxies with the Fermi large area telescope. *JCAP*, 5:25, May 2010.

[5] M. Ackermann, M. Ajello, A. Allafort, L. Baldini, J. Ballet, D. Bastieri, K. Bechtol, R. Bellazzini, B. Berenji, E. D. Bloom, E. Bonamente, A. W. Borgland, A. Bouvier, J. Bregeon, M. Brigida, P. Bruel, R. Buehler, S. Buson, G. A. Caliandro, R. A. Cameron, P. A. Caraveo, J. M. Casandjian, C. Cecchi, E. Charles, A. Chekhtman, C. C. Cheung, J. Chiang, A. N. Cillis, S. Ciprini, R. Claus, J. Cohen-Tanugi, J. Conrad, S. Cutini, F. de Palma, C. D. Dermer, S. W. Digel, E. d. C. e. Silva, P. S. Drell, A. Drlica-Wagner, C. Favuzzi, S. J. Fegan, P. Fortin, Y. Fukazawa, S. Funk, P. Fusco, F. Gargano, D. Gasparrini, S. Germani, N. Giglietto, F. Giordano, T. Glanzman, G. Godfrey, I. A. Grenier, S. Guiriec, M. Gustafsson, D. Hadasch, M. Hayashida, E. Hays, R. E. Hughes, G. Jóhannesson, A. S. Johnson, T. Kamae, H. Katagiri, J. Kataoka, J. Knödlseder, M. Kuss, J. Lande, F. Longo, F. Loparco, B. Lott, M. N. Lovellette, P. Lubrano, G. M. Madejski, P. Martin, M. N. Mazziotta, J. E. McEnery, P. F. Michelson, T. Mizuno, C. Monte, M. E. Monzani, A. Morselli, I. V. Moskalenko, S. Murgia, S. Nishino, J. P. Norris, E. Nuss, M. Ohno, T. Ohsugi, A. Okumura, N. Omodei, E. Orlando, M. Ozaki, D. Parent, M. Persic, M. Pesce-Rollins, V. Petrosian, M. Pierbattista, F. Piron, G. Pivato, T. A. Porter, S. Rainò, R. Rando, M. Razzano, A. Reimer, O. Reimer, S. Ritz, M. Roth, C. Sbarra, C. Sgrò, E. J. Siskind, G. Spandre, P. Spinelli, Ł. Stawarz, A. W. Strong, H. Takahashi, T. Tanaka, J. B. Thayer, L. Tibaldo, M. Tinivella, D. F. Torres, G. Tosti, E. Troja, Y. Uchiyama, J. Vandenbroucke, G. Vianello, V. Vitale, A. P. Waite, M. Wood, and Z. Yang. GeV Observations of Star-forming Galaxies with the Fermi Large Area Telescope. *The Astrophysical Journal*, 755:164, August 2012.

[6] M. Ackermann, et al. The Spectrum of Isotropic Diffuse Gamma-Ray Emission between 100 MeV and 820 GeV. *The Astrophysical Journal*, 799:86, January 2015.

[7] M. Ackermann, et al. Observations of M31 and M33 with the Fermi Large Area Telescope: A Galactic Center Excess in Andromeda? *The Astrophysical Journal*, 836:208, February 2017.

[8] N. Afshordi and R. Cen. Mass-Temperature Relation of Galaxy Clusters: A Theoretical Study. *The Astrophysical Journal*, 564:669–682, January 2002.

[9] C. P. Ahn, R. Alexandroff, C. Allende Prieto, F. Anders, S. F. Anderson, T. Anderton, B. H. Andrews, É. Aubourg, S. Bailey, F. A. Bastien, and et al. The Tenth Data Release of the Sloan Digital Sky Survey: First Spectroscopic Data from the SDSS-III Apache Point Observatory Galactic Evolution Experiment. *The Astrophysical Journal Supplement Series*, 211:17, April 2014.

[10] M. Ajello, D. Gasparrini, M. Sánchez-Conde, G. Zaharijas, M. Gustafsson, J. Cohen-Tanugi, C. D. Dermer, Y. Inoue, D. Hartmann, M. Ackermann, K. Bechtol, A. Franckowiak, A. Reimer, R. W. Romani, and A. W. Strong. The Origin of the Extragalactic Gamma-Ray Background and Implications for Dark Matter Annihilation. *The Astrophysical Journal Letters*, 800:L27, February 2015.

[11] C. Alcock, R. A. Allsman, D. R. Alves, T. S. Axelrod, A. C. Becker, D. P. Bennett, K. H. Cook, N. Dalal, A. J. Drake, K. C. Freeman, M. Geha, K. Griest, M. J. Lehner, S. L. Marshall, D. Minniti, C. A. Nelson, B. A. Peterson, P. Popowski, M. R. Pratt, P. J. Quinn, C. W. Stubbs, W. Sutherland, A. B. Tomaney, T. Vandehei, and D. Welch. The MACHO Project: Microlensing Results from 5.7 Years of Large Magellanic Cloud Observations. *The Astrophysical Journal*, 542:281–307, October 2000.

[12] B. Allgood, R. A. Flores, J. R. Primack, A. V. Kravtsov, R. H. Wechsler, A. Faltenbacher, and J. S. Bullock. The shape of dark matter haloes: dependence on mass, redshift, radius and formation. *Monthly Notices of the Royal Astronomical Society*, 367:1781–1796, April 2006.

[13] D. Anderhalden and J. Diemand. Density profiles of CDM microhalos and their implications for annihilation boost factors. *JCAP*, 4:9, April 2013.

[14] S. Ando. Can Dark Matter Annihilation Dominate the Extragalactic Gamma-Ray Background? *Physical Review Letters*, 94(17):171303, May 2005.

[15] P. W. Angel, G. B. Poole, A. D. Ludlow, A. R. Duffy, P. M. Geil, S. J. Mutch, A. Mesinger, and J. S. B. Wyithe. Dark-ages reionization and galaxy formation simulation - II. Spin and concentration parameters for dark matter haloes during the epoch of reionization. *Monthly Notices of the Royal Astronomical Society*, 459:2106–2117, June 2016.

[16] V. Avila-Reese, P. Colín, S. Gottlöber, C. Firmani, and C. Maulbetsch. The Dependence on Environment of Cold Dark Matter Halo Properties. *The Astrophysical Journal*, 634:51–69, November 2005.

[17] Y. M. Bahé, I. G. McCarthy, and L. J. King. Mock weak lensing analysis of simulated galaxy clusters: bias and scatter in mass and concentration. *Monthly Notices of the Royal Astronomical Society*, 421:1073–1088, April 2012.

[18] J. Bailin, C. Power, B. K. Gibson, and M. Steinmetz. How Concentrated Are The Haloes Of Low Surface Brightness Galaxies In The Cold Dark Matter Model? *ArXiv e-prints*, February 2005.

[19] E. A. Baltz, J. E. Taylor, and L. L. Wai. Can Astrophysical Gamma-Ray Sources Mimic Dark Matter Annihilation in Galactic Satellites? *The Astrophysical Journal Letters*, 659:L125–L128, April 2007.

[20] R. Bartels and S. Ando. Boosting the annihilation boost: Tidal effects on dark matter subhalos and consistent luminosity modeling. *Physical Review D*, 92(12):123508, December 2015.

[21] R. A. Battye and A. Moss. Evidence for Massive Neutrinos from Cosmic Microwave Background and Lensing Observations. *Physical Review Letters*, 112(5):051303, February 2014.

[22] K. Bechtol, M. Ahlers, M. Di Mauro, M. Ajello, and J. Vandenbroucke. Evidence against Star-forming Galaxies as the Dominant Source of Icecube Neutrinos. *The Astrophysical Journal*, 836:47, February 2017.

[23] P. S. Behroozi, R. H. Wechsler, and C. Conroy. The Average Star Formation Histories of Galaxies in Dark Matter Halos from z = 0-8. *The Astrophysical Journal*, 770:57, June 2013.

[24] L. Berezhiani and J. Khoury. Theory of dark matter superfluidity. *Physical Review D*, 92(10):103510, November 2015.

[25] Lars Bergström, Joakim Edsjö, and Piero Ullio. Spectral gamma-ray signatures of cosmological dark matter annihilations. *Physical Review Letters*, 87:251301, Nov 2001.

[26] E. Bertschinger. Self-similar secondary infall and accretion in an Einstein-de Sitter universe. *The Astrophysical Journal Supplement Series*, 58:39–65, May 1985.

[27] P. Bett, V. Eke, C. S. Frenk, A. Jenkins, J. Helly, and J. Navarro. The spin and shape of dark matter haloes in the Millennium simulation of a Λ cold dark matter universe. *Monthly Notices of the Royal Astronomical Society*, 376:215–232, March 2007.

[28] F. Beutler, C. Blake, J. Koda, F. A. Marín, H.-J. Seo, A. J. Cuesta, and D. P. Schneider. The BOSS-WiggleZ overlap region - I. Baryon acoustic oscillations. *Monthly Notices of the Royal Astronomical Society*, 455:3230–3248, January 2016.

[29] F. Beutler, S. Saito, J. R. Brownstein, C.-H. Chuang, A. J. Cuesta, W. J. Percival, A. J. Ross, N. P. Ross, D. P. Schneider, L. Samushia, A. G. Sánchez, H.-J. Seo, J. L. Tinker, C. Wagner, and B. A. Weaver. The clustering of galaxies in the SDSS-III Baryon Oscillation Spectroscopic Survey: signs of neutrino mass in current cosmological data sets. *Monthly Notices of the Royal Astronomical Society*, 444:3501–3516, November 2014.

[30] S. Bhattacharya, S. Habib, K. Heitmann, and A. Vikhlinin. Dark Matter Halo Profiles of Massive Clusters: Theory versus Observations. *The Astrophysical Journal*, 766:32, March 2013.

[31] J. Binney and S. Tremaine. *Galactic dynamics*. Princeton, NJ, Princeton University Press, 1987, 747 p., 1987.

[32] J. R. Bond, S. Cole, G. Efstathiou, and N. Kaiser. Excursion set mass functions for hierarchical Gaussian fluctuations. *The Astrophysical Journal*, 379:440–460, October 1991.

[33] J. R. Bond, G. Efstathiou, and J. Silk. Massive neutrinos and the large-scale structure of the universe. *Physical Review Letters*, 45:1980–1984, December 1980.

[34] T. Bridges, K. Gebhardt, R. Sharples, F. R. Faifer, J. C. Forte, M. A. Beasley, S. E. Zepf, D. A. Forbes, D. A. Hanes, and M. Pierce. The globular cluster kinematics and galaxy dark matter content of NGC 4649 (M60). *Monthly Notices of the Royal Astronomical Society*, 373:157–166, November 2006.

[35] J. S. Bullock, T. S. Kolatt, Y. Sigad, R. S. Somerville, A. V. Kravtsov, A. A. Klypin, J. R. Primack, and A. Dekel. Profiles of dark haloes: evolution, scatter and environment. *Monthly Notices of the Royal Astronomical Society*, 321:559–575, March 2001.

[36] Isabella P. Carucci, Martin Sparre, Steen H. Hansen, and Michael Joyce. Particle ejection during mergers of dark matter halos. *Journal of Cosmology and Astroparticle Physics*, 2014(06):057, 2014.

[37] E. Castorina, E. Sefusatti, R. K. Sheth, F. Villaescusa-Navarro, and M. Viel. Cosmology with massive neutrinos II: on the universality of the halo mass function and bias. *JCAP*, 2:049, February 2014.

[38] D. Clowe, M. Bradač, A. H. Gonzalez, M. Markevitch, S. W. Randall, C. Jones, and D. Zaritsky. A Direct Empirical Proof of the Existence of Dark Matter. *The Astrophysical Journal Letters*, 648:L109–L113, September 2006.

[39] J. Conrad. Indirect Detection of WIMP Dark Matter: a compact review. *arXiv e-prints*, November 2014.

[40] A. Cooray and R. Sheth. Halo models of large scale structure. *Physics Report*, 372:1–129, December 2002.

[41] C. A. Correa, J. S. B. Wyithe, J. Schaye, and A. R. Duffy. The accretion history of dark matter haloes - III. A physical model for the concentration-mass relation. *Monthly Notices of the Royal Astronomical Society*, 452:1217–1232, September 2015.

[42] M. M. Crone, A. E. Evrard, and D. O. Richstone. The cosmological dependence of cluster density profiles. *The Astrophysical Journal*, 434:402–416, October 1994.

[43] A. J. Cuesta, V. Niro, and L. Verde. Neutrino mass limits: Robust information from the power spectrum of galaxy surveys. *Physics of the Dark Universe*, 13:77–86, September 2016.

[44] S. Das and R. K. Bhaduri. Dark matter and dark energy from a Bose-Einstein condensate. *Classical and Quantum Gravity*, 32(10):105003, May 2015.

[45] M. Davis, G. Efstathiou, C. S. Frenk, and S. D. M. White. The evolution of large-scale structure in a universe dominated by cold dark matter. *The Astrophysical Journal*, 292:371–394, May 1985.

[46] F. De Bernardis, S. Aiola, E. M. Vavagiakis, N. Battaglia, M. D. Niemack, J. Beall, D. T. Becker, J. R. Bond, E. Calabrese, H. Cho, K. Coughlin, R. Datta, M. Devlin, J. Dunkley, R. Dunner, S. Ferraro, A. Fox, P. A. Gallardo, M. Halpern, N. Hand, M. Hasselfield, S. W. Henderson, J. C. Hill, G. C. Hilton, M. Hilton, A. D. Hincks,

R. Hlozek, J. Hubmayr, K. Huffenberger, J. P. Hughes, K. D. Irwin, B. J. Koopman, A. Kosowsky, D. Li, T. Louis, M. Lungu, M. S. Madhavacheril, L. Maurin, J. McMahon, K. Moodley, S. Naess, F. Nati, L. Newburgh, J. P. Nibarger, L. A. Page, B. Partridge, E. Schaan, B. L. Schmitt, N. Sehgal, J. Sievers, S. M. Simon, D. N. Spergel, S. T. Staggs, J. R. Stevens, R. J. Thornton, A. van Engelen, J. Van Lanen, and E. J. Wollack. Detection of the pairwise kinematic Sunyaev-Zel'dovich effect with BOSS DR11 and the Atacama Cosmology Telescope. *JCAP*, 3:008, March 2017.

[47] W. Dehnen and D. E. McLaughlin. Dynamical insight into dark matter haloes. *Monthly Notices of the Royal Astronomical Society*, 363:1057–1068, November 2005.

[48] A. Del Popolo and M. Gambera. Non radial motions and the shapes and the abundance of clusters of galaxies. *Astronomy and Astrophysics*, 357:809–815, May 2000.

[49] B. Diemer and A. V. Kravtsov. A Universal Model for Halo Concentrations. *The Astrophysical Journal*, 799:108, January 2015.

[50] O. Doré, J. Bock, M. Ashby, P. Capak, A. Cooray, R. de Putter, T. Eifler, N. Flagey, Y. Gong, S. Habib, K. Heitmann, C. Hirata, W.-S. Jeong, R. Katti, P. Korngut, E. Krause, D.-H. Lee, D. Masters, P. Mauskopf, G. Melnick, B. Mennesson, H. Nguyen, K. Öberg, A. Pullen, A. Raccanelli, R. Smith, Y.-S. Song, V. Tolls, S. Unwin, T. Venumadhav, M. Viero, M. Werner, and M. Zemcov. Cosmology with the SPHEREX All-Sky Spectral Survey. *ArXiv e-prints*, December 2014.

[51] A. G. Doroshkevich. The space structure of perturbations and the origin of rotation of galaxies in the theory of fluctuation. *Astrofizika*, 6:581–600, 1970.

[52] A. G. Doroshkevich, R. A. Sunyaev, and I. B. Zeldovich. The formation of galaxies in Friedmannian universes. In M. S. Longair, editor, *Confrontation of Cosmological Theories with Observational Data*, volume 63 of *IAU Symposium*, pages 213–225, 1974.

[53] M. J. Drinkwater, R. J. Jurek, C. Blake, D. Woods, K. A. Pimbblet, K. Glazebrook, R. Sharp, M. B. Pracy, S. Brough, M. Colless, W. J. Couch, S. M. Croom, T. M. Davis, D. Forbes, K. Forster, D. G. Gilbank, M. Gladders, B. Jelliffe, N. Jones, I.-H. Li, B. Madore, D. C. Martin, G. B. Poole, T. Small, E. Wisnioski, T. Wyder, and H. K. C. Yee. The WiggleZ Dark Energy Survey: survey design and first data release. *Monthly Notices of the Royal Astronomical Society*, 401:1429–1452, January 2010.

[54] A. R. Duffy, J. Schaye, S. T. Kay, and C. Dalla Vecchia. Dark matter halo concentrations in the Wilkinson Microwave Anisotropy Probe year 5 cosmology. *Monthly Notices of the Royal Astronomical Society*, 390:L64–L68, October 2008.

[55] A. R. Duffy, J. Schaye, S. T. Kay, C. Dalla Vecchia, R. A. Battye, and C. M. Booth. Impact of baryon physics on dark matter structures: a detailed simulation study of halo density profiles. *Monthly Notices of the Royal Astronomical Society*, 405:2161–2178, July 2010.

[56] A. A. Dutton and A. V. Macciò. Cold dark matter haloes in the Planck era: evolution of structural parameters for Einasto and NFW profiles. *Monthly Notices of the Royal Astronomical Society*, 441:3359–3374, July 2014.

[57] G. Efstathiou, C. S. Frenk, Simon D. M. White, and M. Davis. Gravitational clustering from scale free initial conditions. *Monthly Notices of the Royal Astronomical Society*, 235:715–748, 1988.

[58] J. Einasto. On the Construction of a Composite Model for the Galaxy and on the Determination of the System of Galactic Parameters. *Trudy Astrofizicheskogo Instituta Alma-Ata*, 5:87–100, 1965.

[59] D. J. Eisenstein and W. Hu. Baryonic Features in the Matter Transfer Function. *The Astrophysical Journal*, 496:605–614, March 1998.

[60] V. R. Eke, J. F. Navarro, and M. Steinmetz. The Power Spectrum Dependence of Dark Matter Halo Concentrations. *The Astrophysical Journal*, 554:114–125, June 2001.

[61] J. D. Emberson, T. Kobayashi, and M. A. Alvarez. Evolution of Low Mass Galactic Subhalos and Dependence on Concentration. *The Astrophysical Journal*, 812:9, October 2015.

[62] A. E. Evrard, C. A. Metzler, and J. F. Navarro. Mass Estimates of X-Ray Clusters. *The Astrophysical Journal*, 469:494, October 1996.

[63] J. A. Fillmore and P. Goldreich. Self-similar gravitational collapse in an expanding universe. *The Astrophysical Journal*, 281:1–8, June 1984.

[64] G. L. Fogli, E. Lisi, A. Marrone, D. Montanino, A. Palazzo, and A. M. Rotunno. Global analysis of neutrino masses, mixings, and phases: Entering the era of leptonic CP violation searches. *Physical Review D*, 86(1):013012, July 2012.

[65] L. Gao, J. F. Navarro, S. Cole, C. S. Frenk, S. D. M. White, V. Springel, A. Jenkins, and A. F. Neto. The redshift dependence of the structure of massive Λ cold dark matter haloes. *Monthly Notices of the Royal Astronomical Society*, 387:536–544, June 2008.

[66] L. Gao, S. D. M. White, A. Jenkins, F. Stoehr, and V. Springel. The subhalo populations of ΛCDM dark haloes. *Monthly Notices of the Royal Astronomical Society*, 355:819–834, December 2004.

[67] K. Garrett and G. Dūda. Dark Matter: A Primer. *Advances in Astronomy*, 2011:968283, 2011.

[68] C. Giocoli, M. Meneghetti, S. Ettori, and L. Moscardini. Cosmology in two dimensions: the concentration-mass relation for galaxy clusters. *Monthly Notices of the Royal Astronomical Society*, 426:1558–1573, October 2012.

[69] C. Giocoli, G. Tormen, and R. K. Sheth. Formation times, mass growth histories and concentrations of dark matter haloes. *Monthly Notices of the Royal Astronomical Society*, 422:185–198, May 2012.

[70] O. Y. Gnedin, A. V. Kravtsov, A. A. Klypin, and D. Nagai. Response of Dark Matter Halos to Condensation of Baryons: Cosmological Simulations and Improved Adiabatic Contraction Model. *The Astrophysical Journal*, 616:16–26, November 2004.

[71] M. B. Gralla, K. Sharon, M. D. Gladders, D. P. Marrone, L. F. Barrientos, M. Bayliss, M. Bonamente, E. Bulbul, J. E. Carlstrom, T. Culverhouse, D. G. Gilbank, C. Greer, N. Hasler, D. Hawkins, R. Hennessy, M. Joy, B. Koester, J. Lamb, E. Leitch, A. Miller, T. Mroczkowski, S. Muchovej, M. Oguri, T. Plagge, C. Pryke, and D. Woody. Sunyaev-Zel'dovich Effect Observations of Strong Lensing Galaxy Clusters: Probing the Overconcentration Problem. *The Astrophysical Journal*, 737:74, August 2011.

[72] J. E. Gunn and J. R. Gott, III. On the Infall of Matter Into Clusters of Galaxies and Some Effects on Their Evolution. *The Astrophysical Journal*, 176:1, August 1972.

[73] J. Han, S. Cole, C. S. Frenk, and Y. Jing. A unified model for the spatial and mass distribution of subhaloes. *Monthly Notices of the Royal Astronomical Society*, 457:1208–1223, April 2016.

[74] S. H. Hansen. Might We Eventually Understand the Origin of the Dark Matter Velocity Anisotropy? *The Astrophysical Journal*, 694:1250–1255, April 2009.

[75] S. H. Hansen and B. Moore. A universal density slope Velocity anisotropy relation for relaxed structures. *New Astronomy*, 11:333–338, March 2006.

[76] E. Hayashi, J. F. Navarro, J. E. Taylor, J. Stadel, and T. Quinn. The Structural Evolution of Substructure. *The Astrophysical Journal*, 584:541–558, February 2003.

[77] E. Hayashi and S. D. M. White. Understanding the halo-mass and galaxy-mass cross-correlation functions. *Monthly Notices of the Royal Astronomical Society*, 388:2–14, July 2008.

[78] J. F. Hennawi, N. Dalal, P. Bode, and J. P. Ostriker. Characterizing the Cluster Lens Population. *The Astrophysical Journal*, 654:714–730, January 2007.

[79] Y. Hoffman and J. Shaham. Local density maxima - Progenitors of structure. *The Astrophysical Journal*, 297:16–22, October 1985.

[80] S. Hofmann, D. J. Schwarz, and H. Stöcker. Damping scales of neutralino cold dark matter. *Physical Review D*, 64(8):083507, October 2001.

[81] O. Host and S. H. Hansen. What it takes to measure a fundamental difference between dark matter and baryons: the halo velocity anisotropy. *JCAP*, 6:016, June 2007.

[82] O. Host, S. H. Hansen, R. Piffaretti, A. Morandi, S. Ettori, S. T. Kay, and R. Valdarnini. Measurement of the Dark Matter Velocity Anisotropy in Galaxy Clusters. *The Astrophysical Journal*, 690:358–366, January 2009.

[83] K. M. Huffenberger and U. Seljak. Halo concentration and the dark matter power spectrum. *Monthly Notices of the Royal Astronomical Society*, 340:1199–1204, April 2003.

[84] P. J. Humphrey, D. A. Buote, F. Gastaldello, L. Zappacosta, J. S. Bullock, F. Brighenti, and W. G. Mathews. A Chandra View of Dark Matter in Early-Type Galaxies. *The Astrophysical Journal*, 646:899–918, August 2006.

[85] D. Inman, J. D. Emberson, U.-L. Pen, A. Farchi, H.-R. Yu, and J. Harnois-Déraps. Precision reconstruction of the cold dark matter-neutrino relative velocity from N -body simulations. *Physical Review D*, 92(2):023502, July 2015.

[86] T. Ishiyama. Hierarchical Formation of Dark Matter Halos and the Free Streaming Scale. *The Astrophysical Journal*, 788:27, June 2014.

[87] R. Jimenez, C. Pena-Garay, and L. Verde. Neutrino footprint in Large Scale Structure. *ArXiv e-prints*, February 2016.

[88] Y. P. Jing. The density profile of equilibrium and nonequilibrium dark matter halos. *The Astrophysical Journal*, 535(1):30, 2000.

[89] M. Joyce, B. Marcos, and F. Sylos Labini. Energy ejection in the collapse of a cold spherical self-gravitating cloud. *Monthly Notices of the Royal Astronomical Society*, 397:775–792, August 2009.

[90] F. Kahlhoefer. Review of LHC dark matter searches. *International Journal of Modern Physics A*, 32:1730006, May 2017.

[91] M. Kamionkowski and S. M. Koushiappas. Galactic substructure and direct detection of dark matter. *Physical Review D*, 77(10):103509, May 2008.

[92] M. Kamionkowski, S. M. Koushiappas, and M. Kuhlen. Galactic substructure and dark-matter annihilation in the Milky Way halo. *Physical Review D*, 81(4):043532, February 2010.

[93] L. J. King and J. M. G. Mead. The mass-concentration relationship of virialized haloes and its impact on cosmological observables. *Monthly Notices of the Royal Astronomical Society*, 416:2539–2549, October 2011.

[94] A. Klypin, G. Yepes, S. Gottlöber, F. Prada, and S. Heß. MultiDark simulations: the story of dark matter halo concentrations and density profiles. *Monthly Notices of the Royal Astronomical Society*, 457:4340–4359, April 2016.

[95] A. A. Klypin, S. Trujillo-Gomez, and J. Primack. Dark Matter Halos in the Standard Cosmological Model: Results from the Bolshoi Simulation. *The Astrophysical Journal*, 740:102, October 2011.

[96] M. Kuhlen, J. Diemand, and P. Madau. The Dark Matter Annihilation Signal from Galactic Substructure: Predictions for GLAST. *The Astrophysical Journal*, 686:262–278, October 2008.

[97] C. Lacey and S. Cole. Merger rates in hierarchical models of galaxy formation. *Monthly Notices of the Royal Astronomical Society*, 262:627–649, June 1993.

[98] M. Lang, K. Holley-Bockelmann, and M. Sinha. Voronoi Tessellation and Non-parametric Halo Concentration. *The Astrophysical Journal*, 811:152, October 2015.

[99] G. Lavaux, N. Afshordi, and M. J. Hudson. First measurement of the bulk flow of nearby galaxies using the cosmic microwave background. *Monthly Notices of the Royal Astronomical Society*, 430:1617–1635, April 2013.

[100] G. Lemson and G. Kauffmann. Environmental influences on dark matter haloes and consequences for the galaxies within them. *Monthly Notices of the Royal Astronomical Society*, 302:111–117, January 1999.

[101] J. Lesgourgues and S. Pastor. Massive neutrinos and cosmology. *Physics Report*, 429:307–379, July 2006.

[102] J. Lesgourgues and S. Pastor. Neutrino mass from Cosmology. *ArXiv e-prints*, December 2012.

[103] M. Levi, C. Bebek, T. Beers, R. Blum, R. Cahn, D. Eisenstein, B. Flaugher, K. Honscheid, R. Kron, O. Lahav, P. McDonald, N. Roe, D. Schlegel, and representing the DESI collaboration. The DESI Experiment, a whitepaper for Snowmass 2013. *ArXiv e-prints*, August 2013.

[104] A. Lewis, A. Challinor, and A. Lasenby. Efficient Computation of Cosmic Microwave Background Anisotropies in Closed Friedmann-Robertson-Walker Models. *The Astrophysical Journal*, 538:473–476, August 2000.

[105] M. LoVerde. Neutrino mass without cosmic variance. *Physical Review D*, 93(10):103526, May 2016.

[106] A. D. Ludlow, J. F. Navarro, R. E. Angulo, M. Boylan-Kolchin, V. Springel, C. Frenk, and S. D. M. White. The mass-concentration-redshift relation of cold dark matter haloes. *Monthly Notices of the Royal Astronomical Society*, 441:378–388, June 2014.

[107] A. D. Ludlow, J. F. Navarro, M. Boylan-Kolchin, P. E. Bett, R. E. Angulo, M. Li, S. D. M. White, C. Frenk, and V. Springel. The mass profile and accretion history of cold dark matter haloes. *Monthly Notices of the Royal Astronomical Society*, 432:1103–1113, June 2013.

[108] A. D. Ludlow, J. F. Navarro, M. Li, R. E. Angulo, M. Boylan-Kolchin, and P. E. Bett. The dynamical state and mass-concentration relation of galaxy clusters. *Monthly Notices of the Royal Astronomical Society*, 427:1322–1328, December 2012.

[109] A. V. Macciò, A. A. Dutton, and F. C. van den Bosch. Concentration, spin and shape of dark matter haloes as a function of the cosmological model: WMAP1,

WMAP3 and WMAP5 results. *Monthly Notices of the Royal Astronomical Society*, 391:1940–1954, December 2008.

[110] A. V. Macciò, A. A. Dutton, F. C. van den Bosch, B. Moore, D. Potter, and J. Stadel. Concentration, spin and shape of dark matter haloes: scatter and the dependence on mass and environment. *Monthly Notices of the Royal Astronomical Society*, 378:55–71, June 2007.

[111] K. J. Mack. Known unknowns of dark matter annihilation over cosmic time. *Monthly Notices of the Royal Astronomical Society*, 439:2728–2735, April 2014.

[112] R. Mainini and A. Romano. Constraining the mass-concentration relation through weak lensing peak function. *JCAP*, 8:063, August 2014.

[113] M. Maltoni, T. Schwetz, M. A. Tórtola, and J. W. Valle. Status of three-neutrino oscillations after the SNO-salt data. *Physical Review D*, 68(11):113010, December 2003.

[114] G. A. Mamon, J. Chevalier, A. J. Romanowsky, and R. Wojtak. Dark matter inner slope and concentration in galaxies: from the Fornax dwarf to M87. In M. Cappellari and S. Courteau, editors, *Galaxy Masses as Constraints of Formation Models*, volume 311 of *IAU Symposium*, pages 16–19, April 2015.

[115] Y.-Y. Mao, M. Williamson, and R. H. Wechsler. The Dependence of Subhalo Abundance on Halo Concentration. *The Astrophysical Journal*, 810:21, September 2015.

[116] T. Marrodán Undagoitia and L. Rauch. Dark matter direct-detection experiments. *Journal of Physics G Nuclear Physics*, 43(1):013001, January 2016.

[117] B. Mathiesen, A. E. Evrard, and J. J. Mohr. The Effects of Clumping and Substructure on Intracluster Medium Mass Measurements. *The Astrophysical Journal Letters*, 520:L21–L24, July 1999.

[118] P. McDonald. Gravitational redshift and other redshift-space distortions of the imaginary part of the power spectrum. *JCAP*, 11:026, November 2009.

[119] S. S. McGaugh, M. K. Barker, and W. J. G. de Blok. A Limit on the Cosmological Mass Density and Power Spectrum from the Rotation Curves of Low Surface Brightness Galaxies. *The Astrophysical Journal*, 584:566–576, February 2003.

[120] D. Merritt, J. F. Navarro, A. Ludlow, and A. Jenkins. A Universal Density Profile for Dark and Luminous Matter? *The Astrophysical Journal Letters*, 624:L85–L88, May 2005.

[121] Á. Moliné, M. A. Sánchez-Conde, S. Palomares-Ruiz, and F. Prada. Characterization of subhalo structural properties and implications for dark matter annihilation signals. *Monthly Notices of the Royal Astronomical Society*, 466:4974–4990, April 2017.

[122] B. Moore, S. Ghigna, F. Governato, G. Lake, T. Quinn, J. Stadel, and P. Tozzi. Dark Matter Substructure within Galactic Halos. *The Astrophysical Journal Letters*, 524:L19–L22, October 1999.

[123] J. C. Muñoz-Cuartas, A. V. Macciò, S. Gottlöber, and A. A. Dutton. The redshift evolution of Λ cold dark matter halo parameters: concentration, spin and shape. *Monthly Notices of the Royal Astronomical Society*, 411:584–594, February 2011.

[124] J. F. Navarro, C. S. Frenk, and S. D. M. White. The Structure of Cold Dark Matter Halos. *The Astrophysical Journal*, 462:563, May 1996.

[125] J. F. Navarro, C. S. Frenk, and S. D. M. White. A Universal Density Profile from Hierarchical Clustering. *The Astrophysical Journal*, 490:493–508, December 1997.

[126] J. F. Navarro, E. Hayashi, C. Power, A. R. Jenkins, C. S. Frenk, S. D. M. White, V. Springel, J. Stadel, and T. R. Quinn. The inner structure of ΛCDM haloes - III. Universality and asymptotic slopes. *Monthly Notices of the Royal Astronomical Society*, 349:1039–1051, April 2004.

[127] A. F. Neto, L. Gao, P. Bett, S. Cole, J. F. Navarro, C. S. Frenk, S. D. M. White, V. Springel, and A. Jenkins. The statistics of Λ CDM halo concentrations. *Monthly Notices of the Royal Astronomical Society*, 381:1450–1462, November 2007.

[128] K. C. Y. Ng, R. Laha, S. Campbell, S. Horiuchi, B. Dasgupta, K. Murase, and J. F. Beacom. Resolving small-scale dark matter structures using multisource indirect detection. *Physical Review D*, 89(8):083001, April 2014.

[129] C. Okoli and N. Afshordi. Concentration, ellipsoidal collapse, and the densest dark matter haloes. *Monthly Notices of the Royal Astronomical Society*, 456:3068–3078, March 2016.

[130] C. Okoli, J. E. Taylor, and N. Afshordi. Searching for dark matter annihilation from individual halos: uncertainties, scatter and signal-to-noise ratios. *JCAP*, 8:019, August 2018.

[131] T. Padmanabhan. *Structure Formation in the Universe*. Cambridge University Press, May 1993.

[132] T. Padmanabhan. *Theoretical Astrophysics - Volume 1, Astrophysical Processes*. Cambridge University Press, December 2000.

[133] C. Pfrommer, R. Pakmor, C. M. Simpson, and V. Springel. Simulating Gamma-Ray Emission in Star-forming Galaxies. *The Astrophysical Journal Letters*, 847:L13, October 2017.

[134] L. Pieri, G. Bertone, and E. Branchini. Dark matter annihilation in substructures revised. *Monthly Notices of the Royal Astronomical Society*, 384:1627–1637, March 2008.

[135] Planck Collaboration, P. A. R. Ade, N. Aghanim, C. Armitage-Caplan, M. Arnaud, M. Ashdown, F. Atrio-Barandela, J. Aumont, C. Baccigalupi, A. J. Banday, and et al. Planck 2013 results. XVI. Cosmological parameters. *Astronomy and Astrophysics*, 571:A16, November 2014.

[136] Planck Collaboration, P. A. R. Ade, N. Aghanim, M. Arnaud, M. Ashdown, J. Aumont, C. Baccigalupi, A. J. Banday, R. B. Barreiro, J. G. Bartlett, and et al. Planck 2015 results. XIII. Cosmological parameters. *Astronomy and Astrophysics*, 594:A13, September 2016.

[137] G. B. Poole, C. Blake, F. A. Marín, C. Power, S. J. Mutch, D. J. Croton, M. Colless, W. Couch, M. J. Drinkwater, and K. Glazebrook. The Gigaparsec WiggleZ simulations: characterizing scale-dependant bias and associated systematics in growth of structure measurements. *Monthly Notices of the Royal Astronomical Society*, 449:1454–1469, May 2015.

[138] F. Prada, A. A. Klypin, A. J. Cuesta, J. E. Betancort-Rijo, and J. Primack. Halo concentrations in the standard Λ cold dark matter cosmology. *Monthly Notices of the Royal Astronomical Society*, 423:3018–3030, July 2012.

[139] W. H. Press and P. Schechter. Formation of Galaxies and Clusters of Galaxies by Self-Similar Gravitational Condensation. *The Astrophysical Journal*, 187:425–438, February 1974.

[140] D. S. Reed, R. Bower, C. S. Frenk, A. Jenkins, and T. Theuns. The halo mass function from the dark ages through the present day. *Monthly Notices of the Royal Astronomical Society*, 374:2–15, January 2007.

[141] M. Ricotti, A. Pontzen, and M. Viel. Is the Concentration of Dark Matter Halos at Virialization Universal? *The Astrophysical Journal Letters*, 663:L53–L56, July 2007.

[142] S. RiemerSørensen, C. Blake, D. Parkinson, T. M. Davis, S. Brough, M. Colless, C. Contreras, W. Couch, S. Croom, D. Croton, M. J. Drinkwater, K. Forster, D. Gilbank, M. Gladders, K. Glazebrook, B. Jelliffe, R. J. Jurek, I.-h. Li, B. Madore, D. C. Martin, K. Pimbblet, G. B. Poole, M. Pracy, R. Sharp, E. Wisnioski, D. Woods, T. K. Wyder, and H. K. C. Yee. WiggleZ Dark Energy Survey: Cosmological neutrino mass constraint from blue high-redshift galaxies. *Physical Review D*, 85(8):081101, April 2012.

[143] V. C. Rubin and W. K. Ford, Jr. Rotation of the Andromeda Nebula from a Spectroscopic Survey of Emission Regions. *The Astrophysical Journal*, 159:379, February 1970.

[144] E. Salvador-Solé, A. Manrique, G. González-Casado, and S. H. Hansen. The Nature of Dark Matter and the Density Profile and Central Behavior of Relaxed Halos. *The Astrophysical Journal*, 666:181–188, September 2007.

[145] E. Salvador-Solé, J. Viñas, A. Manrique, and S. Serra. Theoretical dark matter halo density profile. *Monthly Notices of the Royal Astronomical Society*, 423:2190–2202, July 2012.

[146] M. A. Sánchez-Conde and F. Prada. The flattening of the concentration-mass relation towards low halo masses and its implications for the annihilation signal boost. *Monthly Notices of the Royal Astronomical Society*, 442:2271–2277, August 2014.

[147] P. Santini, et al. The Main Sequence relation in the HST Frontier Fields. *ArXiv e-prints*, June 2017.

[148] E. Schaan, S. Ferraro, M. Vargas-Magaña, K. M. Smith, S. Ho, S. Aiola, N. Battaglia, J. R. Bond, F. De Bernardis, E. Calabrese, H.-M. Cho, M. J. Devlin, J. Dunkley, P. A. Gallardo, M. Hasselfield, S. Henderson, J. C. Hill, A. D. Hincks, R. Hlozek, J. Hubmayr, J. P. Hughes, K. D. Irwin, B. Koopman, A. Kosowsky, D. Li, T. Louis, M. Lungu, M. Madhavacheril, L. Maurin, J. J. McMahon, K. Moodley, S. Naess, F. Nati, L. Newburgh, M. D. Niemack, L. A. Page, C. G. Pappas, B. Partridge, B. L. Schmitt, N. Sehgal, B. D. Sherwin, J. L. Sievers, D. N. Spergel, S. T. Staggs, A. van Engelen, E. J. Wollack, and ACTPol Collaboration. Evidence for the kinematic Sunyaev-Zel'dovich effect with the Atacama Cosmology Telescope and velocity

reconstruction from the Baryon Oscillation Spectroscopic Survey. *Physical Review D*, 93(8):082002, April 2016.

[149] M. Selig, V. Vacca, N. Oppermann, and T. A. Enßlin. The denoised, deconvolved, and decomposed Fermi γ-ray sky. An application of the D^{3}PO algorithm. *Astronomy and Astrophysics*, 581:A126, September 2015.

[150] R. K. Sheth, H. J. Mo, and G. Tormen. Ellipsoidal collapse and an improved model for the number and spatial distribution of dark matter haloes. *Monthly Notices of the Royal Astronomical Society*, 323:1–12, May 2001.

[151] J. Silk et al. *Particle Dark Matter: Observations, Models and Searches*. Cambridge Univ. Press, Cambridge, 2010.

[152] R. A. Skibba, M. S. M. Smith, A. L. Coil, J. Moustakas, J. Aird, M. R. Blanton, A. D. Bray, R. J. Cool, D. J. Eisenstein, A. J. Mendez, K. C. Wong, and G. Zhu. PRIMUS: Galaxy Clustering as a Function of Luminosity and Color at 0.2 z 1. *The Astrophysical Journal*, 784:128, April 2014.

[153] T. R. Slatyer, N. Padmanabhan, and D. P. Finkbeiner. CMB constraints on WIMP annihilation: Energy absorption during the recombination epoch. *Physical Review D*, 80(4):043526, August 2009.

[154] M. Sparre and S. H. Hansen. The behaviour of shape and velocity anisotropy in dark matter haloes. *JCAP*, 10:049, October 2012.

[155] V. Springel, N. Yoshida, and S. D. M. White. GADGET: a code for collisionless and gasdynamical cosmological simulations. *New Astronomy*, 6:79–117, April 2001.

[156] N. S. Sugiyama, T. Okumura, and D. N. Spergel. Will kinematic Sunyaev-Zel'dovich measurements enhance the science return from galaxy redshift surveys? *JCAP*, 1:057, January 2017.

[157] I. Tamborra, S. Ando, and K. Murase. Star-forming galaxies as the origin of diffuse high-energy backgrounds: gamma-ray and neutrino connections, and implications for starburst history. *JCAP*, 9:043, September 2014.

[158] J. E. Taylor and A. Babul. The evolution of substructure in galaxy, group and cluster haloes - II. Global properties. *Monthly Notices of the Royal Astronomical Society*, 364:515–534, December 2005.

[159] J. E. Taylor and J. Silk. The clumpiness of cold dark matter: implications for the annihilation signal. *Monthly Notices of the Royal Astronomical Society*, 339:505–514, February 2003.

[160] The Fermi LAT collaboration. Limits on dark matter annihilation signals from the Fermi LAT 4-year measurement of the isotropic gamma-ray background. *JCAP*, 9:8, September 2015.

[161] J. Tinker, A. V. Kravtsov, A. Klypin, K. Abazajian, M. Warren, G. Yepes, S. Gottlöber, and D. E. Holz. Toward a Halo Mass Function for Precision Cosmology: The Limits of Universality. *The Astrophysical Journal*, 688:709–728, December 2008.

[162] J. L. Tinker, B. E. Robertson, A. V. Kravtsov, A. Klypin, M. S. Warren, G. Yepes, and S. Gottlöber. The Large-scale Bias of Dark Matter Halos: Numerical Calibration and Model Tests. *The Astrophysical Journal*, 724:878–886, December 2010.

[163] D. Tseliakhovich and C. Hirata. Relative velocity of dark matter and baryonic fluids and the formation of the first structures. *Physical Review D*, 82(8):083520, October 2010.

[164] P. Ullio, L. Bergström, J. Edsjö, and C. Lacey. Cosmological dark matter annihilations into γ rays: A closer look. *Physical Review D*, 66(12):123502, December 2002.

[165] E. van Uitert, M. Cacciato, H. Hoekstra, M. Brouwer, C. Sifón, M. Viola, I. Baldry, J. Bland-Hawthorn, S. Brough, M. J. I. Brown, A. Choi, S. P. Driver, T. Erben, C. Heymans, H. Hildebrandt, B. Joachimi, K. Kuijken, J. Liske, J. Loveday, J. McFarland, L. Miller, R. Nakajima, J. Peacock, M. Radovich, A. S. G. Robotham, P. Schneider, G. Sikkema, E. N. Taylor, and G. Verdoes Kleijn. The stellar-to-halo mass relation of GAMA galaxies from 100 square degrees of KiDS weak lensing data. *ArXiv e-prints*, January 2016.

[166] G. M. Voit. Tracing cosmic evolution with clusters of galaxies. *Reviews of Modern Physics*, 77:207–258, April 2005.

[167] D. Walsh, R. F. Carswell, and R. J. Weymann. 0957 + 561 A, B - Twin quasistellar objects or gravitational lens. *Nature*, 279:381–384, May 1979.

[168] M. S. Warren, K. Abazajian, D. E. Holz, and L. Teodoro. Precision Determination of the Mass Function of Dark Matter Halos. *The Astrophysical Journal*, 646:881–885, August 2006.

[169] M. S. Warren, P. J. Quinn, J. K. Salmon, and W. H. Zurek. Dark halos formed via dissipationless collapse. I - Shapes and alignment of angular momentum. *The Astrophysical Journal*, 399:405–425, November 1992.

[170] Risa H. Wechsler, James S. Bullock, Joel R. Primack, Andrey V. Kravtsov, and Avishai Dekel. Concentrations of dark halos from their assembly histories. *The Astrophysical Journal*, 568(1):52, 2002.

[171] A. R. Wetzel, J. D. Cohn, M. White, D. E. Holz, and M. S. Warren. The Clustering of Massive Halos. *The Astrophysical Journal*, 656:139–147, February 2007.

[172] R. Wojtak and E. L. Łokas. Mass profiles and galaxy orbits in nearby galaxy clusters from the analysis of the projected phase space. *Monthly Notices of the Royal Astronomical Society*, 408:2442–2456, November 2010.

[173] J. Wolf and J. S. Bullock. Dark matter concentrations and a search for cores in Milky Way dwarf satellites. *ArXiv e-prints*, March 2012.

[174] X.-P. Wu and Y.-J. Xue. Correlation between the Halo Concentration C and the Virial Mass M_{VIR} Determined from X-Ray Clusters. *The Astrophysical Journal Letters*, 529:L5–L7, January 2000.

[175] M. Wyman, D. H. Rudd, R. A. Vanderveld, and W. Hu. Neutrinos Help Reconcile Planck Measurements with the Local Universe. *Physical Review Letters*, 112(5):051302, February 2014.

[176] J. Yoo and U. Seljak. Signatures of first stars in galaxy surveys: Multitracer analysis of the supersonic relative velocity effect and the constraints from the BOSS power spectrum measurements. *Physical Review D*, 88(10):103520, November 2013.

[177] A. Zait, Y. Hoffman, and I. Shlosman. Dark Matter Halos: Velocity Anisotropy-Density Slope Relation. *The Astrophysical Journal*, 682:835–840, August 2008.

[178] J. Zavala and N. Afshordi. Clustering in the phase space of dark matter haloes - II. Stable clustering and dark matter annihilation. *Monthly Notices of the Royal Astronomical Society*, 441:1329–1339, June 2014.

[179] Y. B. Zel'dovich. Gravitational instability: An approximate theory for large density perturbations. *Astronomy and Astrophysics*, 5:84–89, March 1970.

[180] D. H. Zhao, Y. P. Jing, H. J. Mo, and G.. Börner. Mass and Redshift Dependence of Dark Halo Structure. *The Astrophysical Journal Letters*, 597:L9–L12, November 2003.

[181] D. H. Zhao, Y. P. Jing, H. J. Mo, and G. Börner. Accurate universal models for the mass accretion histories and concentrations of dark matter halos. *The Astrophysical Journal*, 707(1):354, 2009.

[182] D. H. Zhao, H. J. Mo, Y. P. Jing, and G. Börner. The growth and structure of dark matter haloes. *Monthly Notices of the Royal Astronomical Society*, 339:12–24, February 2003.

[183] H.-M. Zhu, U.-L. Pen, X. Chen, D. Inman, and Y. Yu. Measurement of Neutrino Masses from Relative Velocities. *Physical Review Letters*, 113(13):131301, September 2014.

[184] F. Zwicky. Die Rotverschiebung von extragalaktischen Nebeln. *Helvetica Physica Acta*, 6:110–127, 1933.

Appendix A

APPENDIX for Chapter Four

A.1 SNR from the gravitational field due to dynamical friction

Following the correction to the gravitational field due the dynamical friction effect from neutrinos, $\mathbf{g_k} \rightarrow \mathbf{g_k} + \mathbf{g}_{\nu,\mathbf{k}}$, we can express this as a measurable effect to the power spectrum of galaxies in a redshift survey. Using divergence form of Gauss's equation for gravity, $\nabla \cdot \mathbf{g} = -4\pi a G\rho$, the Fourier space version is given as

$$\mathbf{g_k} = \frac{4\pi i a G\rho_k \mathbf{k}}{|\mathbf{k}|^{\mathbf{2}}}, \tag{A.1}$$

while that of the Poisson equation is

$$\Phi_k = -\frac{4\pi a^2 G\rho_k}{|\mathbf{k}|^{\mathbf{2}}}. \tag{A.2}$$

Thus,

$$\begin{aligned} \mathbf{g_k} &\rightarrow \mathbf{g_k} + \mathbf{g}_{\nu,\mathbf{k}} \\ &= \frac{4\pi i a G\rho_k \mathbf{k}}{|\mathbf{k}|^{\mathbf{2}}} \left(1 + i\frac{2a^2 G\sum_{i=1}^{3} m_i^4 \mu \mathbf{v}_{ic}(z)\cdot\mathbf{k}}{\hbar^3 |\mathbf{k}|^{\mathbf{3}}}\right), \\ &= \frac{4\pi i a G\rho_m \delta_k \mathbf{k}}{|\mathbf{k}|^{\mathbf{2}}} \left(1 + i\frac{2a^2 G\sum_{i=1}^{3} m_i^4 \mu \mathbf{v}_{ic}(z)\cdot\mathbf{k}}{\hbar^3 |\mathbf{k}|^{\mathbf{3}}}\right), \end{aligned} \tag{A.3}$$

where we have used Eq. (4.20) in comoving coordinates to substitute for $\mathbf{g}_{\nu,\mathbf{k}}$.

We shall see that this signal can be extracted by looking at the redshift space distortion of galaxy surveys. Recall that the redshift-space distance r^s is related to the real-space distance r^d through

$$r^s = r^d + \frac{v_x}{aH}, \tag{A.4}$$

where v_x is the velocity along the line of sight and H is the Hubble constant. Using continuity equation for matter, we can find the redshift space overdensity for galaxies δ_g^s in terms of its real space overdensity δ_g^d and matter overdensity δ_m:

$$\delta^s_{g,k} = \delta^d_{g,k} - \nabla \cdot \left(\frac{v_x \hat{\mathbf{x}}}{aH}\right) \Rightarrow \delta^s_{g,k} = \delta^d_{g,k} - \frac{k_x^2 \dot{\delta}_{m,k}}{H|\mathbf{k}|^2}. \tag{A.5}$$

Due to the dynamical friction of the neutrinos (assuming a uniform $\mathbf{v}_{\nu c}$) the matter overdensity has a redshift-dependent phase (A.3):

$$\begin{aligned} \delta_{m,k}(z) &\simeq D_L(k,z) e^{i\phi_{\mathbf{k}}(z)} \delta_{m0,k}, \\ \phi_{\mathbf{k}}(z) &= \frac{2a^2 G \sum_{i=1}^3 m_i^4 \mu \mathbf{v}_{ic}(z) \cdot \mathbf{k}}{\hbar^3 |\mathbf{k}|^{\mathbf{3}}}, \end{aligned} \tag{A.6}$$

where $D_L(k,z)$ is the (scale-dependent) linear growth factor for $\nu\Lambda$CDM cosmology. For a single tracer in redshift-space, the density perturbation is given as

$$\begin{aligned} \delta^s_{g,k} &= \delta^d_{g,k} - \frac{k_x^2 \dot{\delta}_{m,k}}{H|\mathbf{k}|^2} \\ &= \delta^d_{g,k} \left(1 - \frac{k_x^2}{b_g H |\mathbf{k}|^2} \frac{\dot{D}_L}{D_L} - i \frac{\dot{\phi} k_x^2}{H b_g |\mathbf{k}|^2}\right) \\ &= \delta_{m,k} \left(b_g - \frac{k_x^2}{H|\mathbf{k}|^2} \frac{\dot{D}_L}{D_L} - i \frac{\dot{\phi} k_x^2}{H|\mathbf{k}|^2}\right). \end{aligned} \tag{A.7}$$

The first two terms in the above equation are the standard RSD terms while the last term is new, as a result of the effect of dynamical friction due to neutrinos. Measuring this signal from a single tracer requires a very good knowledge of the linear bias term and is also susceptible to sample variance. One may eliminate the sample variance limitation by considering multiple tracers, as first suggested in [118]. This is because, in the absence of shot noise, the ratio of Fourier amplitudes for two tracers can be measured perfectly, even for a single mode. While this ratio is real in standard multi-tracer RSD [118], it finds an imaginary part (leading to a dipole) in the presence of a neutrino wind. There could also be a comparable imaginary term for different tracer biases, b_f and b_l, which we shall ignore for our simple S/N estimate here.

We will consider cross-correlating two distinct populations of galaxies with similar comoving densities n_l and n_f, and biases b_l and b_f. This is given as

$$\begin{aligned} C_{fl} &\equiv \langle \delta^s_{l,k}\delta^{*s}_{f,k}\rangle = \left\langle \left(\delta^d_{l,k} - \frac{k_x^2\dot{\delta}_{m,k}}{H|\mathbf{k}|^2}\right)\left(\delta^{d*}_{f,k} - \frac{ak_x^2\dot{\delta}^*_{m,k}}{H|\mathbf{k}|^2}\right)\right\rangle, \\ &= b_l b_f P_k \Bigg[1 - \frac{\dot{D}_L k_x^2}{HD_L|\mathbf{k}|^2}\left(\frac{1}{b_l}+\frac{1}{b_f}\right) + \\ &\qquad \frac{k_x^4}{b_l b_f H|\mathbf{k}|^4}\left(\frac{\dot{D}_L^2}{D_L^2}+\dot{\phi}_{\mathbf{k}}^2\right)\Bigg] - \frac{ib_l b_f P_k\dot{\phi}_{\mathbf{k}}k_x^2}{H|\mathbf{k}|^2}\left(\frac{1}{b_l}-\frac{1}{b_f}\right). \end{aligned} \tag{A.8}$$

As can be seen from the last equation, the dynamical friction due to neutrinos has introduced an imaginary term to the redshift- space cross-power spectrum. This imaginary term is the signal per mode we hope to capture. Recall that

$$\dot{\phi}_{\mathbf{k}} = \sum_{i=1}^{3}\left(\frac{2Gm_i^4\mu H}{\hbar^3|\mathbf{k}|^{\mathbf{3}}}\right)\mathbf{k}\cdot\left[2a^2\mathbf{v}_{ic}(z) - a\frac{\partial\mathbf{v}_{ic}(z)}{\partial z}\right]. \tag{A.9}$$

Ignoring the effect of neutrinos, the noise variance for every mode is given by, e.g, [118]:

$$\begin{aligned} (\Delta\ \mathrm{Im}\ C_{fl})^2 &= \langle|\ \mathrm{Im}\ C_{fl}|^2\rangle = \frac{1}{2}(C_{ff}C_{ll} - C_{fl}C_{fl}) \\ C_{ll} &= \left(b_l - \frac{k_x^2\dot{D}_L}{|\mathbf{k}|^2HD_L}\right)^2 P_k + n_l^{-1} \\ C_{ff} &= \left(b_f - \frac{k_x^2\dot{D}_L}{|\mathbf{k}|^2HD_L}\right)^2 P_k + n_f^{-1} \\ C_{fl} &= \left(b_l - \frac{k_x^2\dot{D}_L}{|\mathbf{k}|^2HD_L}\right)\left(b_f - \frac{k_x^2\dot{D}_L}{|\mathbf{k}|^2HD_L}\right)P_k \end{aligned} \tag{A.10}$$

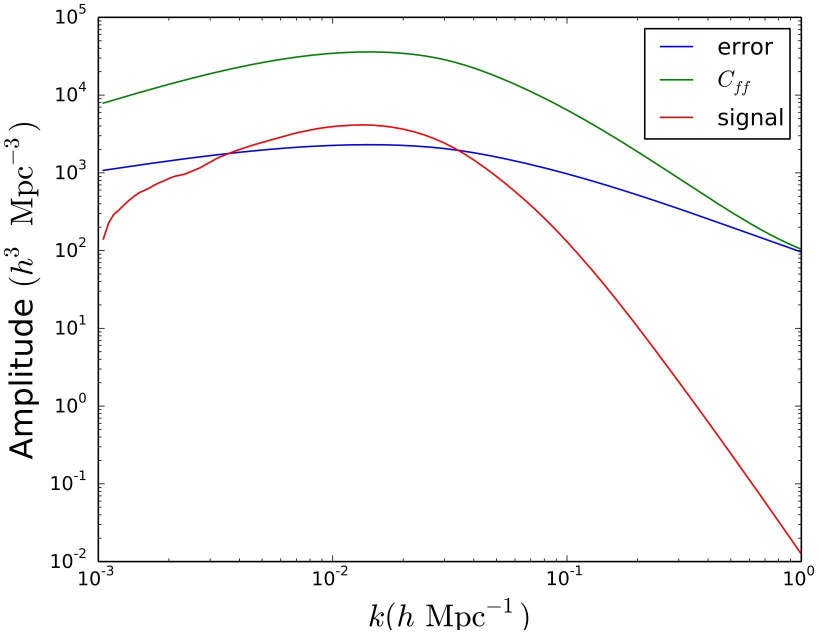

Figure A.1: The amplitude of the signal from the imaginary part of the cross-power spectrum, the error on the signal, and the auto-power spectrum of faint galaxies, C_{ff}, are shown for a 0.1 eV neutrino, $n_f = n_l = 0.02\ h^3\mathrm{Mpc}^{-3}$, and $b_l = 2b_f = 2$.

Consider these as the elements of a matrix C given by

$$\begin{bmatrix} C_{ll} & C_{fl} \\ C_{fl} & C_{ff} \end{bmatrix}$$

the noise variance is thus one half of the determinant of C, $\det C$.

The amplitude of our signal, $\mathrm{Im}\ C_{fl}$, its error $\Delta\ \mathrm{Im}\ C_{fl}$, and the auto-power spectrum of faint galaxies is shown in Figure A.1. This figure shows that the signal is dominated by large scale modes. The decline of the signal at small scales suggests that the measurement isn't improved by summing lots of modes. It is therefore not sample variance limited.

A.2 Testing nonlinear effects using N-body simulations

We shall next examine to what extent the nonlinear structure formation in standard ΛCDM model could mimic the effects of neutrino dynamical friction on cosmological haloes. We therefore use an N-body simulation without neutrinos in order to systematically account for the nonlinear effects.

The signal we study is the difference in relative displacement due to neutrinos, Δx, for two different tracers, given by $(\Delta x_1 - \Delta x_2) = \frac{1}{2}(\Delta v_{\nu c,1} - \Delta v_{\nu c,2})t = \frac{1}{2}v_{\rm rel}t$, where we denote the relative velocity between tracers 1 and 2 by $v_{\rm rel}$. We want to know whether nonlinear velocities due to growth of structure on small scales could produce a signal that could interfere with the signal from massive neutrinos.

To this end, we use an N-body simulation without massive neutrinos to investigate the possibility of any existing contaminating signal from nonlinear effects. Assuming the neutrino streaming direction in any given volume is the same direction as the CDM bulk flow $\boldsymbol{v}_c$ (which it should be to first order), then we would expect the relative velocity $\boldsymbol{v}_{\rm rel}$ between halo populations 1 and 2 to be in that direction also. So we want to know whether there is any nonzero correlation between the direction of $\boldsymbol{v}_{\rm rel}$ and $\boldsymbol{v}_c$ in the absence of massive neutrinos. That is, we want

$$\langle \hat{\boldsymbol{v}}_{\rm rel} \cdot \hat{\boldsymbol{v}}_c \rangle = 0, \tag{A.11}$$

where the averaging is over independent volumes, which we take to be spheres of radius R, and the hat denotes the unit vector.

This effect is tested using the Gigaparsec WiggleZ (GiggleZ) N-body simulation [137]. The GiggleZ main simulation contains 2160^3 dark matter particles in a periodic box of side $1h^{-1}$ Gpc. The particle mass is $7.5 \times 10^9 h^{-1} M_\odot$, which allows bound systems with masses $\gtrsim 1.5 \times 10^{11} h^{-1} M_\odot$ to be resolved. The clustering bias b of the haloes range from ~ 1 to greater than 2. Halo finding for GiggleZ was performed using SUBFIND [155], which utilizes a friends-of-friends (FoF) algorithm to identify coherent overdensities of particles and a substructure analysis to determine bound overdensities within each FoF halo. The resulting SUBFIND substructure catalogues are rank-ordered by their maximum circular velocity ($V_{\rm max,sub}$) as a proxy for halo size.

$$\begin{aligned} \boldsymbol{v}_1 &= \alpha_1 \boldsymbol{v}_c + \boldsymbol{n}_1 \\ \boldsymbol{v}_2 &= \alpha_2 \boldsymbol{v}_c + \boldsymbol{n}_2. \end{aligned} \tag{A.12}$$

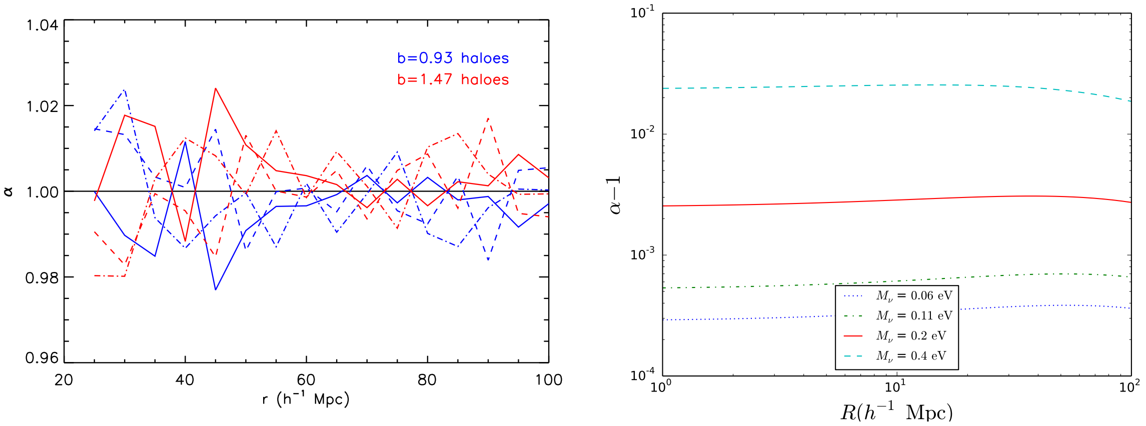

Figure A.2: (a)(Left) Fitted value of α over 100 spheres of radius r, for the (x, y, z) components (solid, dashed and dot-dashed lines) of the bulk flow of our two halo samples. (b)(Right) ΛCDM prediction for α from Eq. (A.13) [for a $10^{15}(h^{-1}M_\odot$ halo)] as a function of top hat window function radius R and different sum of neutrino mass.

In the absence of neutrinos, the equivalence principle implies that $\alpha \equiv 1$, so we expect $\langle \boldsymbol{v}_{\rm rel} \rangle = 0$, i.e. $\alpha_1 = \alpha_2 = 1$, and $\langle \boldsymbol{v}_{\rm rel} \cdot \boldsymbol{v}_c \rangle = 0$.

In the presence of massive neutrinos, we expect that for haloes of mass M within a volume of radius R [13],

$$\alpha(R) = 1 + \frac{\langle \boldsymbol{v}_c(R) \cdot \Delta \boldsymbol{v}_{\nu c}(M, R) \rangle}{\langle \boldsymbol{v}_c(R) \cdot \boldsymbol{v}_c(R) \rangle}. \tag{A.13}$$

Figure (A.2a) shows the measured value of α from the relative velocity of our halo samples, which is consistent with zero at $<$ % level, with no evident systematic bias. A larger sample and/or simulation box will lead to lower stochastic noise in α, and can potentially reveal a systematic bias, albeit at a lower level.

The expected value of α can be calculated from our equation for $\Delta v_{\nu c}$ and the ΛCDM prediction for $\boldsymbol{v}_c$. The 1D rms velocity dispersion of CDM is

$$\begin{aligned} \langle v_c^2 \rangle &= \int \frac{d^3k}{(2\pi)^3} |v_c(k)|^2 \widetilde{W}^2(kR) \\ &= a^2 \int dk \frac{\mathcal{P}_\chi}{k^3} \left| \dot{T}_c(k) \right|^2 \widetilde{W}^2(kR). \end{aligned} \tag{A.14}$$

For the halo model estimation, $\Delta v_{\nu c}$ is given by Eq. (4.27) and thus

$$\begin{aligned}\langle \boldsymbol{v}_c(R)\cdot\Delta\boldsymbol{v}_{\nu c}(m_h,R)\rangle = &-\frac{2\mu(\boldsymbol{v}_{\nu c},\boldsymbol{k})G^2M_{\rm h}}{3\pi H\hbar^3}\sum_{i=1}^{3}m_i^4\\ &\int\frac{dk}{k}\langle\boldsymbol{v}_c\boldsymbol{v}_{ic}(<k)\rangle\left[u(k|M_{\rm h})^2+\frac{b(M_{\rm h})P_{\rm CDM}(k)u(k|M_{\rm h})}{M_{\rm h}}\right.\\ &\left.\int dM'\frac{dn}{dM'}b(M')M'u(k|M')\right] \qquad \text{(A.15)}\end{aligned}$$

and

$$\langle\boldsymbol{v}_c\cdot\boldsymbol{v}_{ic}(<k)\rangle = \int_0^k\frac{dk'}{k'}\Delta_{vc}(k',z)\Delta_{vic}(k',z)\widetilde{W}^2(k'R). \qquad \text{(A.16)}$$

The k integral is over the Fourier modes of the halo distribution while the k' integral is due to the modes from the neutrino distribution. We plot α as a function of top-hat window function radius R and different sum of neutrino mass in Figure (A.2b) for a halo of mass $M_h = 10^{15}h^{-1}M_\odot$. Clearly, the predicted value of $\alpha-1$ is quite small. For example, for $M_\nu = 0.11$ eV, the value of $\alpha-1$ is below 10^{-3} for all radii requiring 0.1 percent-level precision of the bulk flow to detect the neutrino effects.